ABSTRACT

Title of Thesis: DEVELOPMENT AND VALIDATION OF AN NPSS MODEL OF A SMALL TURBOJET ENGINE.

Stephen Michael Vannoy,
Master of Science, 2017

Thesis Directed By: Associate Professor, Christopher P. Cadou,
Department of Aerospace Engineering

Recent studies have shown that integrated gas turbine engine (GT)/solid oxide fuel cell (SOFC) systems for combined propulsion and power on aircraft offer a promising method for more efficient onboard electrical power generation. However, it appears that nobody has actually attempted to construct a hybrid GT/SOFC prototype for combined propulsion and electrical power generation. This thesis contributes to this ambition by developing an experimentally validated thermodynamic model of a small gas turbine (~230 N thrust) platform for a bench-scale GT/SOFC system. The thermodynamic model is implemented in a NASA-developed software environment called Numerical Propulsion System Simulation (NPSS). An indoor test facility was constructed to measure the engine's performance parameters: thrust, air flow rate, fuel flow rate, engine speed (RPM), and all axial stage stagnation temperatures and pressures. The NPSS model predictions are compared to the measured performance parameters for steady state engine operation.

DEVELOPMENT AND VALIDATION OF AN NPSS MODEL OF A SMALL TURBOJET ENGINE.

By

Stephen Michael Vannoy

Thesis submitted to the Faculty of the Graduate School of the
University of Maryland, College Park, in partial fulfillment
of the requirements for the degree of
Master of Science
2017

Advisory Committee:
Associate Professor Christopher P. Cadou, Chair
Associate Professor Stuart Laurence
Associate Professor Kenneth Yu

Dedication

To my family for always providing me with
unconditional love and support.

Acknowledgements

First and foremost, I would like to thank my advisor, Dr. Chris Cadou, for providing me the opportunity to work on this project and teaching me there is *always* more than one way to approach to a problem.

Thank you to the United Sates Navy and particularly the Office of Naval Research for financially supporting this project.

Thank you to Dan Waters for teaching me NPSS in the beginning and providing me assistance with the software throughout the project.

Thank you to Prof. Harald Funke at Aachen University of Applied Sciences in Aachen, Germany for providing preliminary performance data for the AMT Olympus engine prior to construction of our test facility.

I would also like to thank my labmates for creating a fun and enjoyable work environment. In particular, I would like to thank: Daanish Maqbool, Colin Adamson, Chandan Kittur, Andrew Ceruzzi, Wiam Attar, Lucas Pratt, and Branden Chiclana.

Lastly, I would like to thank the University of Maryland Police Department and College Park Fire Department for not shutting down my experiments after triggering the smoke alarms for two consecutive nights in one week during the initial testing phases.

Table of Contents

List of Tables

List of Figures

Nomenclature

Abbreviations:

AFC	alkaline fuel cell
APU	auxiliary power unit
CAD	computer-aided drawing
CEA	Chemical Equilibrium with Applications
CFD	computational fluid dynamics
CPOx	catalytic partial oxidation reactor
ECU	electronic control unit
EDT	electronic data terminal
FAR	fuel-to-air ratio
FC	fuel cell
GE	General Electric
GT	gas turbine
LFE	laminar flow element
LHC	liquid hydrocarbon
MCFC	molten carbonate fuel cell
MDF	medium-density fiberboard
NASA	National Aeronautics and Space Administration
NPSS	Numerical Propulsion System Simulation
PAFC	phosphoric acid fuel cell
PEMFC	proton exchange membrane fuel cell
RPM	rotations per minute
SLS	sea-level-static
SOFC	solid oxide fuel cell
TIT	turbine inlet temperature
UAV	unmanned air vehicle
UMD	University of Maryland
YSZ	yttria stabilized zirconia

Symbols:

A	area
b	systematic error
B	total systematic uncertainty
C_{Dmin}	drag coefficient at minimum lift
C_{Lmin}	minimum lift coefficient
C_{noz}	nozzle coefficient
C_p	specific heat capacity at constant pressure
F	force; Faraday constant; thrust
g	acceleration due to gravity; molar specific Gibbs energy
G	Gibbs free energy
h	specific enthalpy; heat transfer coefficient
H	enthalpy

k	conductivity
K	lift induced drag factor
L	length
m	mass
$\dot{m}$	mass flow rate
m_{eff}	effective fin parameter
M	Mach number
N	number/quantity; shaft speed
Nu	Nusselt number
P	pressure; perimeter
Pr	Prandtl number
q	flux
Q	heat transfer rate
Q_f	fuel heating value
R	gas constant; calculated result
$\bar{R}$	mean of a calculated result
R_t	true value of a calculated result
Re	Reynolds number
S	wing area; entropy
S_R	standard deviation of the sample for a calculated result
$S_{\bar{R}}$	standard deviation about the mean for a calculated result
S_x	standard deviation of the sample for a measurement
$S_{\bar{x}}$	standard deviation about the mean for a measurement
T	temperature; torque
$TSFC$	thrust specific fuel consumption
U	flow velocity
$U_{\bar{R}}$	total uncertainty in a calculated result
$U_{\bar{x}}$	total measurement uncertainty
v	flow or vehicle velocity; specific volume
V	voltage/electric potential
$\dot{V}$	volumetric flow rate
$\dot{W}$	work rate, power
x	length; measured quantity
$\bar{x}$	mean of a measured quantity
X_t	true measurement value
γ	ratio of specific heats
δ	pressure correction factor
Δ	change or difference in/between property values
ε	emissivity
ζ	electric power fraction
η	efficiency
θ	sensitivity coefficient; temperature correction factor
μ	viscosity
π	pressure ratio
ρ	density
σ	Stefan-Boltzmann constant

Subscripts:

0	initial value; stagnation property
air	air property
amb	ambient property
c	compressor
calc	calculated value
carnot	Carnot value
corr	corrected value
cond	conduction
conv	convection
des	design value
elec	electric, electrical
exh	exhaust property
exit	exit value
f	fuel; flow value
free	free stream property
fuel	fuel property
g	gas property
gross	gross value
in	entrance property
inlet	inlet property
input	input value
max	maximum value
out	outlet property
prop	propulsion, propulsive
ram	ram air; ram compression
s	isentropic value; static property
shaft	engine shaft
std	standard value
R	radiation; calculated result
ref	reference value
rev	reversible
t	turbine; total property; thermocouple well tip property
T	total property
w	wall property
∞	ambient/freestream property

Chapter 1: Introduction

1.1 Motivation

1.1.1 Electric Power on Aircraft

The electrical power demands on aircraft are increasing as aircraft subsystems like climate and flight controls become increasingly electric and more sensors are added to vehicle platforms. The latter is especially important in the case of unmanned air vehicles (UAVs). A survey conducted by Waters [1] compares estimates of electric power fraction (ζ) in various commercial, manned military, and unmanned aircraft (see Figure 1 [1]), where the electric power fraction is defined as the ratio of electrical power demand to total power demand:

$$\zeta = \frac{\dot{W}_{elec}}{\dot{W}_{elec} + \dot{W}_{prop}} \tag{1}$$

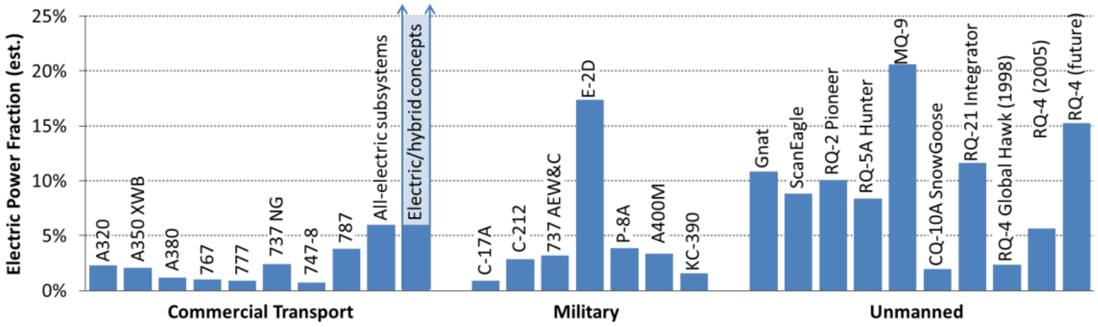

Figure 1. Electric power fractions of various commercial, military, and unmanned aircraft [1].

In Eq. (1), $\dot{W}_{elec}$ is the electric power at cruise and $\dot{W}_{prop}$ is the propulsive power at cruise. Figure 1 shows that for most modern commercial aircraft, the electric power fraction is below 4%. The two exceptions are future aircraft with entirely electric subsystems [2] which have electric power fractions of about 6%. While these are relatively low, the electric transport aircraft conceptualized by NASA [3] would have electric power fractions well in excess of 50%. Manned military aircraft exhibit similar electric power fractions to commercial aircraft. Northrop Grumman's E-2D Advanced Hawkeye is the exception with $\zeta \approx 17\%$. This large electrical power fraction is due to the Hawkeye's immense radar system. The most notable observation from Waters' survey is that electric power fractions of UAVs are significantly larger than those in commercial aircraft and most manned military aircraft. This is because UAVs require substantially larger communications and sensor payloads. As the applications of UAVs expand in both military and commercial arenas, so too will the electrical power required to operate these platforms. Consequently, the efficiency of electric power generation on these aircraft will have a progressively more important impact on fuel consumption and thus vehicle range and endurance.

Turbine-powered aircraft generally produce electrical power via mechanical generators driven by the engine's shaft or via separate auxiliary power units (APUs) [4], [5]. These processes for electrical power generation can be relatively inefficient because fuel passes through the engine's Brayton cycle to convert chemical potential energy into mechanical power before generating electrical power. Fuel cells produce electrical power more efficiently by directly converting the chemical energy stored in fuel to electrical power. For fuel cell systems without heat recovery cycles, efficiencies can reach 50-60% [6], whereas efficiencies for gas turbines (GT) are generally 20-40% [7], [8].

1.1.2 Role of Liquid Hydrocarbons

In addition to fuel cells, batteries are being considered as alternative energy sources for future hybrid/electric propulsion systems [3]. Like fuel cells, batteries offer reduced emissions, which is a significant driving factor in modern aircraft design. In Boeing's SUGAR Volt concept, batteries would power an electric motor that would be used during taxiing and takeoff to reduce fuel consumption [3]. Unfortunately, batteries have low specific energies, with the latest lithium-ion (Li-ion) batteries obtaining 0.54-0.9 MJ/kg [3]. A battery with specific energy of at least 2.7 MJ/kg would be required to power the electric assist motor in Boeing's SUGAR Volt design [3]. Newer battery technologies such as Lithium-air (or Li-air/Li-O_2) batteries have theoretical specific energy of 12.6 MJ/kg [9] compared to the theoretical specific energy of 43-48 MJ/kg for liquid hydrocarbon (LHC) aviation fuel [10].

To compare the practical specific energies of Li-air batteries and LHCs, one must consider the efficiency of their respective energy conversion systems. Assuming the efficiency of a gas turbine engine that runs on LHC fuel is 40% ([7], [8]), the practical specific energy of the fuel is 17.2-19.2 MJ/kg. Conversion efficiencies of electric motors are much higher than 40%. For example, Siemens recently developed their SP260D electric aircraft motor which has an efficiency of 95% [11]. With this efficiency, a Li-air battery powered propulsion system could potentially achieve a practical specific energy of 11.97 MJ/kg. Thus, the useful energy capacity of Li-air batteries is comparable to LHCs but still less. In addition, Li-air battery technology is not expected to achieve its full predicted useful specific energy within the next decade [9]. Table 1 [9] shows the theoretical specific energy of Li-air (Li-O_2) batteries (and others) and their expected energy capacity in 2025.

Table 1. Predicted specific energies of different batteries.

System	Theoretical Specific Energy (MJ/kg)	Expected Specific Energy in 2025 (MJ/kg)
Li-ion	1.4	0.9
Zn-air	3.92	1.44-1.8
Li-S	9.25	1.8-4.5
Li-O_2	12.6	2.88-6.3

The highest predicted specific energy for a lithium-air battery in the next decade is 6.3 MJ/kg, which is only 37% of the current lowest practical energy capacity of aviation fuel. Therefore, battery-powered aircraft with comparable range would incur substantial penalties in useful load from the added mass of the batteries.

Not only do batteries have less energy capacity than aviation fuel, they are also more costly. The nationwide average price per gallon of Jet-A in August 2015 was $5.20 [12], which translates to ~$0.09/MJ when considering the practical specific energy of the fuel. Boeing estimates the lowest price for the 2.7 MJ/kg battery needed to drive the electric motor in the SUGAR Volt design to be $44/kg [13], which equates to $16.29/MJ. Other factors such as improvements in battery design and production/availability are necessary to drive down the costs significantly to the levels of LHCs.

Based on energy and cost considerations, LHCs will likely remain the sole source of chemical potential energy required for propulsion systems in the foreseeable future. As such, any vehicle with a significant component of electrically driven propulsion will require a system for converting energy stored in fuel to electric power. Catalytic partial oxidation reactor (CPOx)/solid oxide fuel cell (SOFC) systems offer a promising method of energy conversion because they can operate on reformates from LHCs such as aviation fuel and are much more tolerant of carbon and sulfur compounds present in such fuels.

1.1.3 Fuel Consumption

The ‘relative’ fuel mass flow rate [1] is one way to quantify the effect of electric power generation on vehicle performance. The relative fuel flow rate is defined as the ratio of a vehicle’s fuel flow rate at cruise to the fuel flow rate at cruise when no electrical power is being delivered. Thus, it is a number greater than one that increases with increasing electric power demand. Waters derived a closed-form expression for the relative fuel flow rate based on thrust specific fuel consumption of the propulsive engine ($TSFC$), specific energy of the fuel (Q_f), efficiency of the electrical conversion system (η_{elec}), mass of the electrical generation components (m_{elec}), cruise speed (v), electric power fraction (ζ), gravitational acceleration (g), a characteristic surface area (S), and the vehicle’s drag polar (C_{Dmin}, C_{Lmin}, K) [1]:

$$\dot{m}_f{}' = \left(1 + \frac{v}{(TSFC)Q_f\eta_{elec}}\left[\frac{\zeta}{1-\zeta}\right]\right)\frac{\left[C_{Dmin} + K\left(\frac{(m_0 + m_{elec})g}{\frac{1}{2}\rho v^2 S} - C_{Lmin}\right)^2\right]}{\left[C_{Dmin} + K\left(\frac{m_0 g}{\frac{1}{2}\rho v^2 S} - C_{Lmin}\right)^2\right]} \tag{2}$$

In order to understand the effect of electrical power generation on the performance of a small UAV, relative fuel flow rate is plotted as a function of electric power fraction for Northrop Grumman’s BQM-74E-Chukar-III at cruise (see Figure 2). The figure shows that the efficiency at which electric power is produced on board can have a significant effect on overall fuel consumption and thus on range and endurance. Flight conditions and aircraft specifications [14] used to generate the plots in Figure 2 are summarized in Table 2.

Table 2. Flight conditions and aircraft specifications for preliminary relative fuel flow rate calculations.

Flight Conditions	
Mach (M)	0.5
Altitude	40 kft
ρ	0.301 kg/m^3
v	147.5 m/s
Aircraft Specifications	
$TSFC$	33.99 g/kN/sec
Q_f	44 MJ/kg
$\eta_{e.gen.}$	0.4
η_{FC}	0.6
S	0.697 m^2
m_0	206.4 kg
Total rated thrust	1068 N

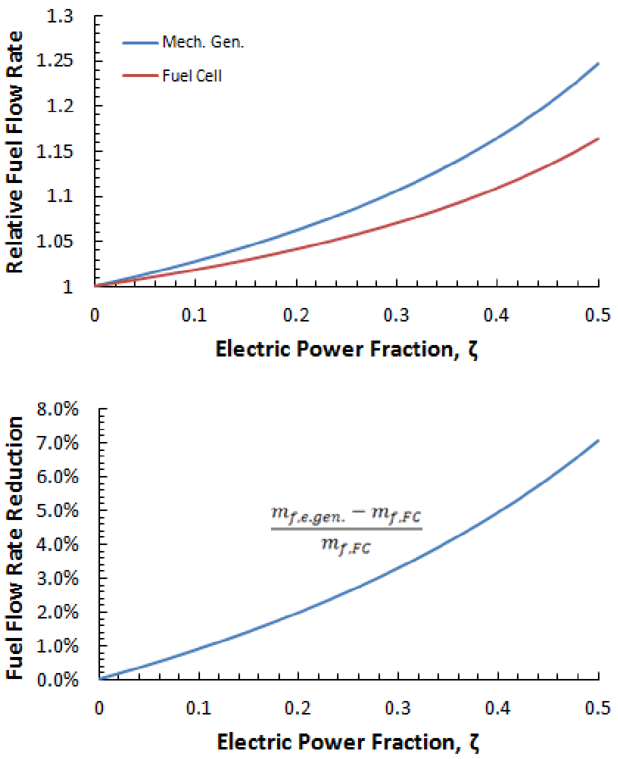

Figure 2. (Top) Relative fuel flow rate vs. electric power fraction; (Bottom) Fuel flow rate reduction vs. electric power fraction.

The top plot in Figure 2 shows that a fuel cell based system consumes less fuel than a mechanical generator based system because of the higher electrical conversion efficiency of the fuel cell. The bottom plot of Figure 2 shows that fuel savings increase with electric power fraction. There is about a 5% and 7% reduction in fuel flow rate from a generator system for electric power fractions of $\zeta = 0.4$ and $\zeta = 0.5$, respectively. For this highly simplified analysis, the electrical system mass and any coupling effects between the engine and fuel cell are neglected.

Since this thesis involves turbine/fuel cell hybrids, it is useful to briefly review the operating principles of turbojet engines and fuel cells.

1.2 Turbojets

1.2.1 Fundamentals of Turbojet Operation

Turbojets are a class of gas turbines that utilize the Brayton thermodynamic cycle to produce thrust. In a turbojet, air enters the inlet and is compressed using centrifugal or axial turbomachinery called a compressor. After exiting the compressor, air enters the combustor/burner where energy in the form of heat is added to the flow due to combustion. Following combustion, air is expanded through a turbine that drives the compressor. The air exiting the turbine is accelerated through a nozzle to produce thrust. An after-burner stage may also be present between the turbine and nozzle where additional fuel is injected and burned to increase the energy of the flow. The engine considered in this work does not have an after-burner stage. Figure 3 is a schematic illustration of a turbojet with ‘standard’ stage numbering [10].

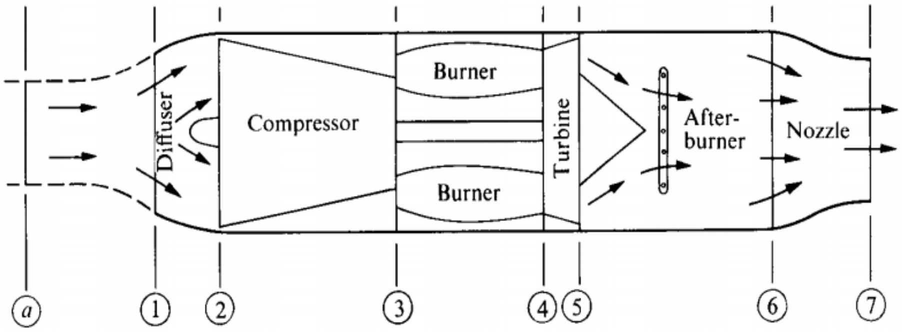

Figure 3. Schematic of a turbojet engine [10]**.**

The simplest representation of the turbojet's thermodynamics is the ideal Brayton cycle in which the working fluid (air in the case of aircraft engines) is subjected to four processes [15]: isentropic compression, isobaric heat addition, isentropic expansion, and isobaric heat rejection. These processes are illustrated using pressure-volume and temperature-entropy diagrams in Figure 4 [16]. It is assumed here that there is no after-burner stage so the nozzle exit is indicated by stage 6 (and not stage 7). All processes in the ideal turbojet cycle are assumed to be reversible.

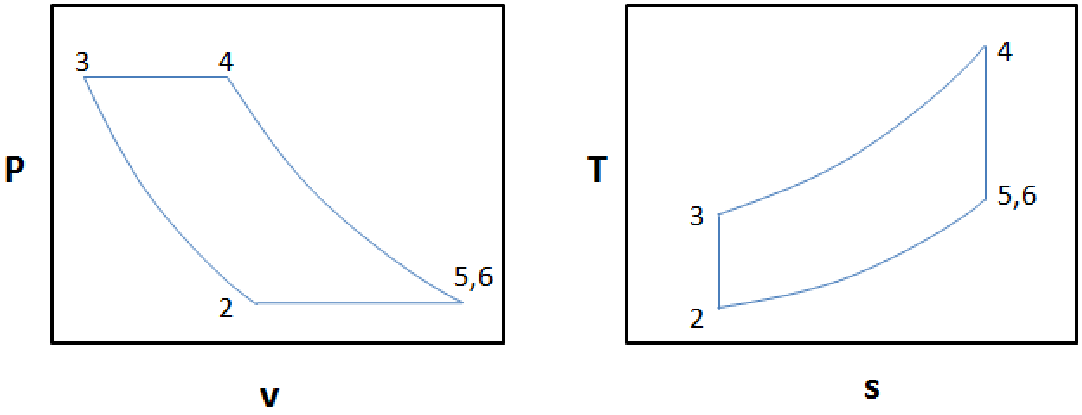

Figure 4. P-v and T-s diagrams of the ideal Brayton cycle.

The net work per unit mass of the ideal Brayton cycle is expressed as a function of temperatures at each stage in the thermodynamic cycle for constant C_p [17]:

$$Net\ Work = C_p(T_4 - T_3) - C_p(T_{5,6} - T_2) \tag{3}$$

In Eq. (3), T_2 is the ambient temperature and the assumption of isentropic flow constrains the values of T_3 and $T_{5,6}$. This means that maximizing T_4 maximizes the net work of the ideal cycle [15]. However, T_4 cannot be increased indefinitely as it is generally limited by material properties of the turbine inlet.

The thermal efficiency of the ideal turbojet cycle is defined as the ratio of the net work to heat addition in the burner. Following the relationship for specific work in Eq. (3), the thermal efficiency can be expressed in terms of temperatures for a calorically perfect gas [17]:

$$\eta = \frac{Net\ Work}{Heat\ Addition} = \frac{C_p(T_4 - T_3) - C_p(T_{5,6} - T_2)}{C_p(T_4 - T_3)} \tag{4}$$

The combustion and heat rejection processes are assumed to be isobaric. The other two processes are assumed to be isentropic [15] so:

$$\left(\frac{T_{5,6}}{T_4}\right)^{\gamma/(\gamma-1)} = \left(\frac{T_2}{T_3}\right)^{\gamma/(\gamma-1)} \tag{5}$$

Therefore, $T_{5,6}/T_4 = T_2/T_3$, and the expression for thermal efficiency of the Brayton cycle can be rewritten as a function of ambient temperature and the compressor exit temperature:

$$\eta = 1 - \frac{T_2}{T_3} \tag{6}$$

Using isentropic relations, Eq. (6) can be written in terms of the engine’s compression ratio:

$$\eta = 1 - \frac{T_2}{T_3} = 1 - \frac{1}{(P_3/P_2)^{(\gamma-1)/\gamma}} \tag{7}$$

This expression shows that higher compression ratios lead to higher cycle efficiencies. For fixed ambient and burner exit temperatures, there is also an optimum compression ratio that maximizes the net work of the cycle [15]:

$$\left[\frac{P_3}{P_2}\right]_{max\,work} = \left(\frac{T_4}{T_2}\right)^{\frac{\gamma}{2(\gamma-1)}} \tag{8}$$

A real turbojet engine is not a closed cycle as described above for the ideal Brayton cycle, but rather an open cycle where the working fluid (air) is expelled after the expansion process instead of performing the isobaric heat rejection. While none of the engine's components are actually reversible, they are assumed to be adiabatic in this idealized analysis. Also, fluid velocities in the engine are not negligible (necessary for flame stabilization in the combustor), and the turbine and compressor flow rates are not equal because of the potential bleed flows for cooling and the addition of fuel during combustion [10].

An adiabatic efficiency for the compression process in a real turbojet can be defined as the ratio of work required in an isentropic process to that required in the real process [10]:

$$\eta_c = \frac{h_{03s} - h_{02}}{h_{03} - h_{02}} \tag{9}$$

Similarly, the adiabatic efficiency of the expansion process in the turbine is defined as [10]:

$$\eta_t = \frac{h_{04} - h_{05,06}}{h_{04} - h_{05s,06s}} \tag{10}$$

Burner efficiency can be defined as well, which is the fraction of chemical energy stored in fuel that is released during combustion [10]. This efficiency is generally close to unity, as there is usually complete combustion of the fuel. Other engine components such as the inlet/diffuser and nozzle introduce losses, but they are typically small and have little effect on overall performance.

1.2.2 Applications of Small Turbojet Engines

In recent years, small-scale turbojet engines have become attractive propulsive platforms for small manned aircraft, UAVs, and for research applications where larger turbojets are not easily accessible.

Figure 5. Clockwise from top left: SubSonex, JB-9 Jetpack, Jetman Dubai Wing Suit, BQM-74E-Chukar-III[1].

PBS Aerospace manufactures small turbojet engines for police/military (reconnaissance, target drones, missiles, etc.) and recreational applications (gliders,

---

[1] Image sources, all accessed 9/6/2016:
SubSonex (http://www.sonexaircraft.com/press/releases/pr_020714.html)
JB-9 Jetpack (http://jetpackaviation.com/the-jumpjet/jb-9/)
Jetman Dubai Wing Suit (http://i.dailymail.co.uk/i/pix/2014/12/12/24007F4E00000578-2871768-image-m-60_1418402049123.jpg)
BQM-74E-Chukar-III (http://www.northropgrumman.com/MediaResources/Pages/Photo.aspx?pid%3DTG-10032_022%26rel%3D%2F%26name%3DPhotos)

light sport and experimental aircraft, etc.) [18]. PBS Aerospace’s TJ100 turbojet engine (1300 N thrust) [19] is currently employed on Sonex’s SubSonex sport aircraft [20]. The TJ100 has also been refined and optimized for use in reconnaissance UAVs and target drones [19]. Smaller turbojet engines manufactured by PBS Aerospace such as the TJ40 (395 N thrust) and the TJ20 (210 N thrust) are more suited for target and decoy drones [18]. Other small turbojet manufacturers such as AMT Netherlands, JetCat, and Jet Central produce engines of comparable size and applications. Two of AMT Netherlands’ Nike engines (784 N thrust) power JetPack Aviation’s JB-9 jetpack [21]. This work uses AMT Netherlands’ Olympus HP (230 N thrust). Jetman Dubai’s jet-propelled wing suit is powered by four of JetCat’s P400 turbojet engines (391 N thrust) [22]. Northrop Grumman’s BQM-74E-Chukar-III is a turbojet-powered aerial target drone that simulates enemy tactical cruise missiles or fighter aircraft and is heavily employed by the U.S. Navy [14]. Its powerplant is a single Williams J400-WR-404 turbojet with a maximum thrust of 1068 N.

Because large-scale turbojets are often too complex and expensive to operate in a laboratory setting, many research universities and institutions employ smaller turbojets for this purpose. Benini and Giacometti [23] describe the development of a 200 N static-thrust engine at the University of Padova designed specifically for educational and research activities. The development of small-scale turbojet engines for research purposes has been investigated by others as well [24], [25]. Industry has also developed small turbojet engines specialized for lab-scale testing, such as the SR-30 turbojet produced by Turbine Technologies [26]. Badami et al. [27] perform an experimental and numerical analysis of the thermodynamic cycle of the SR-30 for use in later studies of examining the use of alternative fuels in gas turbine engines. AMT Netherlands offers modifications to their existing gas turbine models for static testing. This work uses AMT's Olympus HP turbojet in "University Configuration", meaning the engine comes equipped with stagnation temperature and pressure measurement ports at each axial stage along the engine [28]. AMT engines in "University Configuration" also come with an analog throttle controller for ground testing. The AMT Olympus HP is a popular turbojet model at other universities as well [29]–[35].

1.3 Fuel Cells

1.3.1 Fundamentals of Fuel Cell Operation

Combustion engines convert chemical potential energy stored in a fuel stream into thermal power, the thermal power into mechanical power, and then the mechanical power into electrical power via a mechanical generator. Fuel cells convert chemical energy in a fuel stream directly to electrical power. While this single-step electrical conversion process is usually much more efficient than the multi-step process associated with engines, the fuel cell requires other 'balance of plant' components like pumps, blowers, controls, etc. whose losses significantly degrade the overall performance of the energy conversion system.

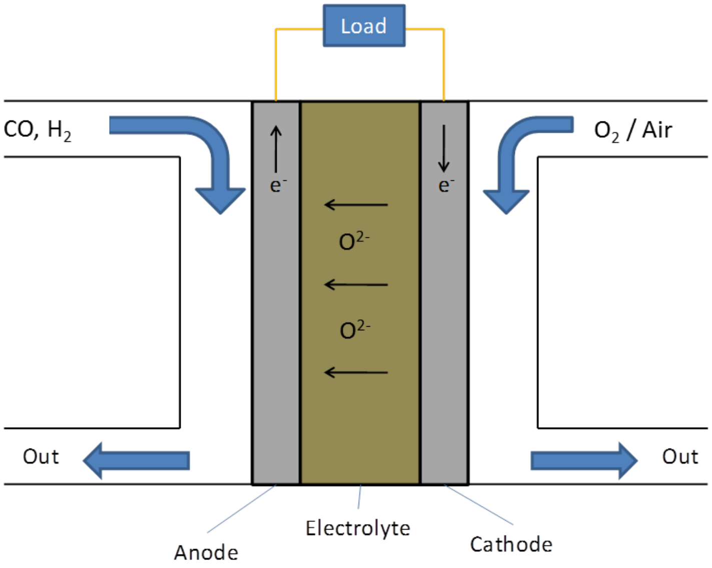

Figure 6. Schematic of a solid oxide fuel cell [1]**.**

A schematic illustration of a solid oxide fuel cell is shown in Figure 6 [1]. A hydrogen ion (or proton) carrier such as hydrogen or carbon monoxide gas enters the anode side of the fuel cell and an oxidizer such as oxygen or air enters the cathode side. Oxidation and reduction reactions occur at the anode and cathode. O^{2-} ions are transported from the cathode across a solid ceramic electrolyte to the anode, where oxidation occurs. This is in contrast to a PEM fuel cell, where H^+ ions (protons) are transported across the electrolyte. Electrons cannot flow through the electrolyte, so instead they flow from the anode to the cathode through a load to produce electrical power. Other types of fuel cells will be discussed shortly.

The following reaction occurs at the anode [36]:

$$\text{Anode:} \quad H_2 + O^{2-} \rightarrow H_2O + 2e^- \tag{11}$$

The electrons produced in this oxidation reaction flow through the external load on their way back to the cathode where they complete the reaction. The reduction reaction that occurs at the cathode is given by [36]:

$$\text{Cathode:} \quad O_2 + 4e^- \rightarrow 2O^{2-} \tag{12}$$

The O^{2-} ions produced at the cathode diffuse across the electrolyte to complete the oxidation reaction in the anode. Thus, it is essential that the electrolytic membrane has physical properties that allow the transport of O^{2-} ions without conducting electrons. The total electrical power produced by the fuel cell is the product of the current and electric potential across the fuel cell.

The variation of fuel cell voltage with pressure is given by [36]:

$$\left(\frac{\partial V_{rev}}{\partial P}\right)_T = -\frac{1}{nF}\left(\frac{\partial\,\Delta\,g}{\partial P}\right)_T = -\frac{\Delta\,v}{nF} \tag{13}$$

where n is the number of electrons in the reaction. Eq. (13) shows that the change in reversible fuel cell voltage with pressure is related to the change in specific volume of the reaction. If there is a negative change in reaction volume (i.e., less moles of product than reactants), the cell voltage will increase with increasing pressure according to Le Chatelier's principle [16]. Assuming the ideal gas law is applicable, Eq. (13) can be written as [36]:

$$\left(\frac{\partial V_{rev}}{\partial P}\right)_T = -\frac{\Delta NRT}{nF}\frac{1}{P} \tag{14}$$

Similar to Eq. (13), for reactions with $\Delta N < 0$ the reversible cell voltage will increase with increasing pressure. Equations (13) and (14) show that increasing the operating pressure enables a fuel cell to produce more power with the same current density. This means the higher pressure system operates at a higher voltage and more efficiently. While there are diminishing returns because the derivative in Eq. (14) is inversely proportional to pressure, it suggests that placing the fuel cell in parallel with the combustor and thus at elevated pressure should improve performance.

The cycle efficiencies of engines and fuel cells have different temperature dependences. The maximum theoretical efficiency of any heat engine is the Carnot efficiency [37]:

$$\eta_{carnot} = 1 - T_L/T_H \tag{15}$$

In Eq. (15), T_L and T_H are the temperatures of the low and high temperature reservoirs in the heat engine cycle. The Carnot efficiency is the maximum efficiency allowed by the second law of thermodynamics. However, a Carnot efficiency of unity is physically impossible because this would require the low reservoir temperature to be absolute zero or an infinitely high reservoir temperature.

The maximum theoretical efficiency achieved by any fuel cell is given by [37]:

$$\eta_{fc,max} = W_{max}/-\mathit{\Delta} H = \mathit{\Delta} G/\mathit{\Delta} H = (\Delta H - T\Delta S)/\Delta H \tag{16}$$

where ΔH is the change in sensible enthalpy and ΔG is the change in Gibbs free energy. The change in Gibbs free energy decreases with increasing temperature in any real process with an entropy change. Thus, a fuel cell’s efficiency decreases with increasing operating temperature whereas a heat engine’s increases. This is illustrated in Figure 7 [1].

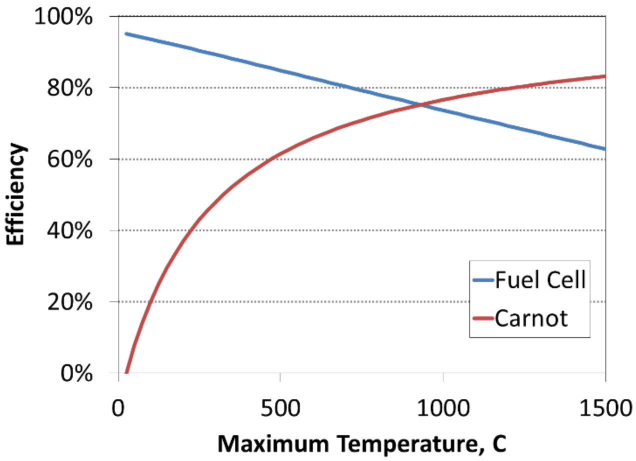

Figure 7. Efficiencies of ideal heat engine and fuel cell vs. temperature [1]**.**

The Carnot efficiency curve in Figure 7 assumes that $T_L = 298\,K$, and the fuel cell curve was generated for a fuel cell operating at 1 atm, where the oxidizer is air and the fuel is composed of 80% hydrogen and 20% water vapor [1]. Figure 7 shows that fuel cell efficiency is greatest at low temperatures, whereas heat engine efficiency is greatest at high temperatures. The efficiencies in Figure 7 depict the maximum theoretical efficiencies. These efficiencies are not attainable in real systems, so comparisons between heat engines and fuel cells must be made based on practical performance of these systems.

There are five major types of fuel cells which are mainly differentiated by their electrolytes [36]:

1. Phosphoric acid fuel cell (PAFC)
2. Polymer electrolyte membrane fuel cell (PEMFC)
3. Alkaline fuel cell (AFC)
4. Molten carbonate fuel cell (MCFC)
5. Solid oxide fuel cell (SOFC)

PAFCs use liquid H_3PO_4 (phosphoric acid) contained in a SiC matrix between porous electrodes coated with a platinum catalyst to form the electrolyte [36]. PEMFCs employ a polymer electrolyte membrane that conducts protons [36]. AFCs are constructed from a liquid potassium hydroxide electrolyte where OH^- ions diffuse from the cathode to the anode [36]. The electrolyte in MCFCs is a molten mixture of alkali carbonates (Li_2CO_3 and K_2CO_3) in a matrix of $LiOAlO_2$, where the carbonate ion CO_3^{2-} is the charge carrier [36]. SOFCs generally contain ceramic electrolytes such as yttria stabilized zirconia (YSZ) that conduct oxygen ions [36]. For SOFCs, the diffusion of oxygen ions across the YSZ electrolyte membrane is most effective at high fuel cell operating temperatures. For example, the conductivity of YSZ at 800°C is about 0.02 S/cm and increases to 0.1 S/cm at 1000°C [37]. Therefore, SOFCs require high operating temperatures and a thin YSZ membrane. Advantages of a high operating temperature include fuel flexibility and the ability to utilize a cogeneration scheme with the wasted heat generated from the fuel cell.

The anode electrode in SOFCs must be able to withstand the highly reducing environment of the fuel-side reaction and high operating temperatures of the fuel cell. The most common choice for anode material is a nickel-YSZ cermet – a mixture of ceramic and metal [36]. Nickel provides effective electron conductivity and serves as an effective reaction catalyst. The YSZ provides porosity and mechanical stability to the anode and has resilient thermal properties. Similarly, the cathode electrode must have sufficient porosity to allow the diffusion of reactants and serve as an effective electron conductor. The cathode material must also be well-suited for the highly oxidizing air/oxidizer-side reaction and of course the high fuel cell temperatures.

Common electrode cathode materials for SOFCs are strontium-doped lanthanum manganite, lanthanum-strontium ferrite, lanthanum-strontium cobaltite, and lanthanum strontium cobaltite ferrite [36]. These materials exhibit sufficient diffusive and conductive properties, and offer high catalytic activity for the cathode reaction.

As stated above, one of the advantages of SOFCs is their carbon tolerance (due to their high operating temperature) which enables them to operate on syngas (mixtures of H_2, CO, and CO_2) and other hydrocarbon reformates. While this enables SOFCs to consume energy dense fuels like liquid hydrocarbons (LHCs), a separate reformer such as a catalytic partial oxidation reactor (CPOx) is usually required. However, this adds complexity and balance of plant components to the fuel cell system that reduce overall system efficiency. Other advantages of SOFCs include the use of non-precious metal catalysts (which reduces cost) and their relatively high power density which is essential for aerospace applications where lower mass components are preferred.

Despite the benefits offered by SOFCs, they have several shortcomings. High operating temperatures present issues with thermal management. They also require the use of fragile ceramic materials in the membrane-electrode assembly that are prone to fracturing. Thus, it is important to minimize thermal gradients and manage cyclic heating and cooling carefully. Sealing is also a challenge as most sealants cannot withstand the high temperatures. In spite of the high operating temperatures, contamination and poisoning remain significant problems because syngas from aerospace fuels can contain high levels of sulfur that has been shown to inhibit the Ni catalyst activity in the anode [38]. Thus, the ‘fuel processor’ may have to contain other components besides a reformer and this drives up the size of the system and the balance of plant losses associated with its operation. For example, a fuel cell stack from Ballard Power Systems weighs 0.8-9 kg per kW of electrical output, but the full system weighs roughly 15-110 kg per kW [39]. The balance of plant components can also be significantly more expensive than the fuel cell stack [40].

SOFCs commonly use catalytic partial oxidation (CPOx) reactors as fuel reformers. A CPOx is typically made with porous alumina foams coated in a catalyst [41]–[43]. Such foams are ceramic and achieve porosities of 80-90%, resulting in minimal pressure losses [44]. Catalysts for the foams can be made from platinum [42] or rhodium [38], [43]. At high operating temperatures, well designed CPOx reformers can operate close to chemical equilibrium [38].

CPOx reactors operate fuel rich (with less than stoichiometric oxygen (O_2) concentrations) to partially combust (or oxidize) the fuel into hydrogen (H_2) and carbon monoxide (CO). The partial oxidation of propane is shown in Eq. (17) and can be compared to the complete (stoichiometric) oxidation of propane with O_2 in Eq. (18).

$$C_3H_8 + \frac{3}{2}O_2 \rightarrow 3CO + 4\,H_2 \tag{17}$$

$$C_3H_8 + 5\,O_2 \rightarrow 3CO_2 + 4\,H_2O \tag{18}$$

For any hydrocarbon fuel, partial oxidation is defined as:

$$C_xH_y + \frac{x}{2}O_2 \rightarrow x\,CO + \frac{y}{2}H_2 \tag{19}$$

In Eq. (19), x is the number of carbon atoms and y is the number of hydrogen atoms.

1.3.2 Applications of Fuel Cells in Aircraft

Fuel cell technology has already been incorporated onto aircraft as the sole powerplant for propulsion. This is in contrast to the current work that aims to advance the development of a hybrid GT/SOFC system for combined propulsion and electric power generation.

Figure 8. Clockwise from top left: Ion Tiger, Intelligent Energy's Quadrotor Prototype, Boeing's Experimental FC Aircraft[2].

The U.S. Naval Research Laboratory's Ion Tiger UAV employs a 550 W hydrogen fuel cell as its propulsion system and can carry a 5 lbf (22.2 N) payload [45]. Recent development of a cryogenic fuel storage tank and delivery system for liquid hydrogen fuel allowed the Ion Tiger to successfully complete a 48-hour long flight [46]. Intelligent Energy has recently developed a small quadrotor prototype powered by a hybrid hydrogen fuel cell/battery system and has been able to extend

---

[2] Image sources, all accessed 9/7/2016:
Ion Tiger (http://www.naval-technology.com/projects/ion-tiger-uav/)
Intelligent Energy's Quadrotor Prototype (http://www.intelligent-energy.com/news-and-events/company-news/2015/12/15/intelligent-energy-hydrogen-fuel-cells-significantly-extend-drone-flight-time/)
Boeing's Experimental FC Aircraft (http://www.popularmechanics.com/flight/a2761/4257294/)

the UAV's endurance by several hours [47]. The successful demonstration of their quadrotor drone in early 2016 has led to collaboration with a major drone manufacturer [48]. Boeing has successfully flown a small manned aircraft powered by a hybrid PEM fuel cell/lithium ion battery propulsion system [49]. The airframe for Boeing's experimental aircraft was a two-seat Dimona motor-glider. Despite the success of this small fuel cell-powered aircraft, Boeing researchers do not believe fuel cells will ever provide primary power for larger commercial aircraft [49]. This sentiment validates the need for investigating hybrid technology such as GT/SOFC systems to power aircraft with larger payload requirements.

1.4 Gas Turbine/Solid Oxide Fuel Cell Hybridization

1.4.1 Advantages of System Coupling

Integrating a CPOx reactor and SOFC into the flow path of a gas turbine engine for combined propulsion and power has already shown to have potential benefits [1], [50]. The CPOx/SOFC system would replace conventional generators and auxiliary power units on aircraft. A schematic of a turbojet GT/SOFC is illustrated in Figure 9 [1].

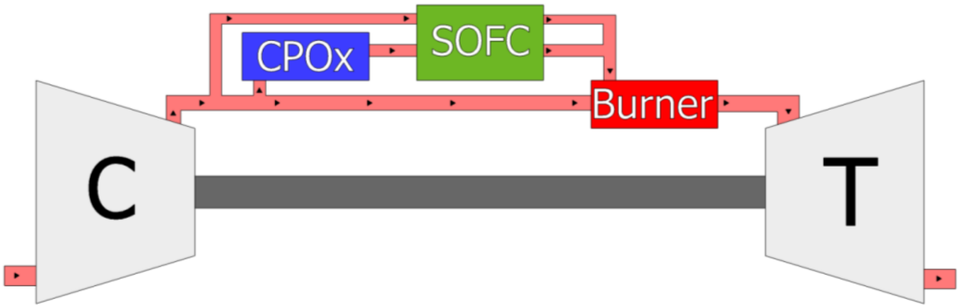

Figure 9. Schematic of a turbojet GT/SOFC [1]**.**

In the proposed GT/SOFC system, bleed air exiting the compressor is supplied to the CPOx/SOFC system. The bleed air provides cooling for the system and oxidizer for the cathode of the fuel cell. Although not indicated in Figure 9, the CPOx also receives its own fuel supply. Unused fuel and products from the CPOx/SOFC reaction are fed back into the burner of the turbojet to be recovered in the Brayton cycle. A hypothetical layout of a turbojet GT/SOFC with the SOFC in an annular duct around the engine is depicted in Figure 10 [1].

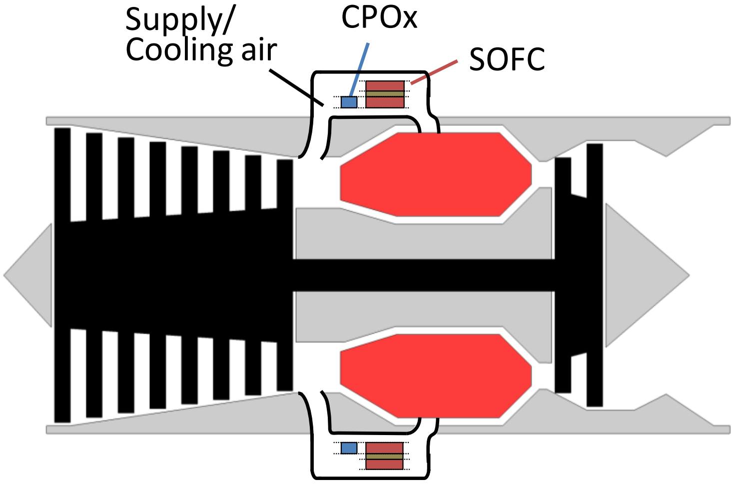

Figure 10. Engine layout of turbojet GT/SOFC [1]**.**

The coupled behavior between the gas turbine and SOFC present several advantages for the hybrid system. Many fuel cell balance of plant functions are absorbed by the gas turbine. For example, the fuel cell does not need separate pumps or blowers because the gas turbine supplies air to the system. Air provided by the gas turbine is pressurized from the compressor stage, improving fuel cell efficiency and power density. The pressurized air is also heated, further improving fuel cell conversion and making it easier to maintain the membrane electrode assembly at the proper temperature. Unreacted fuel and waste heat generated by the CPOx/SOFC system is recovered in the Brayton cycle when products from the reaction flow into the burner. In addition, the faster transient response of the Brayton cycle could improve the transient response of the fuel cell.

1.4.2 Challenges

Pressure losses associated with the CPOx/SOFC system could have detrimental effects on overall performance of the gas turbine. Although the porous alumina foam catalyst in the CPOx has relatively low pressure drop compared to other catalysts [44], the losses can still be significant. Pressure losses due to friction will also occur in the flow channels of the SOFC. Additional pressure losses will arise from bleeding air from the compressor stage of the GT and reintroducing the flow back into the burner. When designing the physical hybrid system, it is essential that the pressure drop across the CPOx/SOFC is no greater than the pressure drop incurred in the GT combustor. If the CPOx/SOFC pressure drop is greater than that across burner, air will not flow into CPOx/SOFC assembly or the gas turbine will encounter further losses in the Brayton cycle. Physical integration of the fuel cell exhaust paths with the burner is another challenge facing the design of a hybrid system. Modifications to the burner will likely add mass to the system, and altering the flow path could result in combustion instability. The effect of introducing low molecular weight fuel species such as H_2 and CO into the combustion process could also be unpredictable. Furthermore, injecting SOFC exhaust upstream of the turbine stage of the gas turbine could result in severe complications. If ceramic materials in the SOFC were to fracture due to excessive heating or impact, the debris could enter the combustor and turbine. This debris would cause damage to the turbine blades and reduce turbine efficiency or at worst cause catastrophic engine failure.

1.4.3 Literature Review of GT/SOFC Systems

A summary of the literature investigating hybrid GT/SOFC systems is presented in Table 3 [1]. Most of the work on engine-integrated SOFCs has been focused primarily on stationary power generation in terrestrial applications. Research on GT/SOFC systems for airborne applications is typically focused on replacing existing APUs with FC technology. These APU applications are strictly for electrical power generation and are separate from the main propulsion of the aircraft. Only a few studies have investigated hybrid GT/SOFC systems for combined propulsion and electrical power generation.

Recent studies conducted at the University of Maryland [1], [50] have further explored the potential benefits of a GT/SOFC system for combined propulsion and power on aircraft. Waters and Cadou develop Numerical Propulsion System Simulation (NPSS) thermodynamic models of SOFCs, CPOx reactors, and multiple GT engine types [1], [50]. The models account for realistic equilibrium gas phase and electrochemical reactions, pressure losses, and heat losses. It is shown that hybrid systems can reduce fuel consumption by 3-4% for a 50 kW SOFC system integrated with a 35 kN rated engine. Larger reductions of 15-20% are predicted for 200 kW systems. Waters and Cadou also show that GT/SOFC systems can produce more electric power than mechanical generator-based systems before reaching turbine inlet temperature limits. Finally, Waters and Cadou examine the aerodynamic drag effects of engine-airframe integration of the SOFC assembly. Ultimately, the studies performed by Waters and Cadou show that integrated GT/SOFC systems for combined propulsion and power exhibit better overall performance than powerplants with separate components. Although hybrid GT/SOFC systems appear to offer better performance than mechanical generator- or APU-based systems, it appears no studies to date have proposed constructing a physical prototype.

Table 3. Summary of GT/SOFC literature [1].

Authors	Platform	Size	Reformer/FC	Fuel	FC model	GT model	Efficiency	Notes
Ground-based:								
Calise et. al. [51]	MATLAB	1.5 MW	IR-SOFC	Natural Gas	Validated vs. data	Performance maps	η_{elec}=68%, η_{sys}>90%	Cost optimization
Haseli et. al. [52]	MATLAB	2.4 MW	IR-SOFC	Methane	Zero-D	Constant efficiencies	η_{sys}=60%	Focus on irreversibilities
Abbasi & Jang [53]		132 kW	IR-SOFC		Zero-D	Constant efficiencies		Power conditioning; transient response
Chan et. al. [54]		2.1 MW	IR-SOFC	Natural Gas	Zero-D, validated vs. data	Constant efficiencies	η_{elec}=62%, η_{sys}=84%	
Palsson et. al. [55]	Aspen Plus	500 kW	pre-reformer, SOFC	Methane	2-D, validated vs. literature	Aspen Plus std. models	η_{elec}=60%, η_{sys}=86%	Combined power and heat prod.
Costamaga et. al. [56]	MATLAB	300 kW	steam ref., SOFC	Natural Gas	Zero-D	Performance maps	η_{sys}>60%	On and off-design analysis
Lim et. al. [57]	Experiment	5 kW	pre-reformer, SOFC	Natural Gas				Working on GT-SOFC
Suther et. al. [58]	Aspen Plus		steam ref., SOFC	Syngas	Zero-D	Aspen Plus std. models		
Zhao et. al. [59]				Coal syngas	Zero-D	Ideal GT	η_{sys}=50-60%	
Leto et. al. [60]	IPSE Pro	140 kW	IR molten carbonate	Natural Gas	Zero-D	IPSE Pro std. models	η_{sys}=60-70%	
Veyo et. al. [61]		300 kW, 1MW		Natural Gas			η_{sys}=59%	
APUs:								
Freeh et. al. [62]	NPSS	200 kW	steam ref., SOFC	Jet-A	Zero-D, validated vs. data	Performance maps	η_{elec}=65%, η_{sys}=40%	
Steffen et. al. [63]	NPSS	440 kW, 1396 kg	steam ref., SOFC	Jet-A	Zero-D	Performance maps	η_{sys}=62%	
Freeh et. al. [64]	NPSS	440 kW	steam ref., SOFC	Jet-A	Zero-D	Performance maps	η_{sys}=73%	On and off-design analysis
Eelman et. al. [65]	MATLAB	370 kW	steam ref., PEM + SOFC	Jet fuel			SOFC: η_{sys}>70%, PEM: η_{sys}>35%	Aircraft integration approaches
Rajashekara et. al. [66]		440 kW, >880 kg	steam ref., SOFC	Jet fuel	Zero-D		SL: η_{sys}=61%, Cruise: η_{sys}=74%	
Braun et. al. [67]	UTRC prop.	300 kW	autothermal ref., SOFC	Jet-A			SL: η_{sys}=53%, Cruise: η_{sys}=70%	
All-Electric:								
Himansu et. al. [68]	MATLAB	20 kW, 50kW	SOFC	H_2	Zero-D	Constant efficiencies		
Aguiar et. al. [69]		140 kW	SOFC	H_2		Constant efficiencies	Single: η_{sys}=54%, Multi: η_{sys}=66%	Multiple stacks: fuel in parallel, air in series
Bradley & Droney [70]	Spreadsheet		SOFC	H_2	Zero-D			
Bradley & Droney [71]	GE prop.		SOFC	LNG				SFC ~0.125 lb/lbf/hr

1.5 Objectives

The overall objective of this research program is to take initial steps toward constructing a bench-scale prototype of a hybrid GT/SOFC so that the challenges associated with building a practical, flight-ready system may be identified. The first step is to develop experimentally validated thermodynamic models of the gas turbine and SOFC as separate components. The separate models will be combined to develop a model of the hybrid GT/SOFC system that, in turn, can be used to design the bench-scale prototype.

The foci of this thesis are the development and experimental validation of a thermodynamic model for a small gas turbine engine suitable for building a bench-scale GT/SOFC hybrid.

1.6 Previous Work

Since this thesis focuses on the development of an experimentally validated model of a small GT needed to construct a bench-scale GT/SOFC system, an investigation of previous testing and modeling of small gas turbines is also necessary. Numerous studies have already investigated performance of the AMT Olympus turbojet engine considered in this work [29]–[35]. Horoufi and Boroomand [32], Grzeszczyk et. al. [31], and Laskaridis et. al. [33] focus on the development of a test facility and performance of the AMT Olympus. Horoufi and Boroomand develop an outdoor test bed that measures RPM, thrust, fuel flow rate, compressor exit temperature, and exhaust gas total temperature [32]. As is done in this work, Horoufi and Boroomand calibrate their thrust stand using a cable/pulley system and measure fuel flow gravimetrically [32]. Grzeszczyk et. al. measure thrust, fuel flow rate, RPM, and all axial stage temperatures/pressures measured in this work (discussed later), but they do not measure air flow rate (as is done in this work). Grzeszczyk et. al. measure fuel flow volumetrically using a flow meter, and they also measure engine vibration [31]. Laskaridis et. al. use CFD to optimize the aerodynamic performance of an enclosed (indoor) test cell that imitates full-scale test cells for larger turbojet engines [33]. Laskaridis et. al. focus more on design of the test facility instead of measuring performance of the Olympus.

References [29], [30], [34], [35] focus on both experimental and numerical analysis of the Olympus. Al-Alshaikh measures thrust, RPM, fuel flow rate, air mass flow rate, flow velocities inside the test cell, pressure distribution inside the test cell, and temperatures at the inlet/exit of the test cell, engine, and detuner [29]. Al-Alshaikh uses the CFD package Fluent to predict performance of the Olympus [29]. Bakalis and Stamatis measure compressor exit total/static pressure and total temperature, turbine inlet total temperature and pressure, turbine exit total/static pressure and total temperature, RPM, fuel flow rate, and thrust [30]. As in this work, Bakalis and Stamatis use scaled compressor and turbine performance maps for off-design performance estimation. They experienced difficulty matching the measured and model-predicted TIT (as was the case in this work too). However, they found that recalibrating their model based on static pressure instead of total pressure measurements at the turbine produced more reasonable predictions. Leylek measures thrust, air flow rate, fuel flow rate, RPM, and the internal stage temperatures and pressures [34]. Leylek models the engine’s thermodynamic cycle using a combination of methods that include: the commercially available Gasturb code and a python script for overall performance simulation, CFD (Fluent and Numeca), Meanline and ThroughFlow empirical tools, and map scaling for turbomachinery performance, and empirical loss models for the combustor and ducts/nozzle performance [34]. Rahman and Whidborne use measured fuel flow, thrust, compressor pressure ratio, air flow, RPM, and exhaust gas temperature for the Olympus to examine the effect of engine bleed on steady state and transient performance of the engine using MATLAB/Simulink as the modeling tool [35]. They also use representative turbomachinery performance maps for the Olympus in their model.

1.7 Approach

The approach taken to achieve the goals of this thesis is outlined below:

- Identify a commercially available small gas turbine engine suitable for indoor bench-scale testing in the facilities at the University of Maryland (UMD)
- Develop a thermodynamic model of the engine using Numerical Propulsion System Simulation (NPSS)
- Design and construct a test facility for safe indoor testing of the engine
- Measure the engine’s performance parameters – thrust, air flow rate, fuel flow rate, and internal stage temperatures and pressures
- Use the measured performance data to validate the NPSS model of the engine

Chapter 2: Engine Selection

Cost, size, and availability of turbomachinery performance maps were among the considerations for selecting a suitable gas turbine platform for a bench-scale GT/SOFC prototype. A complete list of the considerations/requirements used to identify a gas turbine engine is included below:

- Relatively inexpensive
- Maximum thrust and air flow rate are suitable for the previously designed engine exhaust ejector at UMD [72]
- Compressor and turbine performance maps are available
- Engine can easily be modified for measurements of internal stage temperatures and pressures and the eventual integration of the fuel cell system
- Engine sensor output (RPM, exhaust temperature, etc.) collection is available
- Engine controller can easily be configured for static operation

The candidate gas turbine engine platforms are described in Table 4.

Table 4. Candidate gas turbine platforms.

Engine	**P200-SX Turbine Complete**	**Olympus HP (University Configuration)**	**Titan**	**Mammoth SP Series**	**K-210G**
Manufacturer/ Dealer	JetCat USA [73]	AMT Netherlands [21]	AMT Netherlands [21]	Jet Central USA [74]	KingTech Turbines [75]
Price	$5,495.00	$8,979.20	$11,072.20	$4,795.00	$4,350.00
Max Thrust	231 N	230 N (@ STP and 108,500 RPM)	392 N (@ STP and 96,000 RPM)	225 N	206 N
Weight	25 N	28.5 N	35 N	22 N	16 N
Diameter	12.88 cm	12.95 cm	14.73 cm	12.45 cm	11.25 cm
Length	34.67 cm	37.34 cm	38.35 cm	34.9 cm	28.6 cm
RPM Range	33,000-112,000	112,000 (max)	100,000 (max)	28,000-104,000	33,000-120,000
Max Exhaust Temp.	750 °C	750 °C	875 °C	750 °C	650 °C
Fuel Rate @ Full Power	0.0117 kg/sec	0.0106 kg/sec (@ 230 N)	0.017 kg/sec (@ 392 N)	0.0109 kg/sec	0.0098 kg/sec
Turbine Map Available	No	No	No	No	-----
Compressor Map Available	No	Yes	Yes	No	-----
Sensors	Turbine temp. and RPM, fuel flow (ml/min)	Tt3, Tt4, Tt5, Tt6, Ps3,Pt3, Pt4, Pt5, RPM	RPM, exit temp., others upon request	RPM, exit temp.	-----
Sensor Output Collection Available	Yes (sold separately)	Yes (included with engine)	Yes (included with engine)	Yes (included with engine)	-----
Electronic Controller Available	-Yes (included with engine) -usage notes in manual	-Yes (included with engine) -usage notes in manual -analog throttle available for static testing	-Yes (included with engine) -usage notes in manual -analog throttle available for static testing	-Yes (included with engine) -usage notes in manual	-----

***Note: All engine prices listed are accurate as of April 2015.*

All candidate engines considered produce a maximum thrust of less than 445 N. This is because the current work uses an exhaust ejector system that was designed previously at UMD for testing of a gas turbine engine with a maximum thrust of 467 N [72]. The least expensive engines are JetCat's P200-SX, Jet Central's Mammoth SP Series, and KingTech's K-210G. However, the compressor and turbine performance maps are unavailable for these engines. AMT is willing to provide compressor maps for the Olympus and Titan, but unfortunately they do not generate performance maps for their turbines. The availability of turbomachinery maps greatly assists the modeling effort as producing these maps would require additional experimental data. AMT also offers analog throttle controllers for static ground operation of their engines. In addition, AMT offers factory-installed measurement ports ("University Configuration") for axial stage stagnation temperatures and pressures. This saves the time and risk of tampering with the engine's flow path to make these measurements. Because AMT is capable of making these modifications to their engines, it is likely they could eventually assist with the physical integration of a fuel cell system. After narrowing the engine candidates down to AMT's Olympus and Titan, it was ultimately decided that the Olympus is the best choice for a GT/SOFC prototype due to budget constraints and the availability of other performance data from other universities [29]–[35]. A picture of AMT's Olympus in "University Configuration" is provided in Figure 11.

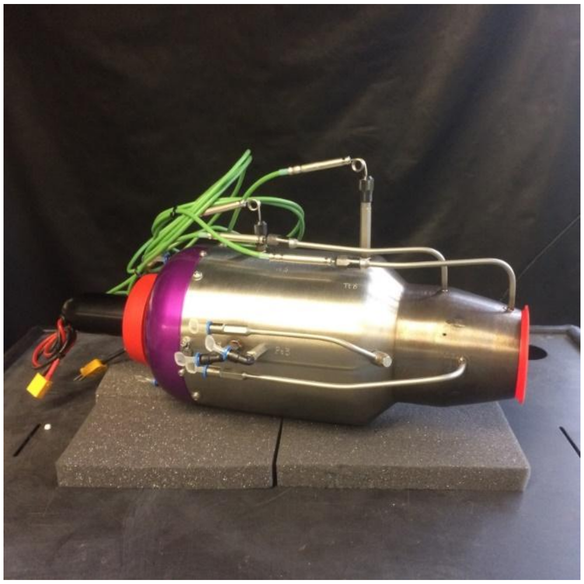

Figure 11. AMT Olympus in University Configuration.

The AMT Olympus is a small turbojet engine that produces a maximum rated thrust of 230 N and has a maximum rated air flow rate of 0.45 kg/sec. It utilizes a centrifugal compressor with a maximum compression ratio of $\pi_c = 3.8$, annular combustor, and an axial turbine. The Olympus is a direct electric start engine that operates on Jet-A fuel. Figure 12 is a cutaway illustration of the Olympus showing its internal stage components and the locations of the temperature and pressure measurement ports [28].

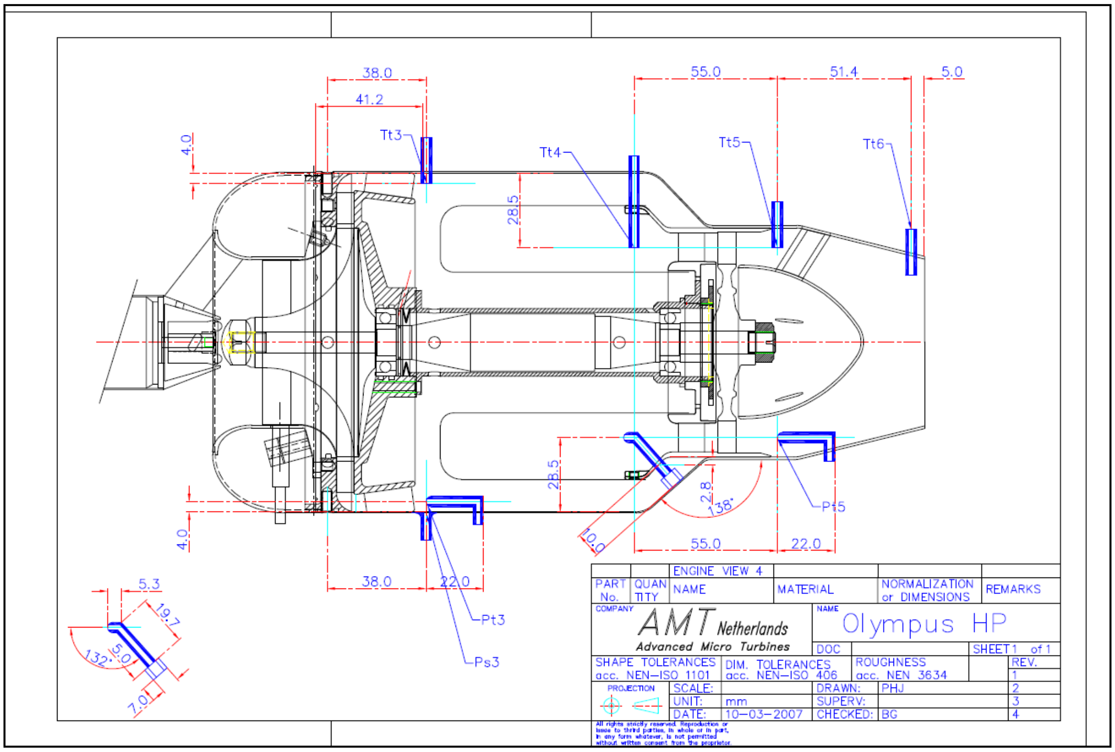

Figure 12. Schematic diagram of the Olympus and its measurement port locations.

Table 5 shows the locations of the various temperature and pressure measurements as a function of position (stage) in the cycle:

Table 5. Locations of the temperature and pressure measurements on the Olympus engine.

Axial Stage	Symbol	Description
3	T_{t3}/T_{03}	Total temperature at compressor exit
4	T_{t4}/T_{04}	Total temperature at turbine inlet
5	T_{t5}/T_{05}	Total temperature at turbine exit
6	T_{t6}/T_{06}	Total temperature at nozzle exit
3	P_{s3}	Static pressure at compressor exit
3	P_{t3}/P_{03}	Total pressure at compressor exit
4	P_{t4}/P_{04}	Total pressure at turbine inlet
5	P_{t5}/P_{05}	Total pressure at turbine exit

Chapter 3: NPSS Engine Model

3.1 Overview of NPSS

The thermodynamic modeling performed in this work is implemented in Numerical Propulsion System Simulation (NPSS) – a modeling environment developed by the National Aeronautics and Space Administration (NASA) [76], [77]. NPSS was designed exclusively for gas turbine analysis and engine models are assembled from a library of standard gas turbine components (compressors, combustors, turbines, etc.) that come with the NPSS package. Each component satisfies the conservation equations for mass and energy. User-defined components can also be developed using the object-oriented NPSS coding language which is similar to C++. NPSS components (called “elements”) contain flow port data structures that save and pass internal flow information (pressure, temperature, enthalpy, entropy, etc.) between connected elements. The NPSS software release also includes several thermodynamic packages, but Chemical Equilibrium with Applications (CEA) is used in this work [78].

CEA performs chemical equilibrium calculations to determine a flow's thermodynamic state. These calculations are based on the minimization of Gibbs' free energy, which produces a solution that is independent of activation energy or reaction kinetics [78]. Although equilibrium calculations are not usually needed to model non-emission related aspects of gas turbine performance, they are required in hybrid GT/SOFC systems because fuel cell models require knowledge of speciation and the bulk heating value of the fuel cell exhaust varies with operating condition. The need to incorporate multi-step equilibrium chemistry is one reason why more computational resources are required to simulate hybrid GT/SOFC systems than stand-alone gas turbines.

NPSS uses a quasi-Newton's method solver to find solutions (operating points) to the set of coupled differential equations that represent the system. The equations are solved by specifying a set of independent variables (called 'independents') and a set of target conditions ('dependents') that are defined using equalities. The solver iteratively adjusts the values of the independents to converge on a solution that satisfies all the dependent conditions. An example of an independent-dependent relationship is adjusting the shaft speed (RPM) such that power input to the compressor equals the power extracted from the turbine. Another example is varying the air mass flow into the engine such that the calculated thrust matches the user-specified thrust. A properly configured solver has an equal number of independents and dependents. A detailed list of the independent variables and dependent conditions used in this work will be presented later.

Solving coupled systems of non-linear differential equations like those representing hybrid GT/SOFC systems is challenging. One challenge associated with Newton-type solvers is coming up with initial 'guesses' for the values of all the independent variables to converge on a viable solution. If the initial guesses for the independents do not produce a physical solution or are not close enough to the converged state, the solver will diverge. As a result, finding the different operating points of a system often requires a trial and error search for an initial state that leads to a physical solution. Once that initial state is located, other states are identified by incrementally adjusting dependent conditions and starting a new iteration using the previous converged state as the initial guess.

Figure 13 [1] is an illustration of an NPSS turbojet model and simple solver configuration.

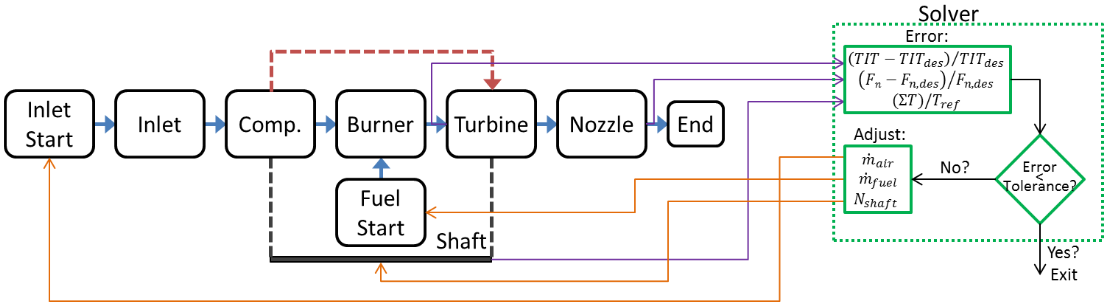

Figure 13. NPSS turbojet model schematic [1]**.**

In Figure 13, Fluid Ports are represented by the blue arrows, and the red arrow represents a Bleed Port. Fluid and Bleed Ports are types of Flow Stations in NPSS that pass flow information between elements (engine components). Examples of information stored by Flow Stations include temperature, pressure, enthalpy, entropy, flow rate, molecular weight, velocity, Mach number, flow area, etc. A Fuel Port is another type of flow station that stores fuel-specific properties such as reference enthalpy, heating value, chemical composition of the fuel, etc. Shaft Ports increase or reduce the energy in the flow by inputting or extracting shaft power from an element. In Figure 13, Fuel Ports are linked between the Fuel Start and Burner elements, and shaft ports are linked between the Compressor and Turbine.

The solver for the turbojet model in Figure 13 consists of three independents (air flow rate, fuel flow rate, and shaft speed) and three dependents (turbine inlet temperature, thrust, and net shaft torque). In this case, design TIT and thrust values are input parameters of the calculation. As the model runs, information about the dependents is sent to the solver. If the calculated dependent errors are within the specified tolerance, the solver terminates and a converged solution has been reached. Otherwise, the solver adjusts the independent variables, returns them to the model, and runs the model again. Further discussions of solver operation and configuration are available elsewhere [76], [77].

Figure 14 shows the assembly of NPSS elements used to model the AMT Olympus turbojet in this work.

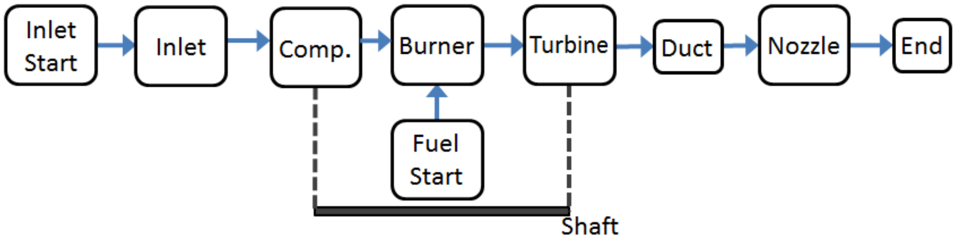

Figure 14. NPSS schematic of AMT Olympus turbojet.

Notice that in Figure 14 there are no bleed port connections as there were in the turbojet model depicted in Figure 13. The following sections describe each component included in the Olympus model. Details about the solver configuration used in this work are discussed in subsequent sections.

3.2 Olympus Engine Model Components

3.2.1 Ambient Element

The Ambient element calculates incoming flight conditions based on user-specified inputs such as flight Mach number, ambient temperature, ambient pressure, etc. For modeling of the static thrust tests of the Olympus, the altitude and flight Mach number are set to zero (for sea-level-static (SLS) operation), and the incoming temperature and pressure are the measured lab temperature and pressure. Calculated flight conditions may include true airspeed, total pressure/temperature, dynamic pressure, etc. The calculated parameters are dependent on the inputs to the element. For example, the incoming stagnation pressure/temperature would be calculated from user-supplied static pressure/temperature and flight speed. This element has no fluid ports and simply stores the calculated flight parameters so that they can be referenced by an Inlet Start element.

Flight conditions at different altitudes are calculated based on standard atmospheric profiles that come with the NPSS package such as ‘Standard’ day [79]. The user must specify which profile to use in a system model. The element requires input of a combination of at least three parameters (in addition to atmospheric profile) to calculate flight conditions.

Input Parameters (used in this work for both on/off design analysis): ‘Standard’ day atmosphere, static temperature, static pressure, and Mach number

Independents/dependents: none

3.2.2 Burner Element

The Burner element calculates performance of a typical gas turbine burner/combustor. This element accepts an air stream from the compressor and a fuel stream from the Fuel Start element (see Figure 15 [1]).

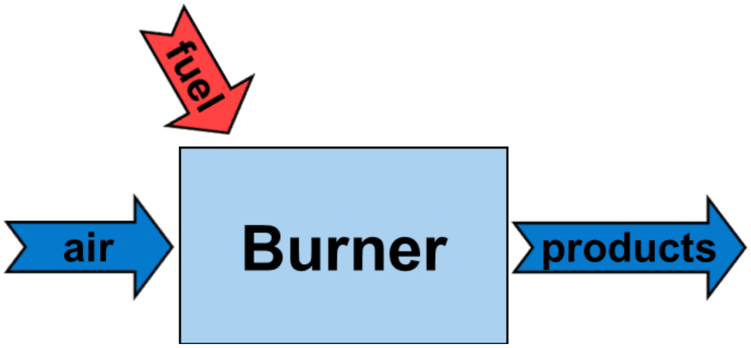

Figure 15. Burner element schematic [1]**.**

Fuel stream properties are defined in the Fuel Start element (described in a later section). A user-specified pressure drop is applied to the burner prior to performing the combustion calculation. In this work, the pressure drop was chosen to match the value measured for the Olympus. The heat release and change in chemical composition associated with combustion are determined using a chemical equilibrium calculation performed by the CEA package. Enabled inputs for this element include: fuel flow rate, fuel-to-air ratio (FAR), burner exit temperature, combustion efficiency, heat loss, and pressure drop due to heat release (Rayleigh flow). The input parameters and independents/dependents used in this work are described below.

Input Parameters (used in this work for both on/off design analysis): fractional pressure drop, fuel flow rate, and combustion efficiency

Independents/dependents: none

3.2.3 Compressor Element

The Compressor element (see Figure 16 [1]) pressurizes incoming airflow according to a user-defined pressure ratio and efficiency. The pressure ratio and efficiency are generally looked up from a tabulated compressor performance map, but they can also be assigned directly in the model. Compressor performance maps give pressure ratio and efficiency as functions of corrected air flow and corrected shaft speed. The compressor map used in this work was provided by AMT for the Olympus engine (see Appendix "A.1 Olympus Compressor Map").

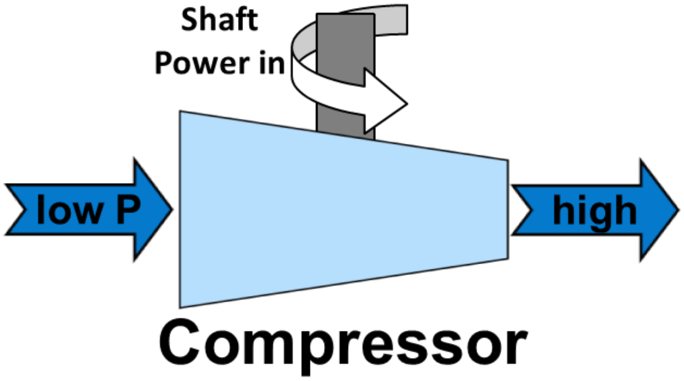

Figure 16. Compressor element schematic [1]**.**

NPSS also requires the definition of an operating line parameter to designate the positions of steady state operating conditions on the performance map. The operating line parameter simply refers to a set of coordinates on the compressor map that define pressure ratio and efficiency as functions of corrected mass flow and shaft speed. Thus, adjusting the operating line parameter implicitly adjusts the pressure ratio and efficiency. When the model is run in 'On-Design' mode, the user must input a design point pressure ratio and design point efficiency. Given these design point parameters, the element scales the input performance map linearly about all three axes to meet the design values. Performance map scaling allows the same map to provide realistic performance predictions for engines of various sizes and operating conditions – one of the tasks that NPSS was designed to perform. When the model is run in 'Off-Design' mode, the performance map is fixed according to the scaling determined in on-design mode, and the compressor operates away from the design point.

To satisfy conservation of mass, the compressor exit air mass flow is set equal to the inlet air mass flow. The exit pressure is calculated based on the compression ratio specified by the user in on-design mode or returned from the performance map in off-design mode.

$$P_{T,out} = P_{T,inlet}\pi_c \tag{20}$$

The exit enthalpy is calculated from the definition of isentropic efficiency [17]:

$$h_{T,out} = \frac{h_s - h_{T,inlet}}{\eta_s} + h_{T,inlet} \tag{21}$$

Power added from the shaft is calculated from the change in enthalpy across the compressor:

$$\dot{W} = \dot{m}\left(h_{T,out} - h_{T,inlet}\right) \tag{22}$$

The input parameters and independents/dependents used in this work are described below.

On-design analysis:

- Input Parameters (used in this work): compressor performance map, pressure ratio, efficiency, operating line parameter, corrected shaft speed

- Independents: none
- Dependents: none

Off-design analysis:

- Input Parameters (used in this work): compressor performance map
- Independents: operating line parameter
- Dependents: corrected mass flow = calculated mass flow from compressor map

3.2.4 Duct Element

The Duct element (see Figure 17 [1]) calculates pressure and heat losses through ducts.

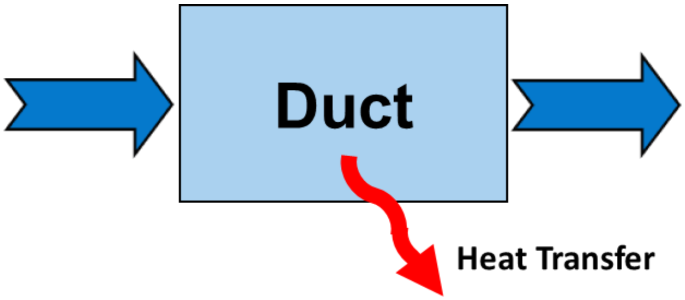

Figure 17. Duct element schematic [1]**.**

Pressure and heat losses are either input as user-defined fractional losses or via user-defined calculation functions (usually by means of a ‘preexecute()’ function). In this work, pressure losses are calculated using a ‘preexecute()’ function. The heat loss through the duct is assumed to be negligible.

Input Parameters (used in this work for both on/off design analysis): ‘preexecute()’ pressure loss function

Independents/dependents: none

3.2.5 Flow End Element

The Flow End element terminates a flow path in the engine model and performs no calculations. The element only has an inlet and no outlet (see Figure 18 [1]).

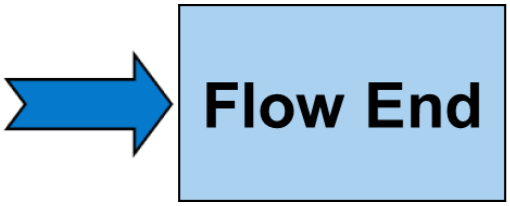

Figure 18. Flow End element schematic [1]**.**

Input Parameters (used in this work for both on/off design analysis): none

Independents/dependents: none

3.2.6 Fuel Start Element

The Fuel Start element (see Figure 19 [1]) generates a fuel stream based on user-defined inputs.

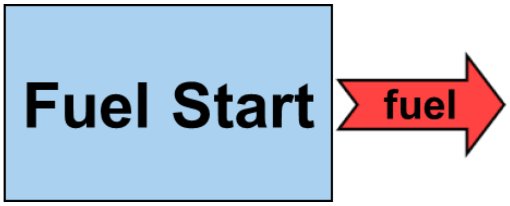

Figure 19. Fuel Start element schematic [1]**.**

The thermodynamics package implemented in the model determines the required inputs. Fuel type and fuel enthalpy at standard conditions are the required inputs for the CEA thermodynamics package. The fuel flow rate can also be defined in this element or the Burner element (as is done in this work).

Input Parameters (used in this work for both on/off design analysis): Jet-A fuel and its enthalpy at standard conditions

Independents/dependents: none

3.2.7 Inlet Element

The Inlet element (see Figure 20 [1]) calculates performance of a typical gas turbine inlet.

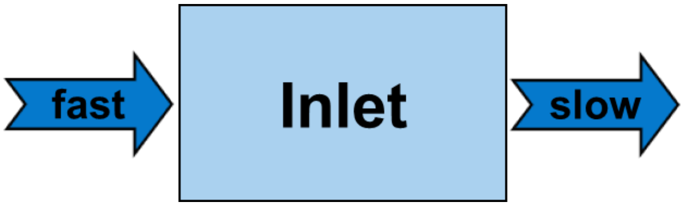

Figure 20. Inlet element schematic [1]**.**

The ram pressure recovery (pressure ratio) is specified by the user as an input value or calculation function. In this work, the ram recovery (π_{inlet}) is defined as an input parameter. It was assumed for this work that pressure losses in the inlet were negligible (π_{inlet} = 1). The inlet exit pressure is calculated based on this value:

$$P_{T,out} = P_{T,free}\pi_{inlet} \tag{23}$$

The ram drag force resulting from decelerating the flow is also output from this element:

$$F_{ram} = \dot{m}_{air}v_{free} \tag{24}$$

Input Parameters (used in this work for both on/off design analysis): ram recovery

Independents/dependents: none

3.2.8 Inlet Start Element

The Inlet Start element (see Figure 21 [1]) creates an air stream to the engine model.

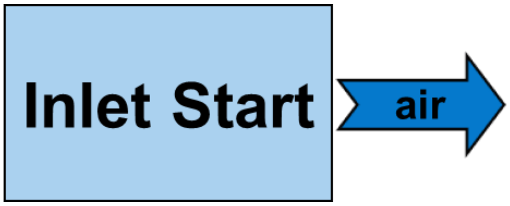

Figure 21. Inlet Start element schematic [1]**.**

Properties of the air stream (such as pressure, temperature, Mach number, dynamic pressure, etc.) are defined/output in the Ambient element and are simply referenced by this element. No calculations are performed in this element.

On-design analysis:

- Input Parameters (used in this work): Ambient element's name; air flow rate (for second design case only)
- Independents: air flow rate (for first design case only)
- Dependents: none

Off-design analysis:

- Input Parameters (used in this work): Ambient element's name
- Independents: air flow rate
- Dependents: none

3.2.9 Nozzle Element

The Nozzle element (see Figure 22 [1]) calculates the performance of the gas turbine's nozzle.

Figure 22. Nozzle element schematic [1]**.**

This element determines performance characteristics for different nozzle geometries (convergent, convergent-divergent, fixed, or variable geometry). In on-design mode, if the nozzle is not choked ($P_{input,exit}$ < $P_{calc,exit}$), the nozzle exit area is calculated such that the calculated exhaust static pressure ($P_{calc,exit}$) equals the specified exhaust static pressure ($P_{input,exit}$). In this case, NPSS iterates Mach number to match pressure using the 'setStaticPs' function. Stagnation exit pressure is then determined from the exit static pressure and exit Mach number. If $P_{input,exit}$ > $P_{calc,exit}$ (choked flow), the exit area is calculated by setting the exit Mach number equal to one. Static exit pressure is then determined using the 'setTotal_hP' function, which iteratively calculates static pressure from the flow enthalpy, total exit pressure, and Mach number. The nozzle is assumed to be adiabatic, so the exit stagnation temperature is equal to the inlet stagnation temperature. In off-design mode, the nozzle exit area is fixed from running the model in on-design mode. The exit Mach number and pressure are then calculated as a function of that flow area and mass flow. Again, the nozzle is assumed to be adiabatic.

For the second design case, mass flow rate into the nozzle is fixed based on the specified air flow rate (determined from the first design case) and fuel flow rate into the engine. For the first design case and all off-design cases, mass flow rate into the nozzle must be adjusted by the system level solver. For this work, this is accomplished by changing the air flow rate into the entire engine (via the Inlet Start element). For both on-design and off-design mode, the gross thrust produced by the engine is calculated from:

$$F_{gross} = \dot{m}_{exit} v_{exit} C_{noz} + (P_{exit} - P_{amb}) A_{exh} \tag{25}$$

Note in Eq. (25) that the freestream velocity term ($\dot{m}_{air} v_{free}$) is neglected because the Olympus engine is tested under static conditions. The nozzle coefficient, C_{noz}, is the ratio of the actual force produced divided by the theoretical force associated with the momentum change. In this work, the default NPSS value of C_{noz} = 1 is used for all model runs.

On-design analysis:

- Input Parameters (used in this work):
    - First design case: none
    - Second design case: exhaust static pressure
- Independents:
    - First design case: exhaust static pressure
    - Second design case: none
- Dependents:
    - First design case: physical exit area = calculated exit area; measured thrust = calculated thrust
    - Second design case: none

Off-design analysis:

- Input Parameters (used in this work): none
- Independents: exhaust static pressure
- Dependents: physical exit area = calculated choked flow exit area; measured thrust = calculated thrust

3.2.10 Shaft Element

The Shaft element performs (see Figure 23 [1]) work/power matching between the compressor and turbine components of the gas turbine model.

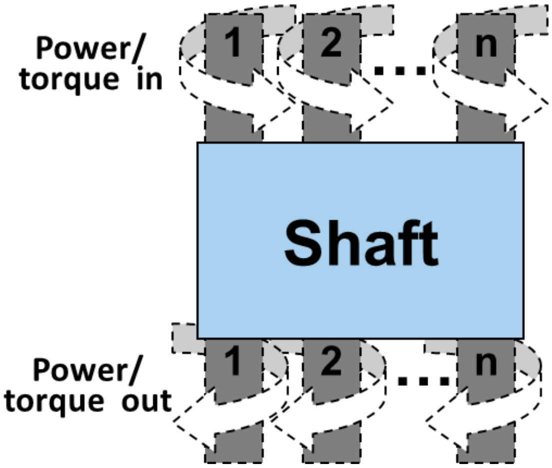

Figure 23. Shaft element schematic [1]**.**

Multiple torque producing components (compressors, turbines, etc.) can be linked to a single shaft element. In this work, a single compressor and turbine element are linked to the shaft. The input ports to the shaft must be declared by the user.

On-design analysis:

- Input Parameters (used in this work): shaft input ports and shaft speed
- Independents: none
- Dependents: zero net torque on the shaft

Off-design analysis:

- Input Parameters (used in this work): shaft input ports
- Independents: shaft speed
- Dependents: zero net torque on the shaft

3.2.11 Turbine Element

The Turbine element (see Figure 24 [1]) expands and extracts work from the core flow of the gas turbine.

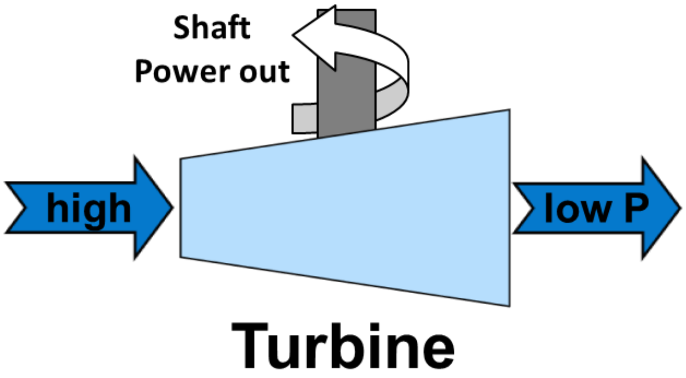

Figure 24. Turbine element schematic [1]**.**

As with the Compressor element, the pressure ratio and efficiency for the turbine are either looked up in a tabulated turbine performance map or assigned directly by the user. The turbine performance map used in this work is a scaled version of a low pressure turbine map developed by General Electric in the 1980s as part of the NASA Energy Efficient Engine (E^3) engine program [80], [81] (see Appendix "A.2 Low Pressure Turbine Map"). Similar to the compressor, a turbine map parameter (pressure ratio in this case) is defined to designate positions of steady state operating conditions on the performance map as functions of corrected air flow rate and corrected shaft speed. Varying the turbine map parameter implicitly varies the efficiency. In on-design mode, NPSS scales the performance map linearly according to a user-specified design point efficiency. During off-design mode, the turbine map is fixed based on the scaling performed in on-design mode, and the turbine operates away from the design point.

To satisfy mass conservation, the inlet mass flow (the sum of the air and fuel mass flows) is set equal to the outlet mass flow. The turbine exit pressure is calculated based on the pressure ratio returned from the performance map or user-defined input:

$$P_{T,out} = P_{T,inlet}/\pi_t \tag{26}$$

The exit enthalpy is calculated from the value of the isentropic efficiency corresponding to the operating point in the turbine operating map and the definition of isentropic efficiency [17]:

$$h_{T,out} = h_{T,inlet} - \left(h_s - h_{T,inlet}\right)\eta_s \tag{27}$$

Power extracted from the flow is determined from the change in enthalpy:

$$\dot{W} = \dot{m}\left(h_{T,inlet} - h_{T,out}\right) \tag{28}$$

The input parameters and independents/dependents used in this work are described below.

On-design analysis:

- Input Parameters (used in this work):
    - First design case: pressure ratio
    - Second design case: turbine performance map, efficiency, and corrected shaft speed
- Independents:
    - First design case: efficiency
    - Second design case: pressure ratio (turbine map parameter)
- Dependents: none

Off-design analysis:

- Input Parameters (used in this work): turbine performance map
- Independents: pressure ratio (turbine map parameter)
- Dependents: corrected mass flow = calculated mass flow from turbine map

3.3 Solution Method

3.3.1 Numerical Solver

Thermodynamic models of gas turbine systems are described by highly complex and nonlinear systems of differential equations. Explicit solutions to these equations are generally impossible to develop. Therefore, iterative methods are often employed that begin with an initial approximation of the solution that is refined in subsequent iterations until a feasible solution is found.

The NPSS solver uses a modified Newton's method [82] with Broyden updates [82]–[84]. The first step of the iteration uses a finite-difference approach to generate a Jacobian (a partial derivative matrix). Subsequent iterations use Broyden's method to update the Jacobian matrix in lieu of finite differencing. This improves computational speed. More information about Newton's and Broyden's method can be found in References [82]–[84].

As mentioned previously, the NPSS solver is configured with a set of independents and dependents. The independents are varied by the solver to converge on a solution that satisfies the dependent conditions. Perturbations to the independents form the Jacobian matrix describing the correlations between all of the independents and dependents in the model. During each iteration, NPSS calculates corrections to the independents based on the current Jacobian and errors in the dependents returned to the solver. New Jacobians are only generated after the first iteration according to specific convergence criteria [76]. The user can specify the maximum number of iterations and Jacobians for the solver to produce before the solver terminates and convergence is not achieved.

3.3.2 Independents and Dependents

This section describes the NPSS solver configurations (independents and dependents) used in the model of the Olympus turbojet. Two on-design cases are run before running several off-design cases. A description of design versus off-design analysis is provided later in Section “3.4 Cycle Analysis”. It is important to note here that the current NPSS model is based on engine performance data without air flow rate measurements. The method used to measure air flow rate in this work significantly reduces freestream pressure and results in non-physical thrust measurements. A more detailed discussion of the pressure losses through the air flow measurement apparatus and its effect on thrust measurements will be presented in Section “4.2 Challenges”.

As mentioned previously, AMT provided the compressor performance map for the Olympus but they could not provide the turbine performance map. This presents the difficulty of not knowing how the turbine’s pressure ratio and efficiency change as a function of corrected shaft speed and corrected mass flow rate. As a result, the approach taken involved scaling a General Electric’s low pressure turbine map from NASA’s E^3 program [81] (provided with the NPSS software release [76]).

However, scaling the map requires knowledge of the turbine design point efficiency. This is estimated by first running the NPSS model without a turbine map and varying the turbine efficiency, air flow rate, and nozzle exhaust static pressure to satisfy the full throttle operation design conditions (defined in Section “3.4 Cycle Analysis”). Table 6 lists the NPSS solver independents and dependents for the first design case.

Table 6. Independents and dependents for the design case without a turbine map.

Independents	
Variable Name	*Description*
AirControl	air mass flow rate
TurbEff	turbine efficiency
ExhPress	exhaust static pressure
Dependents	
Variable Name	*Description*
ShH.integrate_Nmech	zero net torque on the shaft
Thrust	specified net engine thrust = calculated thrust
NozArea	specified nozzle exit area = calculated nozzle exit area

The second design case runs the model again but with the low pressure turbine map using input values of turbine efficiency (now the design value), air flow rate, and exhaust static pressure from the converged solution in the first design case. Table 7 lists the independents and dependents for the second design case.

Table 7. Independents and dependents for the design case with the low pressure turbine map.

Independents	
Variable Name	*Description*
TurbH.S_map.ind_parmMap	turbine map pressure ratio
Dependents	
Variable Name	*Description*
ShH.integrate_Nmech	zero net torque on the shaft

Although the solver configuration is different between the first and second design cases, it is important to note that the converged solutions are the same. The input parameters for both design cases are defined in the following section. Recall that the current model is based on performance data without air flow measurements; otherwise, air flow rate would be an input to the model instead of being varied by the solver as an independent.

In this work, off-design cases are run to predict engine performance at different throttle settings (specified by the user as percentages of the full throttle design condition thrust). As with the second design case, off-design cases are run using the low pressure turbine map to predict turbine performance. Table 8 shows the NPSS solver configuration for the off-design cases.

Table 8. Independents and dependents for off-design cases.

Independents	
Variable Name	*Description*
InletStart.ind_W (same as AirControl)	air mass flow rate
CmpH.S_map.ind_RlineMap	compressor map operating line parameter
TrbH.S_map.ind_parmMap	turbine map pressure ratio
ShH.ind_Nmech	shaft speed (RPM)
ExhPress	exhaust static pressure
Dependents	
Variable Name	*Description*
CmpH.S_map.dep_errWc	corrected mass flow = calculated mass flow from compressor map
TrbH.S_map.dep_errWp	corrected mass flow = calculated mass flow from turbine map
NozPri.dep_Area	physical exit area = calculated choked flow exit area
ShH.integrate_Nmech	zero net torque on the shaft
Thrust	specified net engine thrust = calculated thrust

The NPSS solver is generally defined using the ‘autoSolver Setup()’ command, which automatically adds independents and dependents to the solver based on the components included in the gas turbine model. Newly user-defined or existing independents and dependents can be added or removed from the solver at the user’s discretion after calling the ‘autoSolverSetup()’ command. For the design cases in this work, this command only adds the ‘TrbH.S_map.ind_parmMap’ independent and

‘ShH.integrate_Nmech’ dependent to the solver. The other independents/dependents listed in Table 6 are newly defined. For the off-design cases in this work, the ‘autoSolverSetup()’ command adds all of the independents/dependents described in Table 8 to the solver except for the ‘ExhPress’ independent and ‘Thrust’ dependent. One of the challenges associated with NPSS solver setup is ensuring that there are equal numbers of independents and dependents. In many instances, the user will need to provide additional independents/dependents to satisfy this requirement. The difficulty becomes defining independents/dependents that have physical significance to the engine model and ensuring that all the dependents are affected by at least one of the independents.

3.4 Cycle Analysis

Cycle analysis in NPSS is generally performed in two stages: a design case (design analysis/on-design mode) followed by one or more off-design cases (off-design analysis/off-design mode). The design case determines all geometric/sizing parameters (such as the nozzle throat/exit area) and turbomachinery performance map scale factors based on the specified design parameters. The design case establishes the baseline engine model and serves as a reference condition for off-design analysis. In this work, the only geometric parameter calculated during a design case is the nozzle exit area. The solver dependent ‘NozArea’ in the first design case ensures that the calculated nozzle exit area equals the physical engine’s nozzle exit area of 33.23 cm^2. This nozzle exit area remains fixed for the second design case and all off-design cases.

Generally, only one design case is required for each model run. The reasons for executing two design cases in this work were discussed above in Section "3.3.2 Independents and Dependents". The input design case parameters for the Olympus are shown in Table 9.

Table 9. Full throttle design case parameters for the Olympus engine model.

Parameter	Value
Ambient Pressure (kPa)	101.97
Ambient Temperature (K)	296.53
Shaft Speed (RPM)	108,500
Thrust (N)	210.8
Mach Number	0
Ram Pressure Recovery	1.0
Compressor Total Pressure Ratio (P_{03}/P_{02})	3.78
Compressor Efficiency	0.72
Fuel Type	Jet A
Fuel Enthalpy (kJ/kg)	-1813.3
Fuel Flow Rate (kg/sec)	0.0112
Burner Pressure Loss	4.83%
Burner Efficiency	0.95
Turbine Total Pressure Ratio (P_{04}/P_{05})	2.26
Nozzle Exit Area (cm^2)	33.23

The design case parameters are defined for full throttle operation. The input values of ambient pressure, ambient temperature, engine speed, thrust, Mach number, compressor pressure ratio, fuel flow rate, burner pressure loss, and turbine pressure ratio are determined experimentally from full throttle operation of the Olympus. Compressor efficiency is estimated from the compressor performance map provided by AMT. The fuel enthalpy was calculated for liquid Jet-A from thermodynamic data available with the NPSS software package [76]. Also, the parameters defined in Table 9 are specifically for the first design case mentioned in Section "3.3.2 Independents and Dependents". The input values of turbine efficiency, air flow rate, and exhaust static pressure for the second design case are determined from the converged solution of first design case. All other input parameters for the second design case are the same as those listed in Table 9.

During off-design cases, NPSS calculates operating characteristics for conditions other than those defined in the design case. For example, the user can specify different ambient conditions, flight Mach number, throttle settings, etc. In this work, the performance of the Olympus engine is predicted for various throttle settings. Input parameters for off-design analysis are percent throttle, ambient pressure, ambient temperature, fuel flow rate, and burner pressure drop. It is important to note that the engine model is fixed for the off-design analysis according to the converged solution of the design analysis. This means performance is calculated using the same turbomachinery performance maps and geometric engine parameters for each case. If several cases were run in on-design mode to meet each measured operating point for the Olympus, then each case would result in a completely different engine. This is because NPSS scales the compressor/turbine maps and calculates the nozzle exit area differently for each operating point when run in on-design mode. For this reason, gas turbine models in NPSS are usually run with a design case followed by multiple off-design cases (as is done in this work).

Chapter 4: Engine Performance Measurements

4.1 Test Facility Design

An experimental facility was designed to safely operate the engine while collecting the data needed to validate the thermodynamic model. These data include: thrust, air flow rate, fuel flow rate, shaft speed (RPM), and the pressures/temperatures indicated in Table 5. A CAD rendering of the test facility is provided in Figure 25 and photos of the facility are shown in Figure 26.

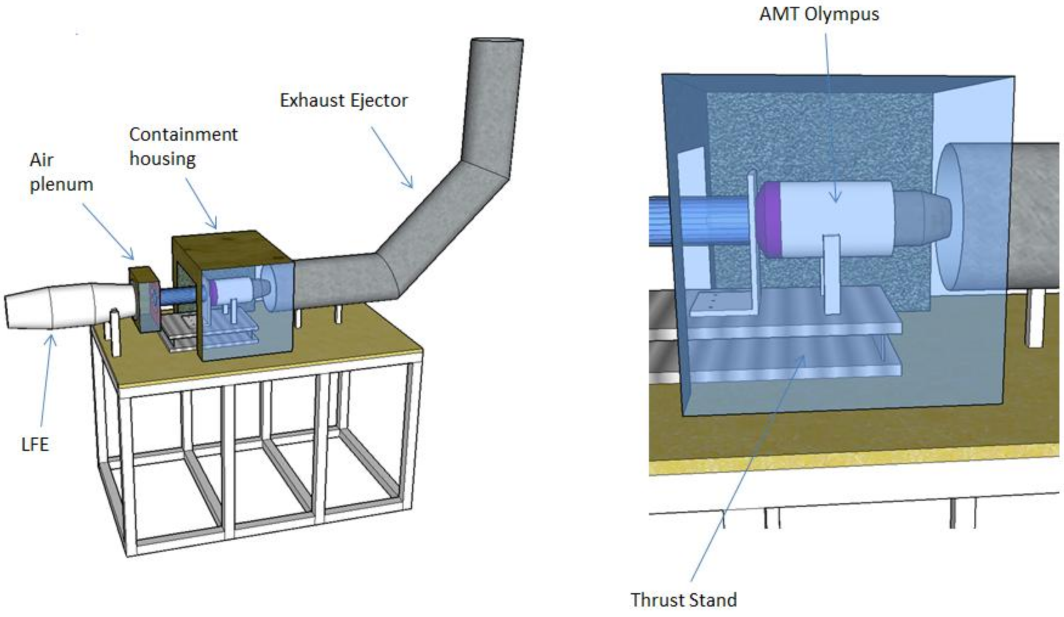

Figure 25. CAD depiction of engine test facility.

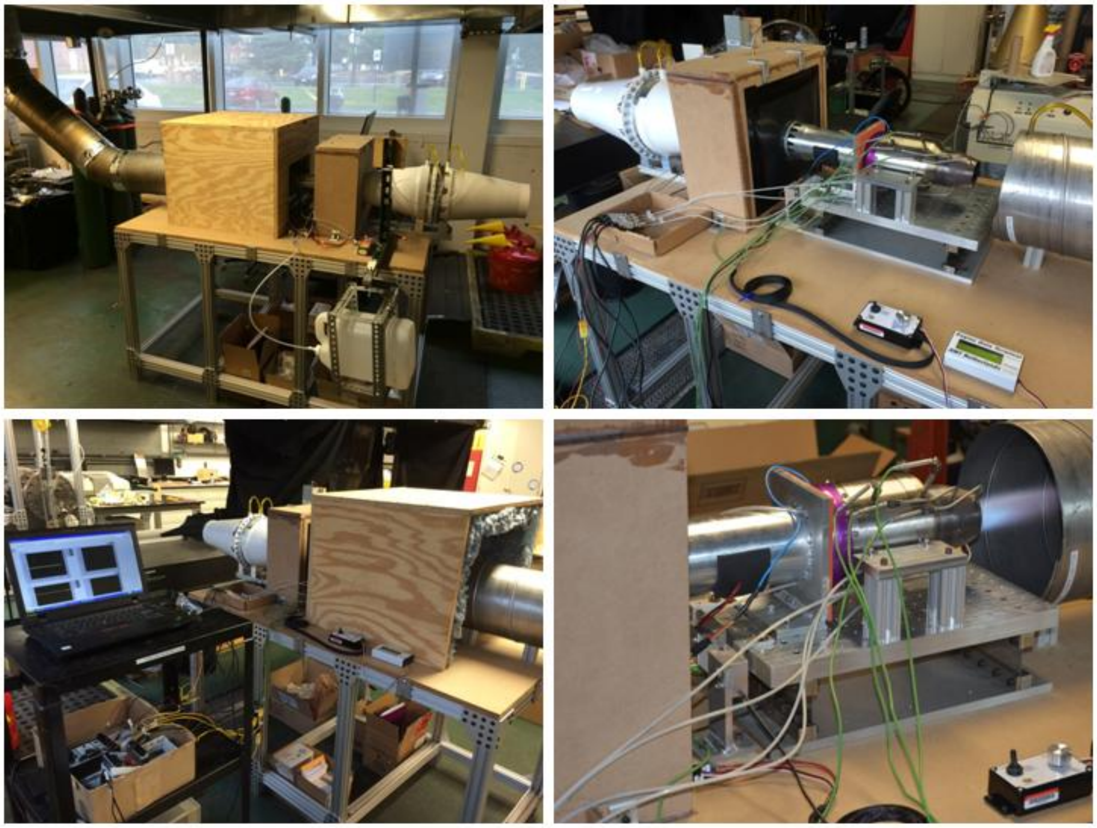

Figure 26. Engine test facility.

The engine sits in a containment housing that protects the laboratory and its occupants from debris in case of catastrophic failure. The housing was designed with dimensions large enough to allow modifications to the engine for eventual fuel cell integration. Fireproof denim insulation covers the interior walls of the housing to reduce engine noise for indoor operation. The engine rests on a thrust stand that measures force along the same axis as incoming airflow. The thrust stand consists of a horizontal aluminum plate supported by thin metal flexures and is restrained by a load cell. More details about the design of the thrust stand can be found in [85]. An aluminum duct connects the engine inlet to the air plenum, and the duct is connected to the air plenum using a compliant rubber gasket material. An ejector nozzle cools the engine's exhaust prior to entering the laboratory's exhaust hood by mixing it with room temperature air.

4.2 Challenges

The most challenging aspect of the test facility design is ensuring the air flow rate measurement does not disrupt the thrust measurement. An accurate air flow rate measurement requires all incoming air to flow through the laminar flow element (LFE). This necessitates creating an air tight seal between the LFE exit and engine inlet that is still flexible enough to transmit thrust. This proved to be difficult because the inlet cowl of the Olympus contains several essential connection and electronic ports (for fuel lines, RPM sensor, electric starter, etc.). Ultimately, this was accomplished by attaching the downstream end of the laminar flow element to a small plenum and connecting the engine to the other side of the plenum using a custom inlet extension that attaches to a flexible rubber diaphragm as illustrated in Figure 27.

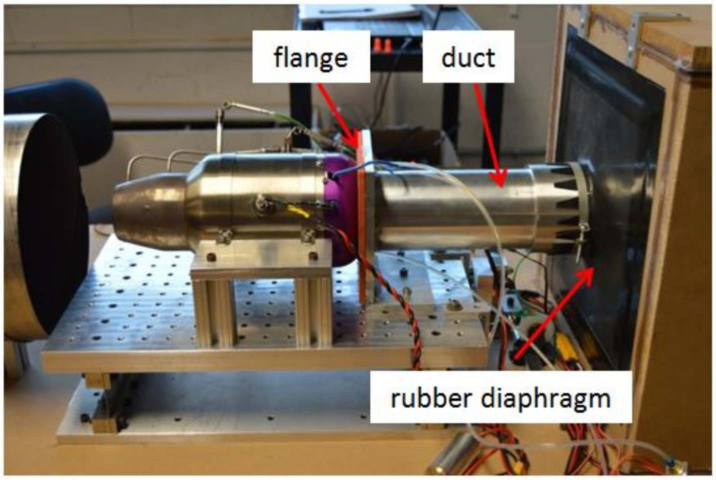

Figure 27. Custom inlet extension.

The rubber diaphragm is intended to allow the thrust stand to deflect as load is applied. The inlet extension contains two feed-through holes for the fuel lines and a single feed-through hole for the electric starter connection. High temperature insulation foam compressed between the extension flange and the engine inlet ensures an air tight connection between the engine and inlet extension.

Another challenge is that the additional components required for air flow rate measurement (LFE, air plenum, duct, etc.) obstruct the flow leading to nearly 10% loss of free-stream pressure at the engine inlet. Location of the engine inlet pressure measurement is shown in Figure 28.

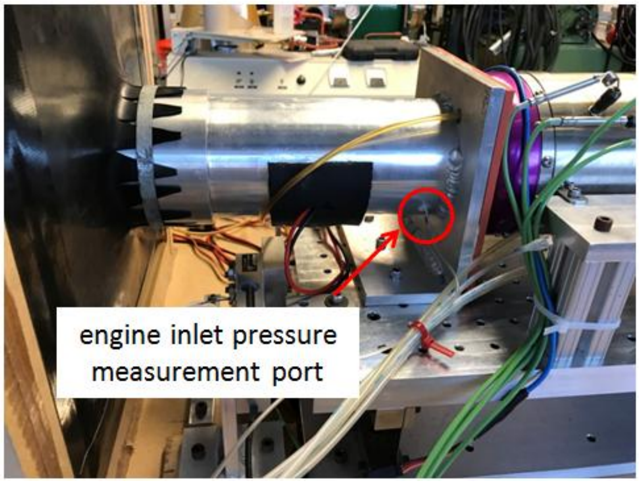

Figure 28. Engine inlet pressure measurement location.

Figure 29 shows the difference in pressure between the room and the engine inlet plane at various engine speeds.

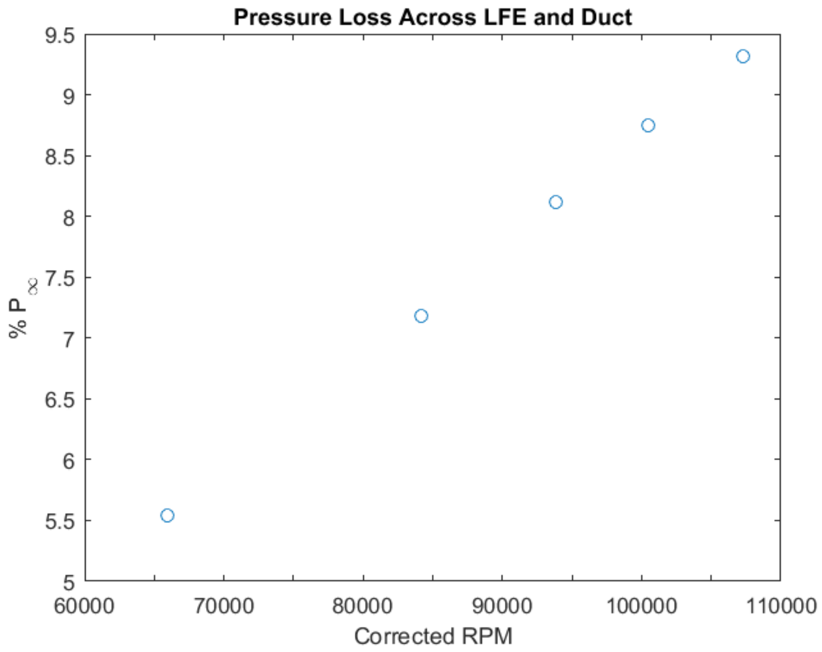

Figure 29. Pressure drop across LFE-plenum-duct as a function of engine speed.

Figure 29 shows the pressure drop through the LFE-plenum-duct is quite large (~9.4% P_∞ at full throttle). Most of this pressure loss occurs in the plenum and duct as the pressure drop across the LFE is relatively small (~1.5% at full throttle) (see Figure 30).

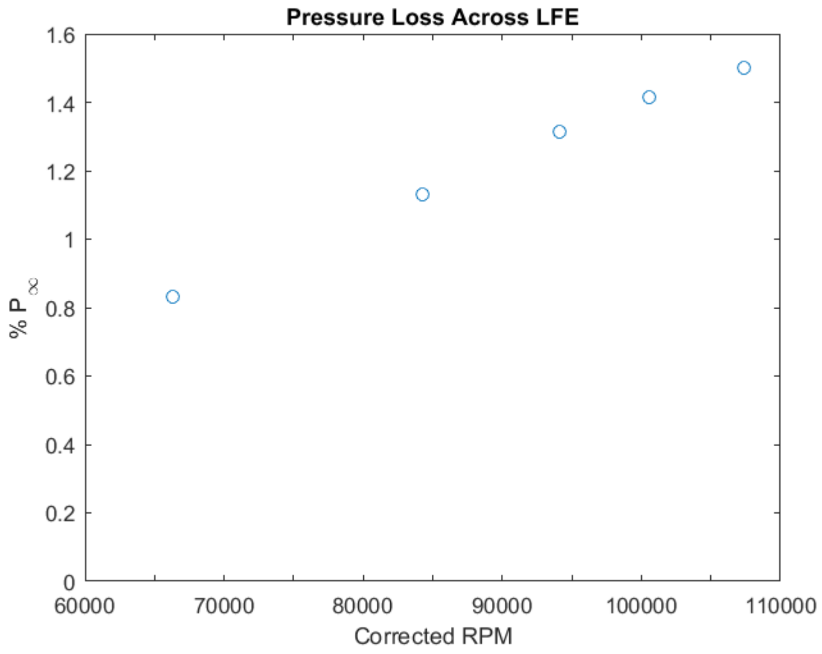

Figure 30. Pressure drop across the LFE as a function of engine speed.

Despite these pressure losses, measured thrust is consistently greater at each engine speed than measured thrust without the obstructive air flow measurement apparatus (see Section “5.2.4 Thrust with & without Air Flow Rate Measurement”).

Another complication with the test facility design is thrust stand calibration. It was observed that the calibration curves for the thrust stand change over the course of an engine throttle sweep (see Figure 31). In Figure 31, the colored lines represent the calibration curves for different speeds during a throttle sweep. The term ‘throttle sweep’ simply refers to a set of engine runs between 20% and 100% throttle.

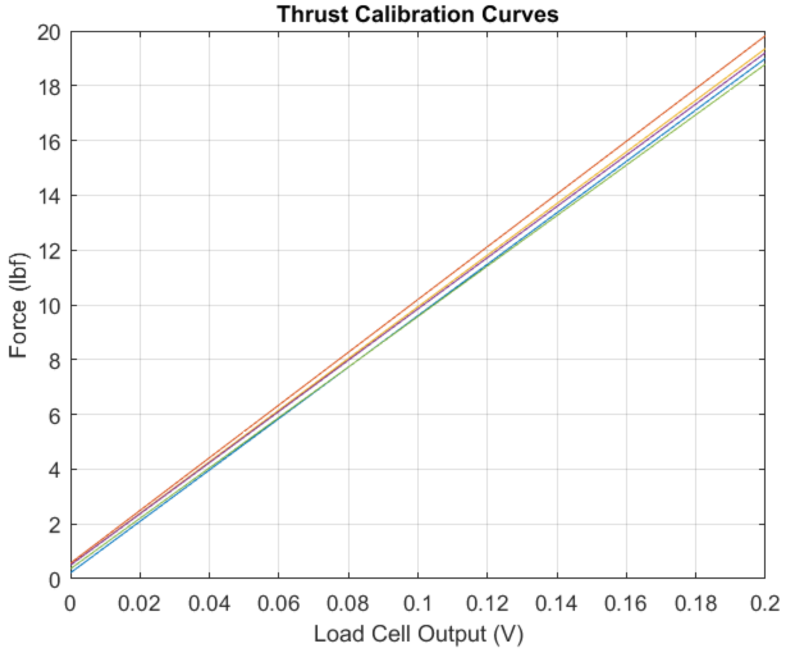

Figure 31. Thrust calibration curves for different engine speeds during a throttle sweep.

The thrust stand and load cell used to measure thrust are bolted to a medium-density fiberboard (MDF) tabletop which has some minor elasticity. During an engine test, vibration of the table and deflection of the thrust stand likely loosen these attachment joints such that the load cell does not maintain consistent contact with the thrust stand between runs. As a result, the thrust stand needs to be calibrated before each engine run. The procedure for calibrating the thrust stand is described in Section “4.3.1 Thrust”.

The strength of the laboratory’s exhaust system is also an issue during engine operation. The laboratory contains four individual exhaust hoods, but the exhaust ejector is only connected to one of those. It was determined previously that a single exhaust hood at maximum power can sufficiently engulf the exhaust from an engine larger than the Olympus [72]. However, the fume hood’s control system uses dampers in the laboratory’s exhaust duct to maintain a constant differential pressure between the duct and the lab which prevents the exhaust hoods from operating at maximum power. At engine speeds upwards of about 40% throttle, the fume hood cannot keep up with the exhaust expelled from the engine. All four hoods must be powered on between runs at these higher speeds and allowed to run for approximately 10-15 minutes to remove residual engine exhaust from the lab. Failure of the exhaust ejector to keep up with the engine's exhaust during runs presumably results in backpressure which could have adverse effects on thrust.

4.3 Measured Quantities

4.3.1 Thrust

Engine thrust is measured using a Transducer Techniques ESP-35 load cell with a maximum capacity of 77 lbf (343 N). The ESP-35 is a cantilever beam load cell with an accuracy of +/- 1.0% of the load cell reading. The contact point between the load cell and the top horizontal plate of the thrust stand is a single hex bolt (see Figure 32). Prior to each engine run, the hex bolt was tightened against the top plate of the thrust stand with about 3 lbf (13.3 N) of preload tension measured on the load cell to ensure secure contact between the load cell and thrust stand. Output from the ESP-35 is filtered using a Transducer Techniques TMO-2-160 load cell conditioner.

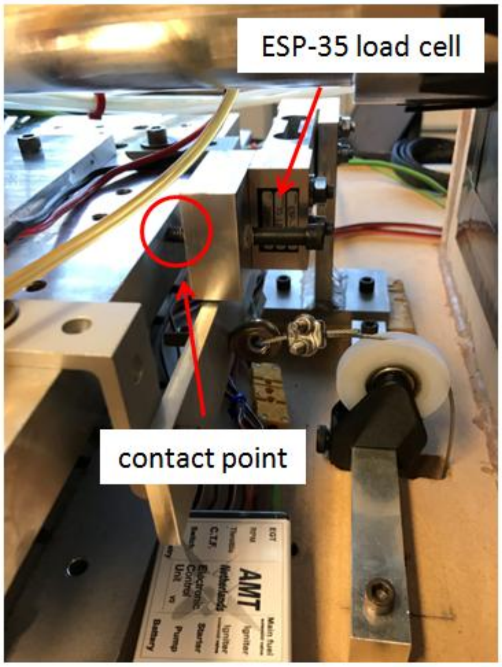

Figure 32. Thrust stand load cell configuration.

Although the load cell itself was calibrated by the manufacturer, some accounting is needed for the stiffness of the thrust stand flexures and LFE-to-engine connection. As a result, the thrust measurement system must be calibrated to account for the effective spring constant produced by these added components. The thrust stand is calibrated using a cable/pulley system where weights are hung at the end of the cable (see Figure 33).

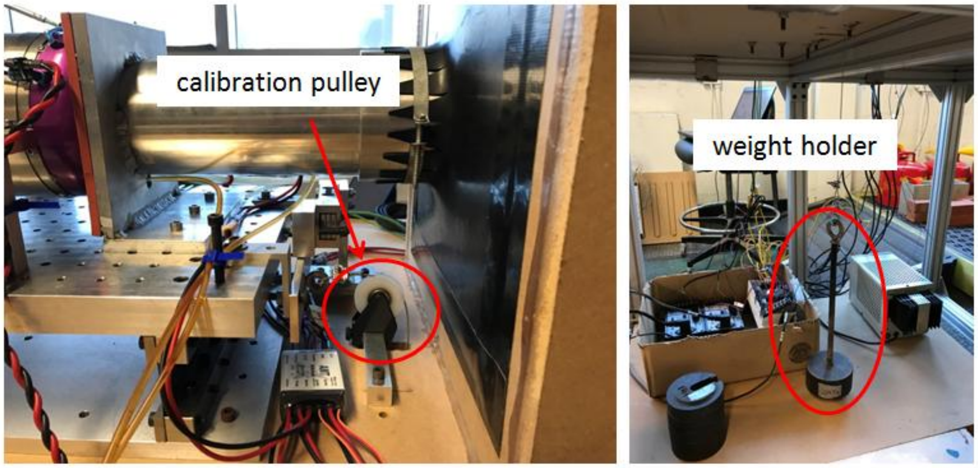

Figure 33. Calibration pulley system.

A calibration curve relating thrust produced by the engine as a function of load cell voltage output must be produced at the beginning of each testing session due to the elasticity of the MDF tabletop. The procedure for generating a calibration curve for the thrust measurement system is outlined below:

1. Remove all weights from the cable/pulley system, and zero the load cell output using the “Balance” knob on the TMO-2-160 load cell signal conditioner.
2. Hang different (known) weights from the end of the loading cable, and record both the total force exerted on the thrust stand and voltage output from the load cell.
3. Incrementally unload pulley system, and record the net force on the thrust stand and load cell voltage output for each weight removed.
4. Repeat steps 2-3 about two or three times.
5. Plot force as a function of load cell voltage output, and generate a linear regression curve. A typical calibration plot is shown in Figure 34.

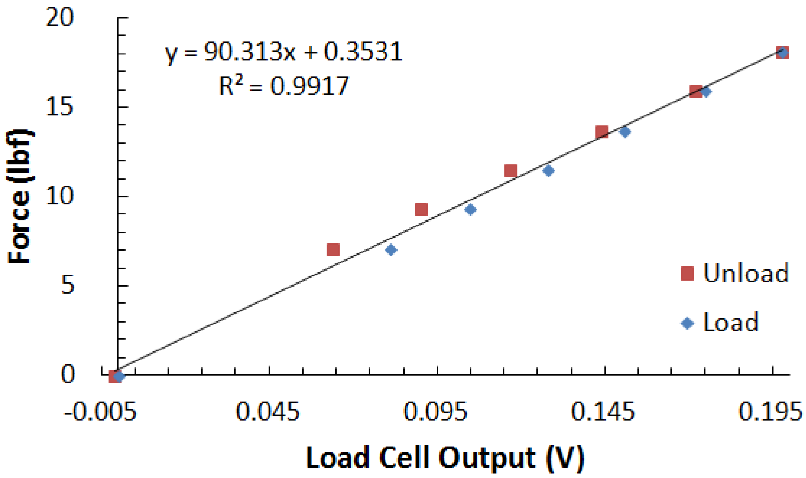

Figure 34. Example thrust stand calibration curve.

To produce the plot in Figure 34, known weights were loaded and unloaded onto the pulley system. The calibration data show there is some hysteresis in the thrust measurement system which is why the thrust stand needs to be calibrated before each engine run.

4.3.2 Air Flow Rate

The Olympus engine draws air through a Meriam Z50MC2-6 LFE. The maximum flow rate of the Z50MC2-6 is 1000 SCFM (33.9 kg/min) and corresponds to a pressure drop of 8 in H_2O (203.2 mm H_2O). The instrument's accuracy is +/- 0.72% to +/- 0.86% of the measured value. A manufacturer-provided calibration curve is used with the measured pressure drop across the laminar flow element to calculate air mass flow rate.

The volumetric flow rate is calculated using the quadratic calibration curve provided by the manufacturer:

$$\dot{V} = (B \times \Delta P + C \times (\Delta P)^2)\left(\mu_{std}/\mu_f\right) \tag{29}$$

where B and C are calibration coefficients provided by Meriam (see Table 10), ΔP is the measured differential pressure across the LFE, μ_f is the viscosity of air at the incoming flow temperature, and μ_{std} is the viscosity of air at 70°F (21.1°C) (in micropoise).

Table 10. Calibration coefficients for LFE.

Coefficient	Value
B	1.1997661e2
C	-6.0838751e-1

The pressure drop across the laminar flow element (ΔP) is measured using an Omega PX277-30D5V differential pressure transducer with a full-scale range of 30 in H_2O (762 mm H_2O). Multiplying the volumetric flow rate by the ratios of temperature and pressure to standard temperature and pressure gives the volumetric flow rate at standard conditions:

$$\dot{V}_{std} = (B \times \Delta P + C \times (\Delta P)^2)(\mu_{std}/\mu_f)(T_{std}/T_f)((P_{atm} + \Delta P)/P_{std}) \tag{30}$$

where T_{std} is the standard temperature of 70°F (21.1°C), T_f is the incoming flow temperature, P_{atm} is the ambient (room) pressure, and P_{std} is the standard pressure of 29.92 in Hg (759.97 mm Hg). Ambient pressure was recorded from the National Weather Service's website [86] for College Park Airport at the time of testing. Finally, the air mass flow rate is determined by multiplying the standard volumetric flow rate by the density of air at standard conditions, ρ_{std}:

$$\dot{m}_{air} = (B \times \Delta P + C \times (\Delta P)^2)(\mu_{std}/\mu_f)(T_{std}/T_f)((P_{atm} + \Delta P)/P_{std})\rho_{std} \tag{31}$$

4.3.3 Fuel Flow Rate

A gravimetric system is used to measure the fuel flow rate (see Figure 35). The fuel tank is suspended from a Transducer Techniques ESP-20 cantilever beam load cell with a maximum load capacity of 44 lbf (196 N) and an accuracy of +/- 1.0% as illustrated in Figure 35. Like the thrust stand load cell, output from the ESP-20 is filtered using a Transducer Techniques TMO-2-160 signal conditioner. At the beginning of each testing session, the load cell is zeroed (with the unistrut cage and fuel tank attached) in the same manner as the thrust stand load cell.

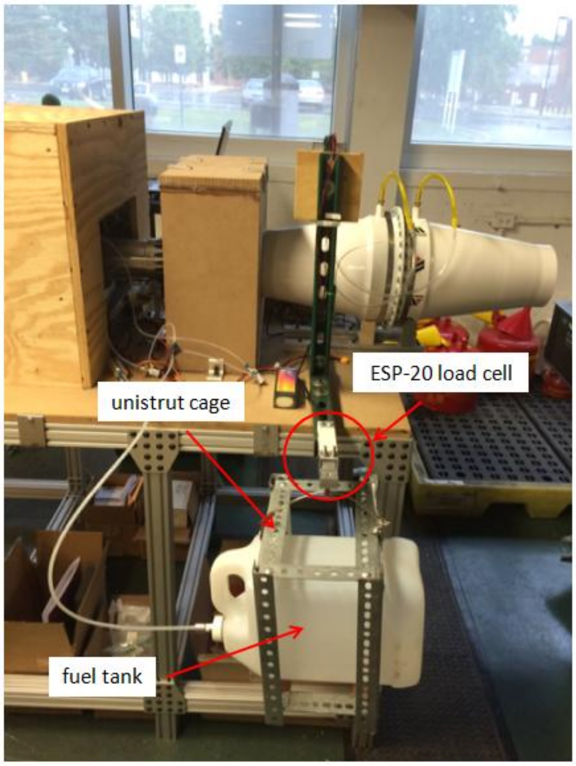

Figure 35. Gravimetric fuel weight measurement system.

During engine runs, the weight of the fuel is logged as a function of time. After the experiment is over, a linear regression curve is fit to the results. The slope of the curve is the equivalent fuel flow rate. An example of fuel weight plotted versus time and its corresponding linear regression curve for an engine test at 80% throttle is shown in Figure 36.

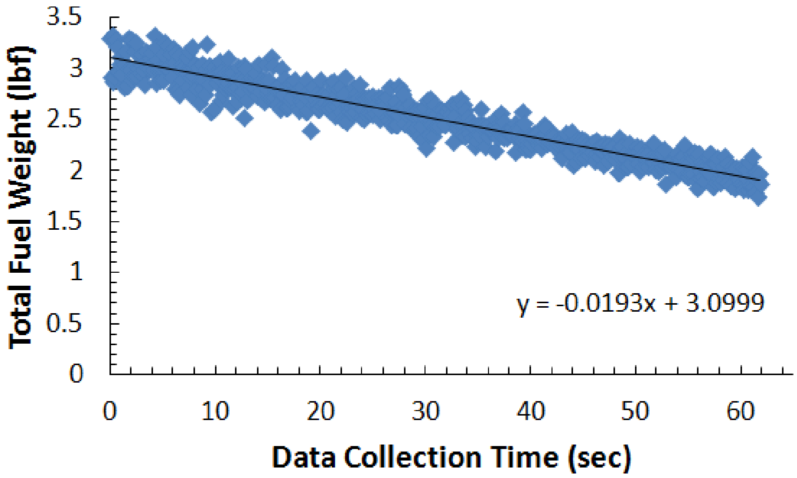

Figure 36. Fuel weight vs. time for a single engine run at 80% throttle.

For the fuel weight data in Figure 36, the equivalent fuel flow rate is 0.0193 lbf/sec (or 0.00875 kg/sec).

4.3.4 Temperatures

Ambient and axial engine stage temperature measurements are made using K-Type thermocouples provided by AMT with the Olympus engine. Unfortunately, AMT could not disclose the manufacturer of these thermocouples. Output from the thermocouples is recorded in units of °C. Assuming the error limits of the AMT-supplied thermocouples are similar to those of K-Type thermocouples manufactured by Omega [87], the accuracy of the thermocouples is assumed to be roughly +/- 0.75% of the measured value. Refer to the schematic drawing of the Olympus (Figure 12) for the location of the temperature measurement ports and the orientation of the thermocouples in the flow. The engine’s hot section thermocouples (T_{04} and T_{05}) need to be corrected for losses due to conduction and radiation. This is discussed later in

Section “4.4 Thermocouple Corrections”. The exhaust gas temperature (T_{06}) is displayed by the engine’s electronic data terminal (EDT), and its signal cannot be recorded directly. This is because the T_{06} thermocouple is a required input to the engine’s electronic control unit (ECU) for proper start-up and shutdown sequences. T_{06} was recorded by hand during engine testing.

4.3.5 Pressures

The Olympus in “University Configuration” only came equipped with axial engine stage pressure measurements ports and not sensors to make these measurements. Refer to the schematic drawing of the Olympus (Figure 12) for the location of the pressure measurement ports and their orientation in the flow. Pressure measurements are made using Omega PX309-100A5V absolute pressure transducers with a range of 0-100 psia (0-689 kPa) and an accuracy of +/- 0.25% of the measured value. Festo tubing supplied with the engine is inserted into the measurement ports on the engine and connected to the pressure transducers. Again, ambient pressure was simply recorded from the National Weather Service’s website [86] for College Park Airport.

4.3.6 Engine Speed

The Olympus comes equipped with a pre-installed RPM sensor at the compressor stage of the engine. RPM readings from the sensor are displayed on the engine’s electronic data terminal (EDT). The EDT also indicates percent throttle as controlled by the analog throttle knob. The RPM and percent throttle readings from the EDT were recorded by hand during each engine run.

4.3.7 Data Acquisition

A National Instruments NI 9205 analog input module and a NI 9213 thermocouple module installed in a cDAQ-9178 chassis logs all measurements (excluding ambient pressure, T_{06}, RPM, and percent throttle) at 10 Hz. Five throttle sweeps spanning 20% to 100% throttle were performed. This provided five data points for each operating condition which are used to compute the averages presented later in this work. For each data point, raw measurements (excluding fuel weight) are averaged over the testing period which generally lasted about 60 seconds. At a sampling rate of 10 Hz, this means that each data point (excluding fuel flow rate) represents an average of approximately 600 raw measurements.

4.3.8 Summary of Measurements

Table 11 shows all measured quantities in this work.

Table 11. Summary of measured quantities.

Measured Quantity	Measuring Device
Thrust	Transducer Techniques ESP-35 load cell
Air Flow Rate (Pressure Drop)	Meriam Z50MC2-6 laminar flow element; Omega PX277-30D5V differential pressure transducer
Fuel Flow Rate (Fuel Weight)	Transducer Techniques ESP-20 load cell
Ambient Temperature (T_{amb})	K-Type thermocouple
T_{03}	K-Type thermocouple
T_{04}	K-Type thermocouple
T_{05}	K-Type thermocouple
T_{06}	K-Type thermocouple
Ambient Pressure (P_{amb})	National Weather Service's website for College Park Airport
P_{s3}	Omega PX309-100A5V pressure transducer
P_{03}	Omega PX309-100A5V pressure transducer
P_{04}	Omega PX309-100A5V pressure transducer
P_{05}	Omega PX309-100A5V pressure transducer
Engine Speed (RPM)	Engine ECU/EDT
% Throttle	Engine ECU/EDT

4.4 Thermocouple Corrections

The measured values of the turbine inlet temperature (T_{04}) and turbine exit temperature (T_{05}) in this work are significantly lower than the NPSS predicted values. This is probably due to conduction and radiation losses in the T_{04} and T_{05} thermocouples. The discrepancy between predicted theoretical and measured temperatures in the hot sections of the Olympus in "University Configuration" was also observed by Prof. Harald Funke[3], who provided preliminary performance data to assist initial efforts in testing the NPSS model before the experiments were completed. Bakalis and Stamatis [30] made this observation as well. Conduction and radiation loss corrections in this work are calculated by modeling the T_{04} and T_{05} thermocouple sheaths as pin fins in a cross flow [88]–[90].

4.4.1 Pin Fin Model

The K-Type thermocouples provided by AMT consist of a thin stainless steel sheath that protects the sensor lead wires. These thermocouple sheaths protrude directly into the flow of the engine (see Figure 37).

---

[3] Professor, Aachen University of Applied Sciences, Aachen, Germany

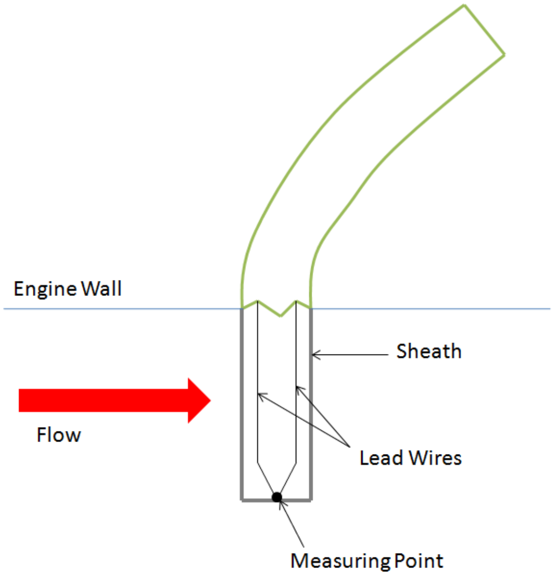

Figure 37. Sheathed thermocouple orientation in flow.

Temperature measurement error is due to axial conduction along the length of the sheath, radiation heat transfer between the sheath and the engine walls, and convection between the sheath and gas. This causes under-prediction of the true gas temperature. A simple method of estimating the measurement error involves modeling the sheathed thermocouple as a pin fin [88]–[90] (see Figure 38).

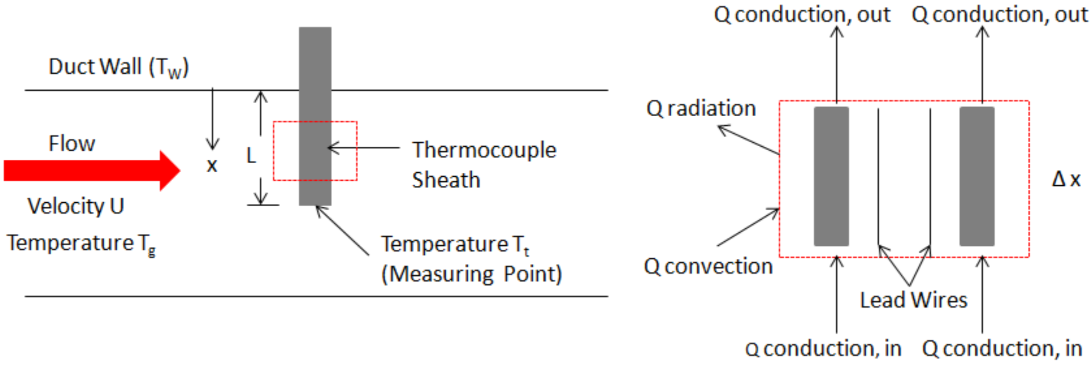

Figure 38. Thermocouple well pin fin model.

The particular approach used in this work for estimating thermocouple temperature measurement errors follows that of [90]. It is assumed that the cross-sectional area of the sheathed thermocouple assembly (effectively the pin) is significantly larger than that of the thermocouple lead wires, so conduction through the wires themselves can be neglected. It is also assumed that the temperature of the sheath is between that of the gas and the wall so that it is heated by convection from the gas and cooled by radiation to the engine walls. The radiation heat flux from the gas to the sheath is approximated using a linearized model [90]:

$$q_R = 4\varepsilon\sigma T_w^3 (T - T_w) = h_R (T - T_w) \tag{32}$$

where the radiation heat transfer coefficient, h_R, is given by:

$$h_R = 4\varepsilon\sigma T_w^3 \tag{33}$$

The linearized form of the radiation heat flux in equation (32) can be used here because it is assumed that the temperature at any point along the thermocouple sheath (T) is of the same order of magnitude as the temperature of the wall (T_w) [91]. The greatest difference between T and T_w occurs when considering the sheath tip temperature (T_t) at full throttle engine operation. At 100% throttle, $T_t \cong 1050$ K and T_w is assumed to be 450 K at the turbine inlet, and $T_t \cong 950$ K and T_w is assumed to be 600 K at the turbine exit. Here, the values of T_t are the raw measured (uncorrected) temperatures at the turbine inlet/exit, and the values of T_w are the assumed wall temperatures at the turbine inlet/exit (see Section "4.4.3 Parameters for the Thermocouple Corrections").

The temperature correction is determined by performing an energy balance on the differential sheath element illustrated in Figure 39.

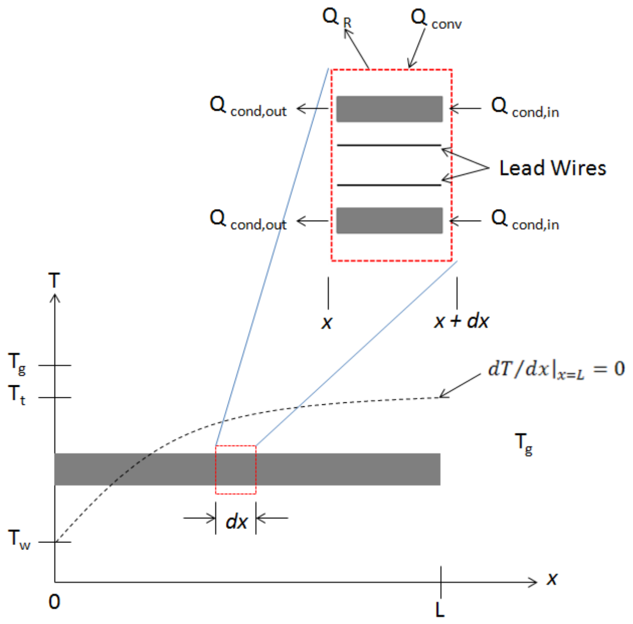

Figure 39. Differential sheath element.

The rates of convective heat transfer from the flow to the sheath (Q_{conv}), radiation to the wall (Q_R), conduction into ($Q_{cond,in}$), and conduction out ($Q_{cond,out}$) are given by equations (34) – (37) [90]:

$$Q_{conv} = h_{conv} P \Delta x (T_g - T) \tag{34}$$

$$Q_R = h_R P \Delta x (T - T_w) \tag{35}$$

$$Q_{cond,in} = k_w A \left.\frac{dT}{dx}\right|_{x} \tag{36}$$

$$Q_{cond,out} = k_w A \left.\frac{dT}{dx}\right|_{x-\Delta x} \tag{37}$$

In equations (34) – (37), P is the perimeter of the thermocouple sheath and A is the annular cross-sectional area of the thermocouple sheath. Performing a simple energy balance on the differential sheath element (see Figure 39) yields the following:

$$Q_{conv} + Q_{cond,in} = Q_R + Q_{cond,out} \tag{38}$$

Substituting equations (34) – (37) into equation (38) yields a second order differential equation for the sheath temperature (T) as a function of distance along the sheath (x) where the tip is at $x = L$ [90]:

$$\frac{d^2T}{dx^2} - \frac{(h_{conv} + h_R)P}{k_w A}T + \frac{h_{conv}P}{k_w A}T_g + \frac{h_R P}{k_w A}T_w = 0 \tag{39}$$

Equation (39) can rewritten in terms of a reference temperature, T_{ref} and effective fin parameter, m_{eff} [90]:

$$\frac{d^2\theta}{dx^2} - m_{eff}^2\theta = 0 \tag{40}$$

where $\theta = T - T_{ref}$ and m_{eff} is defined as [90]:

$$m_{eff} = \sqrt{\frac{(h_{conv} + h_R)P}{k_w A}} \tag{41}$$

The reference temperature, T_{ref}, is defined as [90]:

$$T_{ref} = \frac{h_{conv}T_g + h_R T_w}{h_{conv} + h_R} \tag{42}$$

Assuming an insulated boundary condition at the sheath tip ($dT/dx|_{x=L} = 0$), equation (40) can be solved for the indicated thermocouple temperature [90]:

$$\theta_t = \left(T_t - T_{ref}\right) = \frac{\left(T_w - T_{ref}\right)}{\cosh(m_{eff}L)} \tag{43}$$

where $\theta_t = T_t - T_{ref}$ and T_t is the temperature at the tip of the sheath. Finally, the thermocouple measurement error ($T_t - T_g$) is given by [90]:

$$(T_t - T_g) = \left(T_{ref} - T_g\right) + \frac{\left(T_w - T_{ref}\right)}{\cosh(m_{eff}L)} \tag{44}$$

Solving for the true gas temperature (T_g) in equation (44) gives:

$$T_g = \frac{T_t \cosh\left(m_{eff}L\right)(h_{conv} + h_R) - T_w\left[h_R \cosh\left(m_{eff}L\right) + h_{conv}\right]}{h_{conv} \cosh\left(m_{eff}L\right) - h_{conv}} \tag{45}$$

This analysis shows that the measurement error (Eq. (44)) decreases with increasing immersion depth (L), decreasing thermal conductivity, decreasing emissivity, and increasing fluid velocity.

4.4.2 Determining the Convective Heat Transfer Coefficient

Calculating T_g as described above requires an estimate of the convective heat transfer coefficient (h_{conv}). It is defined as [88]:

$$h_{conv} = \frac{Nuk_g}{L} \tag{46}$$

where Nu is the Nusselt number, k_g is the thermal conductivity of the gas, and L is the thermocouple sheath immersion depth into the flow. Nu is estimated using the Zhukaskas correlation for a cylinder in a cross flow [90]:

$$Nu = CRe^{m}Pr^{n} \tag{47}$$

where the constants C and m are dependent on Reynolds number (Re) and n is dependent on Prandtl number (Pr). Values for these constants used in this work are given in the next section.

4.4.3 Parameters for the Thermocouple Corrections

The parameters used to calculate the thermocouple corrections in this work are presented in Table 12.

Table 12. Parameters used to calculate T_{04} and T_{05} thermocouple corrections.

Constants				
Parameter	*Description*	*Value*	*Units*	*Ref.*
σ	Stefan-Boltzmann constant	5.67e-8	W/m^2/K^4	[88]
R_{air}	Ideal gas constant for air	287	J/kg-K	[88]
P	Thermocouple sheath perimeter	12.47	mm	
A	Thermocouple sheath conduction area	10.52	mm^2	
Zhukaskas Correlation Parameters				
Parameter	*Description*	*Value*	*Units*	*Ref.*
C	Zhukaskas correlation constant	0.26		[90]
m	Zhukaskas correlation constant	0.6		[90]
n	Zhukaskas correlation constant	0.36		[90]
Pr	Prandtl number	0.7		
T_{04} Correction				
Parameter	*Description*	*Value*	*Units*	*Ref.*
ε	Wall emissivity	0.75		[88]
k_w	Thermocouple sheath thermal conductivity	20.0	W/m/K	[88]
L	Thermocouple sheath immersion length	17.1	mm	
T_w	Assumed wall temperature	450	K	
T_{05} Correction				
Parameter	*Description*	*Value*	*Units*	*Ref.*
ε	Wall emissivity	0.75		[88]
k_w	Thermocouple sheath thermal conductivity	18.0	W/m/K	[88]
L	Thermocouple sheath immersion length	7.94	mm	
T_w	Assumed wall temperature	600	K	

Values for turbine inlet/exit wall emissivity and thermocouple sheath wall thermal conductivity were estimated from available data for stainless steel [88]. Similarly, values for dynamic viscosity and thermal conductivity of the gas (k_g) used to calculate the convective heat transfer coefficient (h_{conv}) were estimated from tabulated data for air as a function of temperature [88].

Thermocouple corrections at the compressor exit (T_{03}) and nozzle exit (T_{06}) were not computed. The user's manual [92] of the Olympus states that the inlet casing at the compressor generally reaches a temperature of about 400 K. The raw measured T_{03} temperatures ranged between 360 K and 480 K for all engine speeds considered.

Because the raw measured T_{03} values are relatively close to the compressor wall temperature, the corrections calculated according to the analysis above would be minimal. The results reported later in this work suggest this was a reasonable assumption. T_{06} was not corrected because the exhaust pressure is not measured in this work. The exhaust pressure is required for an estimate Re (and hence Nu and h_{conv}).

4.5 Estimating Uncertainty

This section describes the uncertainties in the measured and calculated quantities reported in this work. Uncertainties are indicated in the results section with error bars that represent a 95% confidence interval for each measured/calculated data point.

4.5.1 Measurement Uncertainty

Measurement error consists of two components: random error and systematic error. Random errors are random deviations around the mean and can be reduced by increasing the number of samples. Systematic errors are the component of the total error that has to do with the instrument/measurement method itself and remain constant during repeated measurements [93]. In this work, the random component of the error is taken to be the standard deviation about the mean, $S_{\bar{x}}$ [93]:

$$S_{\bar{x}} = \frac{S_x}{\sqrt{N}} = \sqrt{\frac{\sum_{i=1}^{N}(x_i - \bar{x})^2}{N-1}} \cdot \frac{1}{\sqrt{N}} \tag{48}$$

where x_i is the i^{th} measurement of the quantity of interest, $\bar{x}$ is the mean of the measured quantity based on N samples, and S_x is the standard deviation of N

samples. Since five throttle sweeps were conducted, there are 5 performance measurements at each engine speed and thus N = 5.

Systematic errors arise primarily from the accuracy, linearity and repeatability limits of the sensors used to make measurements (thermocouples, pressure transducers, load cell, thrust balance, etc.). The total systematic uncertainty, B, is calculated using [93]:

$$B = \sqrt{(b_1)^2 + (b_2)^2 + \cdots + (b_k)^2} \tag{49}$$

where $b_1 \ldots\ b_k$ are the systematic errors in the measurements (such as linearity and repeatability limits of the sensors). The total measurement uncertainty ($U_{\bar{x}}$) for a 95% confidence level for a measurement is given by [93]:

$$U_{\bar{x}} = 2\sqrt{\left(\frac{B}{2}\right)^2 + (S_{\bar{x}})^2} \tag{50}$$

where B is the systematic error and $S_{\bar{x}}$ is the standard deviation of the mean. The true value of the measurement (X_t) is then reported as:

$$X_t = \bar{X} \pm U_{\bar{x}} \tag{51}$$

where $\bar{X}$ is the mean given by:

$$\bar{X} = \frac{1}{N}\sum_{i=1}^{N} X_i \tag{52}$$

where X_i is the measurement, and N is the number of data points.

4.5.2 Uncertainties in Calculated Results

The total error in calculated results is also comprised of random and systematic components. As with measured quantities, the random error of a result is calculated using the standard deviation of the mean for repeated tests [93]:

$$S_{\bar{R}} = \frac{S_R}{\sqrt{N}} = \sqrt{\frac{\sum_{i=1}^{N}(R_i - \bar{R})^2}{N-1}} \cdot \frac{1}{\sqrt{N}} \tag{53}$$

where S_R is the standard deviation of the sample, $\bar{R}$ is the mean of the calculated result, R_i is the calculated result, and N is the total number of tests performed.

Systematic error (B_R) in a quantity calculated using I measured quantities is given by [93]:

$$B_R = \sqrt{\sum\nolimits_{i=1}^{I}(\theta_i b_{\bar{X}_i})^2} \tag{54}$$

where $b_{\bar{X}_i}$ is the systematic error of the measured parameter determined using equation (49). The symbol θ_i is the sensitivity coefficient of the measured parameter $\bar{X}_i$ and is defined as:

$$\theta_i = \frac{\partial R}{\partial \bar{X}_i} \tag{55}$$

where R is the calculated result.

The total uncertainty of a result with 95% confidence is then:

$$U_{\bar{R}} = 2\sqrt{\left(\frac{B_R}{2}\right)^2 + (S_{\bar{R}})^2} \tag{56}$$

where B_R is the total systematic error in the result, and $S_{\bar{R}}$ is the standard deviation about the mean. The true value of the result (R_t) is then expected to be:

$$R_t = \bar{R} \pm U_{\bar{R}} \tag{57}$$

where $\bar{R}$ is the mean result calculated using equation (52).

4.6 Experimental Procedures

This section outlines the procedures used to measure the performance of the Olympus engine. A more detailed discussion of the engine's operation and troubleshooting is provided in the user's manual for the Olympus [92].

4.6.1 Preparing the Engine

1. Ensure that the engine battery is fully charged or at least has sufficient charge for the engine's ECU to initiate the start-up sequence (refer to user's manual [92] for the minimum charge required for start-up). It is good practice to have the battery as close to fully charged as possible for proper ECU function.
2. Ensure that all inputs (electric starter, T_{06} thermocouple, fuel pump, throttle controller, RPM sensor, etc.) to the ECU are securely connected. It is also important to make sure the throttle controller is communicating properly with the ECU (refer to "Dual Channel Operation" in the user's manual [92]).
3. Ensure that there is enough fuel in the fuel tank. The fuel is a mixture of 95% Jet-A and 5% AeroShell 500 turbine oil. Make sure the fuel lines are securely connected to the engine and there are no leaks.
4. Inspect the engine for any damage prior to start-up.

4.6.2 Preparing the Test Facility

1. Ensure that all thermocouples attached to the engine are securely connected, and make sure the tubing connecting the pressure measurement ports on the engine to the pressure transducers is intact.
2. Place the containment housing over the engine and thrust stand, and turn on the fume hood attached to the exhaust ejector. Make sure that all of the other

hoods in the lab are off. Note that it takes a few minutes for the hood to achieve maximum power.

3. Turn on both load cell signal conditioners (i.e., for the thrust and fuel flow rate measurements), the power supply for the pressure transducers, and the LabView modules. Allow this equipment roughly 10 minutes to warm-up. This is particularly important for the load cell signal conditioners prior to calibration.
4. Ensure the wiring for all measuring devices is properly configured.
5. Calibrate the thrust stand according to the procedure described in Section “4.3.1 Thrust”.

The engine and test facility are now ready for data collection.

4.6.3 Data Collection

1. Switch on the engine’s ECU. When the engine’s EDT indicates the engine is ready for start-up, initiate the start-up sequence. Refer to the user’s manual [92] for interpretation of the EDT’s graphic display and how to initiate start-up. After successful start-up, the ECU will automatically throttle the engine to idle (~36,000 RPM).
2. Once the engine achieves idle RPM, adjust the throttle knob to the desired throttle setting. Throttle setting is displayed on the EDT as a percentage of maximum thrust.
3. Allow the engine to equilibrate for about 60 seconds after each throttle change before acquiring data.

4. After about 60 seconds of data collection, stop recording data. During the data collection period, be sure to record the engine's RPM and throttle setting from the engine's EDT. The speed and percent throttle should remain fixed over the data collection period.
5. Initiate the engine's automatic shut-down sequence (refer to user's manual [92]). During the shut-down sequence, the ECU will rotate the compressor until T_{06} cools to the desired temperature. During this time, turn on all hoods in the lab to expel any residual exhaust present in the lab.
6. Once the ECU stops rotating the compressor, switch off the ECU. The engine is now completely powered off.
7. To run the engine again at a different throttle setting, repeat the steps in this section ("4.6.3 Data Collection"). Allow roughly 10 minutes between each engine run for the fume hoods to remove any exhaust present in the lab. Remember to turn off all hoods except for the one attached to the exhaust ejector before the next run. Also, make sure the engine's battery has sufficient charge and there is enough fuel for the next run.

4.6.4 Safety

The engine operator and close observers should wear hearing and eye protection at all times during engine operation. Other lab occupants should at least wear hearing protection. Any debris or light and loose objects should be kept away from the engine's inlet (this includes fuel lines and any sensor wires) as these can be ingested due to the engine's powerful suction. The engine operator and any lab occupants should also maintain a safe distance from the engine's nozzle during operation. A description of the engine’s “Danger Zone(s)” with diagrams can be found in the user’s manual [92]. The containment housing should always cover the engine during operation to protect against catastrophic failure. A fire extinguisher should be kept nearby as well. As with any experiment, it is also good practice to have at least one other person present during testing.

Chapter 5: Results & Discussion

5.1 Summary of Experiments Performed

The Olympus engine was tested with and without the air flow rate measurement apparatus mentioned previously. Five throttle sweeps were performed in both cases, collecting performance data at engine speeds between 20% and 100% throttle. The averaged results for both cases (i.e., with and without air flow rate measurements) are presented in “Appendix D: Experimental Data”. The averaged data for the case without the air flow measurement are used to validate the current NPSS model of the engine. This is because the duct and plenum used to connect the engine to the laminar flow element corrupts the thrust measurement as explained earlier.

5.2 Results

5.2.1 Axial Stage Pressure & Temperature Comparison

Figure 40 shows the measured and simulated total pressures and temperatures at each axial stage (see Figure 3) along the engine for the design case.

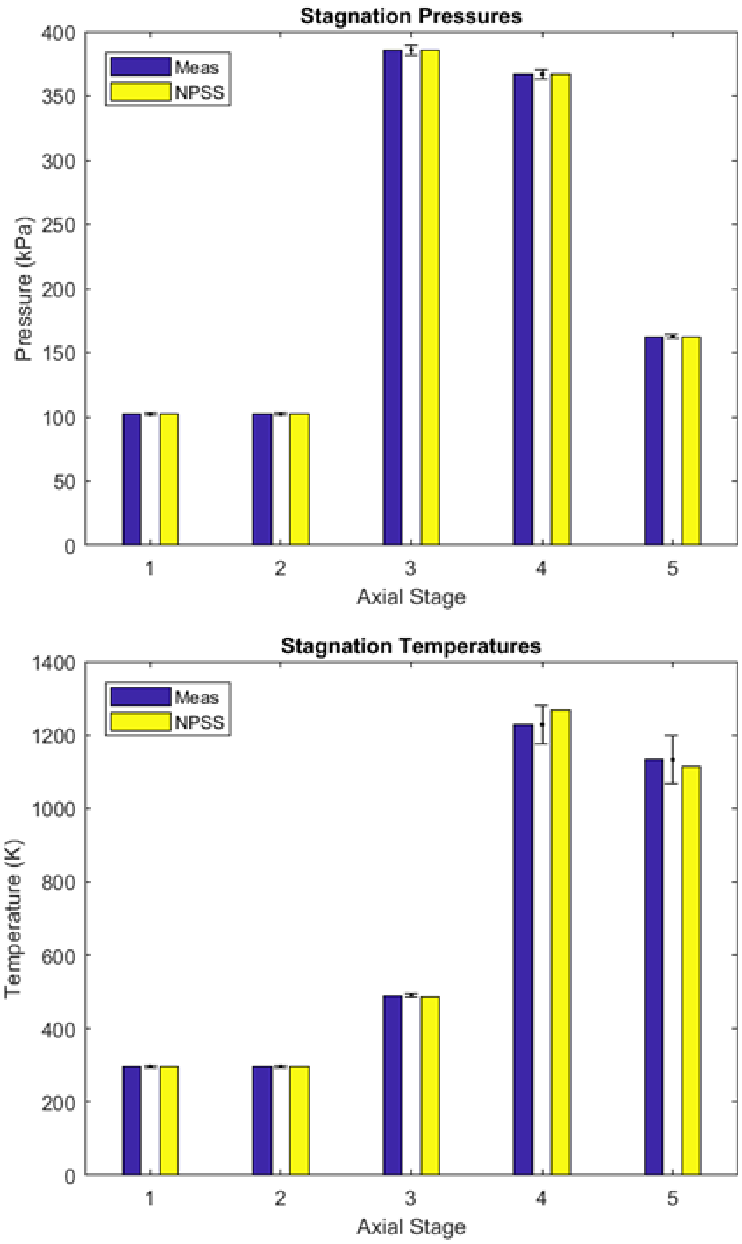

Figure 40. Axial stage pressures (top) and temperatures (bottom) at full throttle (design case).

Figure 40 shows that interstage pressures and temperatures are predicted within the margin of experimental error at all positions in the cycle when the engine runs at 100% power. Note that the pressures and temperatures at stage 1 (ambient) and stage 2 (compressor inlet) are equal in the experiment and the NPSS model predictions. This is because the "University Configuration" of the Olympus does not provide total pressure and temperature measurements at the compressor inlet, and it was assumed that the flow conditions at the compressor inlet were simply equal to ambient conditions. This is a reasonable assumption because typical diffuser efficiencies are close to 1.0 [10]. For this reason, the diffuser/inlet efficiency in the NPSS model was also assumed to be 1.0.

Uncertainties in T_{04} and T_{05} are relatively large (~ +/-70 K), due to the uncertainties in the parameters used to make the thermocouple corrections (i.e., wall emissivity, thermal conductivity, wall temperature, dynamic viscosity, etc.).

Figure 41 shows the percent difference between measured and predicted axial stage stagnation pressures and temperatures at various throttle settings. Temperatures are predicted within 5% at all throttle settings and pressure to within 2.5% except P_{03} and P_{04} at 20% throttle which are predicted to within about 9%.

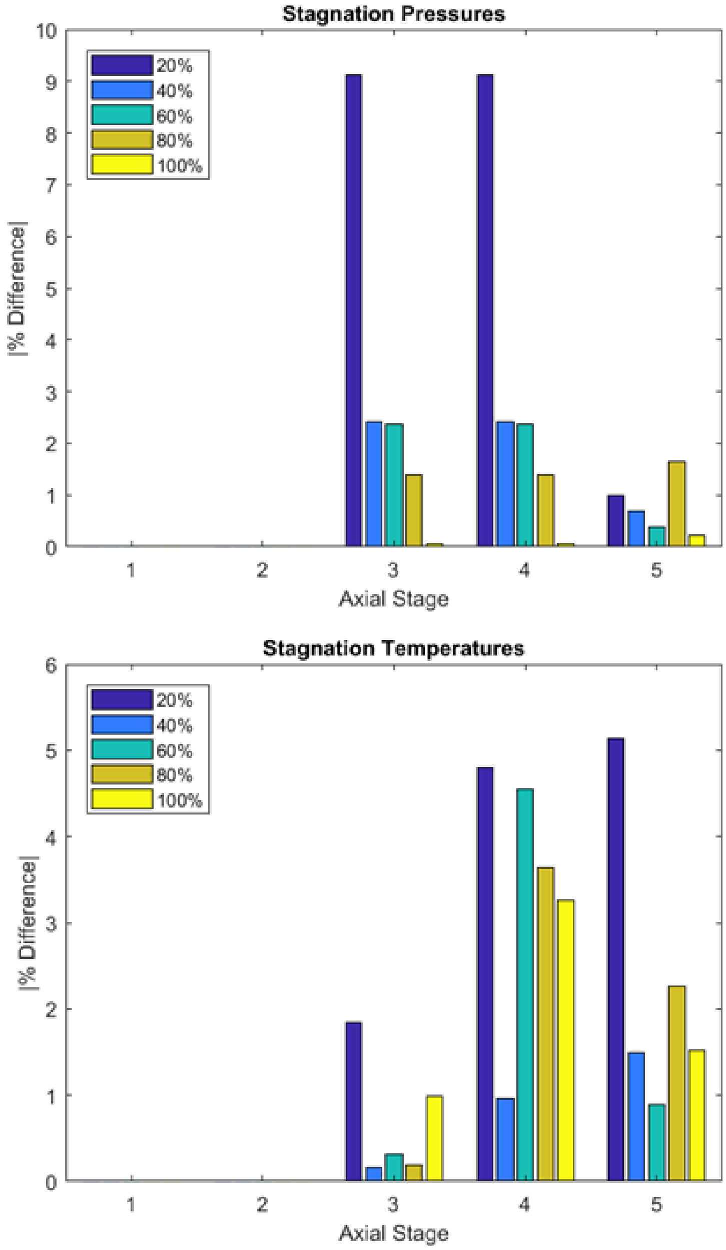

Figure 41. Percent difference between predicted and measured total pressures (top) and temperatures (bottom) at various throttle settings.

This suggests that the NPSS model’s compressor performance map is less accurate in predicting the compressor pressure ratio (P_{03}/P_{02}) at lower throttle settings. Differences between measurements and predictions at stages 1 and 2 are zero because the ambient pressure and temperature are inputs to the NPSS model, and as explained earlier, no measurements are actually made at station 2.

5.2.2 Thrust, Fuel Flow Rate, & TSFC Comparison

Figure 42 compares the measured and predicted thrust as functions of corrected RPM (defined in “Appendix A: Compressor & Turbine Performance Maps”) and throttle setting.

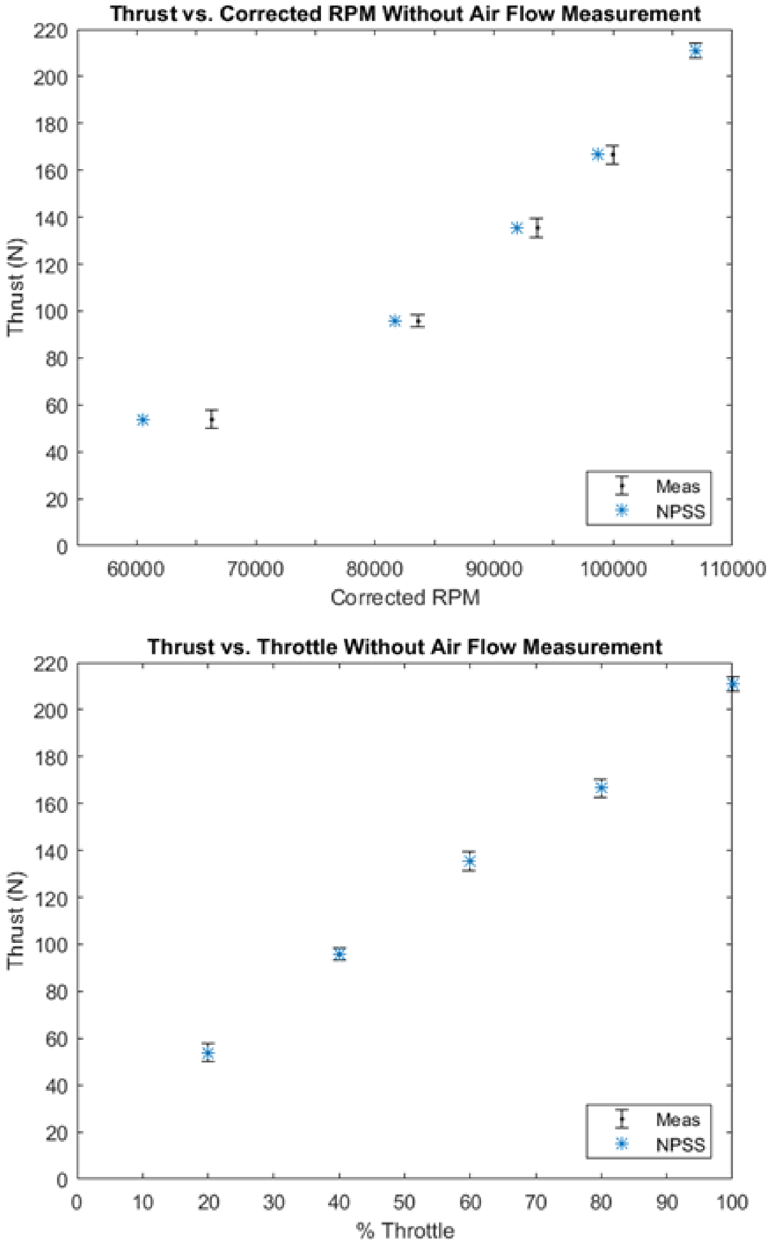

Figure 42. Thrust as a function of corrected RPM (top) and throttle setting (bottom).

Recall that measured thrust is a dependent condition for the NPSS solver during on- and off-design analysis. During off-design cases, the solver adjusts certain independents (which include RPM) such that the calculated thrust equals the measured thrust at each throttle setting (see Section “3.3.2 Independents and Dependents”). Because the exhaust static pressure (P_{s6}) is not measured, NPSS cannot predict exhaust velocity (and thus thrust) directly from the measured interstage pressures and temperatures. Although the measured and NPSS thrust values are equal at each throttle setting (bottom plot of Figure 42), they are offset from each other when plotted against corrected RPM (top plot of Figure 42). This is due to the difference between measured and predicted corrected RPM at each throttle setting (see Figure 43).

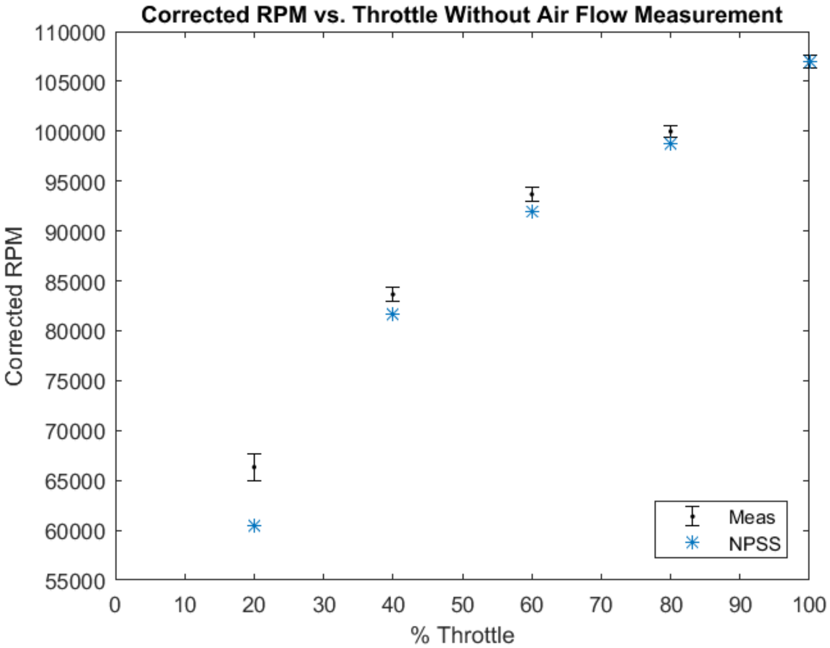

Figure 43. Comparison between measured and predicted corrected RPM.

The corrected RPM values are equal at full throttle because this was the design point for the NPSS model, and the NPSS solver does not adjust RPM in design mode. The offset in RPM may be due to the inaccuracy of the turbomachinery maps used to predict compressor and turbine performance.

Similarly, the measured fuel flow rate is an input to the NPSS model, so the experimental values equal the model values. The same offset in corrected RPM observed with thrust is also observed when comparing fuel flow rate values (see Figure 44).

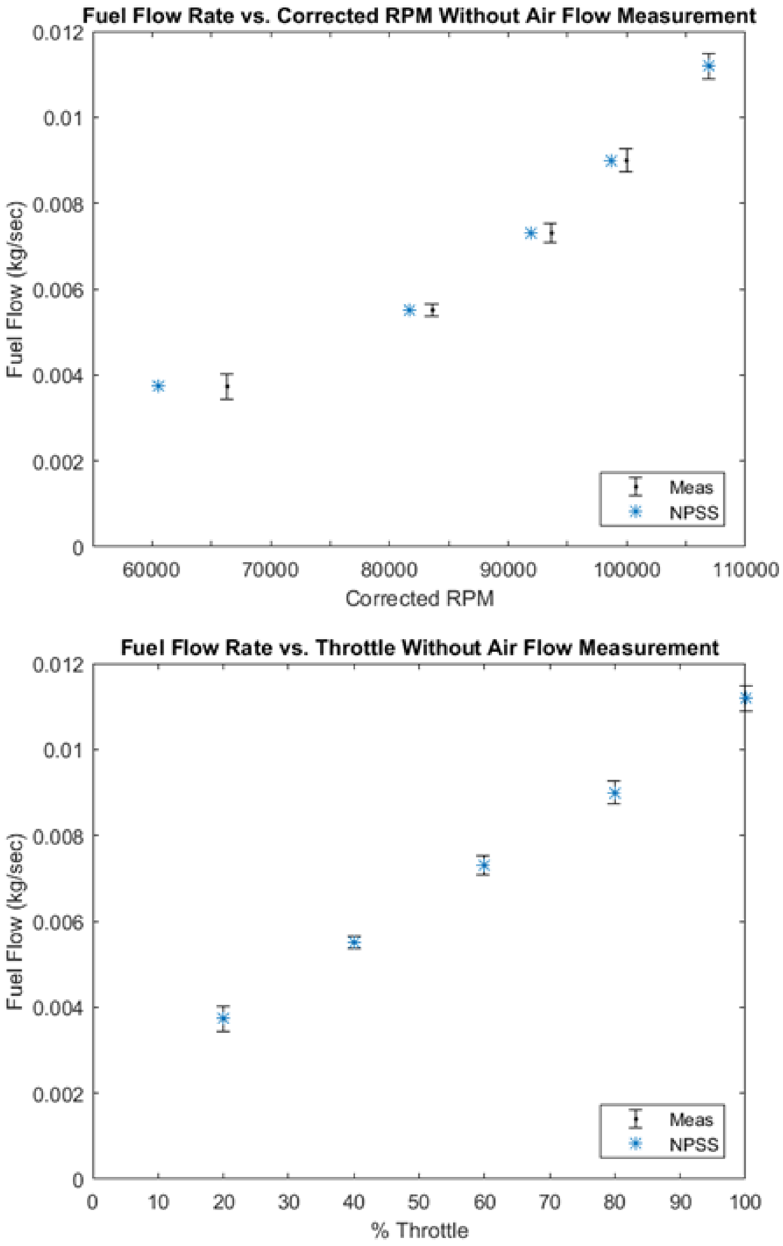

Figure 44. Fuel flow rate as a function of corrected RPM (top) and throttle setting (bottom).

Because the experimental and simulated values of thrust and fuel consumption are equal, the values for TSFC ($= \dot{m}_{fuel}/F_{th}$) are also equal (see Figure 45). Again, there is a slight offset with corrected RPM.

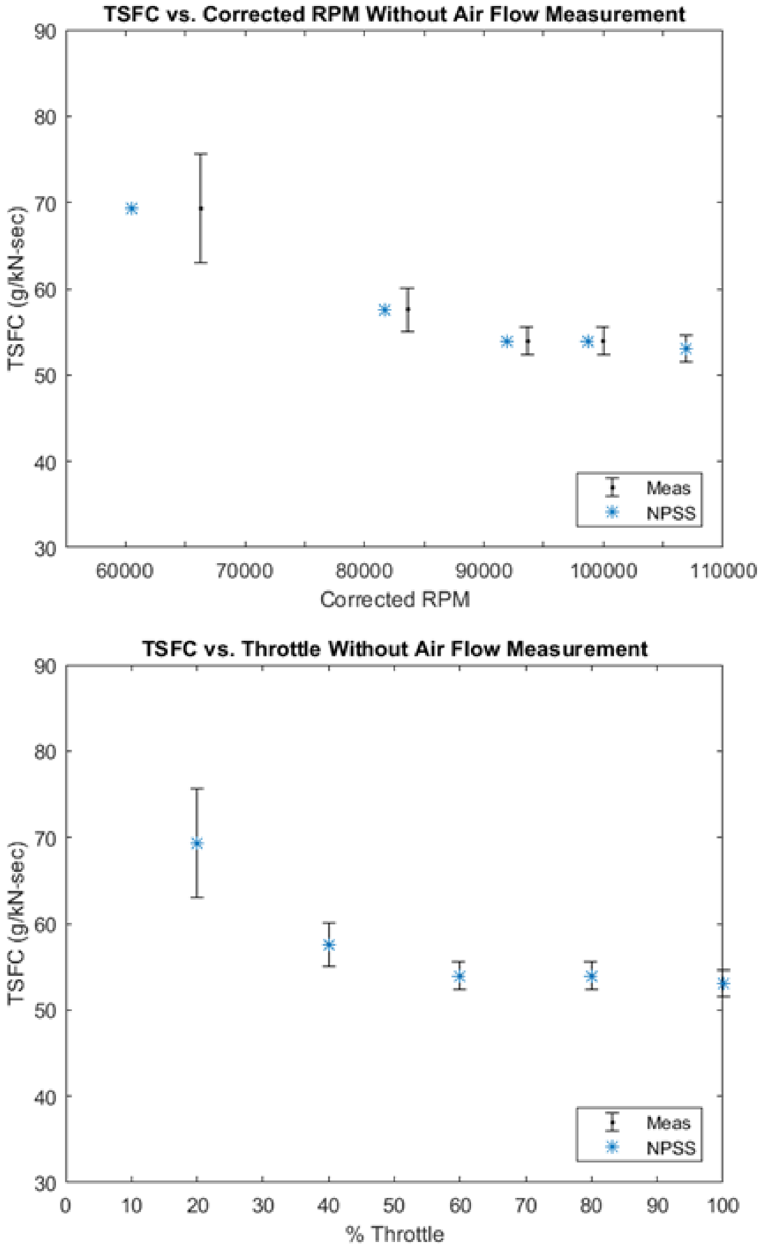

Figure 45. TSFC as a function of corrected RPM (top) and throttle setting (bottom).

5.2.3 Predicted Air Flow Rate, Exhaust Static Pressure, &Turbine Efficiency

Because the NPSS model of the Olympus is based on the data without air flow rate measurements, air flow is varied by the NPSS solver as an independent to meet the dependent conditions instead of being a fixed input to the model. Figure 46 shows the predicted air flow rate as a function of engine speed.

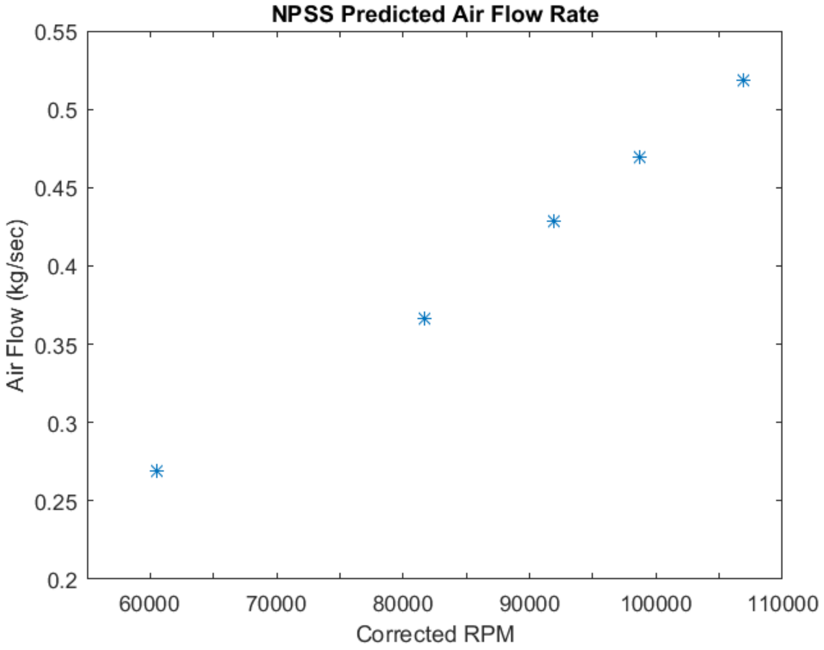

Figure 46. Predicted air flow rate as a function of engine speed.

The maximum predicted air flow rate at full speed of about 0.52 kg/sec is greater than the maximum rated air flow rate (AMT's specification at full throttle) of 0.45 kg/sec. This may suggest that the actual compressor performance map is different from the map provided by AMT. For instance, Leylek [34] measured a maximum air flow rate of 0.5 kg/sec, which is 10% larger than the value specified by AMT. Another possibility is that the compressor on our engine is not performing to specifications due to damage incurred during testing when the RPM sensor wire was ingested into the engine. This damaged the compressor wheel and some of the internal engine components. While the engine was returned to the manufacturer to have the compressor wheel replaced and the engine rebalanced, the engine may not be the same as it was before.

Uncertainties in the air flow rate predictions (compressor map) may also propagate through other predicted parameters such as RPM. As illustrated before, NPSS predictions for RPM are outside of the experimental margin of error. Resolving the issues with the current method of measuring air flow rate will allow a compressor map to be determined experimentally. Replacing the map provided by AMT in the current NPSS model with an experimentally determined compressor performance map should reduce the uncertainty in the predicted air flow rate and reduce error propagation to other predicted parameters.

Exhaust static pressure (not measured) is also varied by the NPSS solver to meet the dependent conditions. Figure 47 shows the predicted P_{s6} as a function of engine speed.

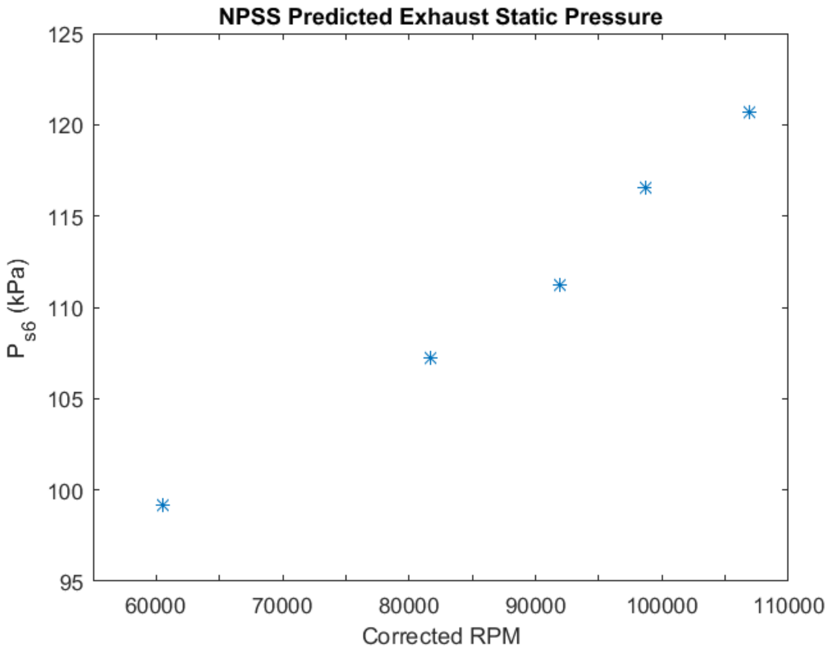

Figure 47. Predicted exhaust static pressure as a function of engine speed.

At higher engine speeds (40% – 100% throttle), NPSS predicts P_{s6} to be greater than ambient pressure (~100 kPa). This may make physical sense when considering the performance of the exhaust ejector. As mentioned previously, the fume hood attached to the exhaust ejector cannot keep up with the engine's exhaust at speeds greater than about 40% throttle. The fume hood's inability to engulf the engine's exhaust will presumably create backpressure behind the nozzle. Since the Olympus in "University Configuration" does not provide a P_{s6} measurement port, a method of making this measurement to confirm the NPSS predicted values still needs to be developed.

Another parameter adjusted by the NPSS solver is turbine efficiency which is depicted in Figure 48.

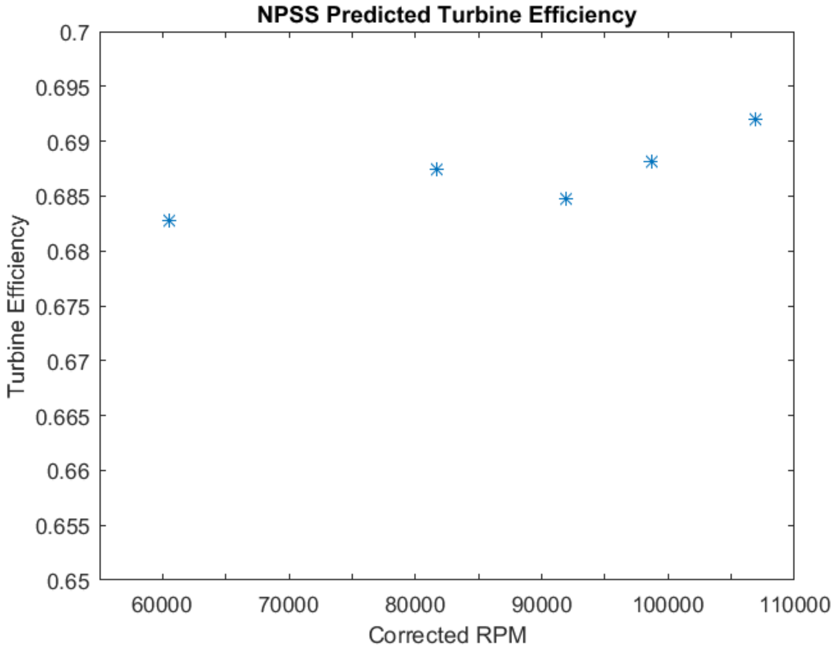

Figure 48. Predicted turbine efficiency as a function of engine speed.

There appears to be a slight increase in turbine efficiency as the engine speed increases. The minimum turbine efficiency of 0.683 occurs at about 60,000 corrected RPM, and the maximum turbine efficiency of 0.692 occurs at about 107,000 corrected RPM. Recall that turbine performance is predicted using a scaled low pressure turbine map from GE. There is some uncertainty associated with scaling a turbine map from a larger engine to the size required for a smaller engine. This uncertainty will certainly affect predicted turbine efficiency and other predicted parameters (such as RPM). As with the current compressor map, the GE turbine map could be replaced with an experimentally determined performance map once the issues with the air flow rate measurements are resolved.

5.2.4 Thrust with & without Air Flow Rate Measurement

As discussed previously, the air flow rate measurement apparatus reduces the freestream pressure significantly. While this should reduce the thrust produced by the engine, the measurements indicate that this not the case (see Figure 49). This apparently non-physical result suggests that the air flow measurement may be corrupting the thrust measurement.

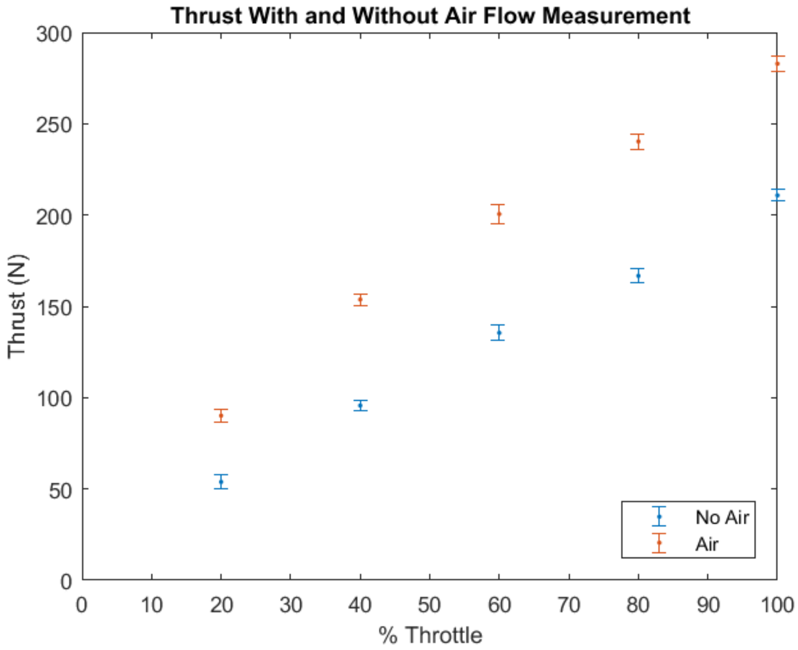

Figure 49. Thrust comparison for the case with and without the air flow rate measurement.

Figure 49 shows that the measured thrust is significantly larger when air flow rate is measured compared to when it is not despite the larger inlet pressure losses when the air flow rate measurement apparatus is installed.

One possible explanation is that this discrepancy is caused by the difference in pressure between the lab and the air plenum. Air in the lab (which is at a greater pressure than that inside the plenum) pushes on the flexible rubber diaphragm forcing it inward toward the plenum. Since the diaphragm is connected to the inlet extension which, in turn, is connected to the thrust stand, this force may be transmitted to the thrust stand in a way that adds to the thrust of the engine. Resolving this problem will require a complete re-design of the air inlet and plenum. The apparently non-physical thrust measurements associated with the air flow rate measurements are the reason that the current NPSS model has been developed based on the experimental data without air flow rate measurements.

A remedy for this phenomenon would be to replace the LFE-plenum-duct configuration with a bell mouth diffuser that is attached directly to the engine's inlet. This would prevent the need for a diaphragm or any type of rigid attachment of the air flow rate measurement device to the tabletop. At the time of writing this thesis, AMT developed a bell mouth diffuser (or 'extended intake') designed specifically to measure air flow rate for the Olympus engine. A schematic diagram of the Olympus engine with the extended diffuser is provided in Figure 50, and a picture of the Olympus with the diffuser attached is provided in Figure 51.

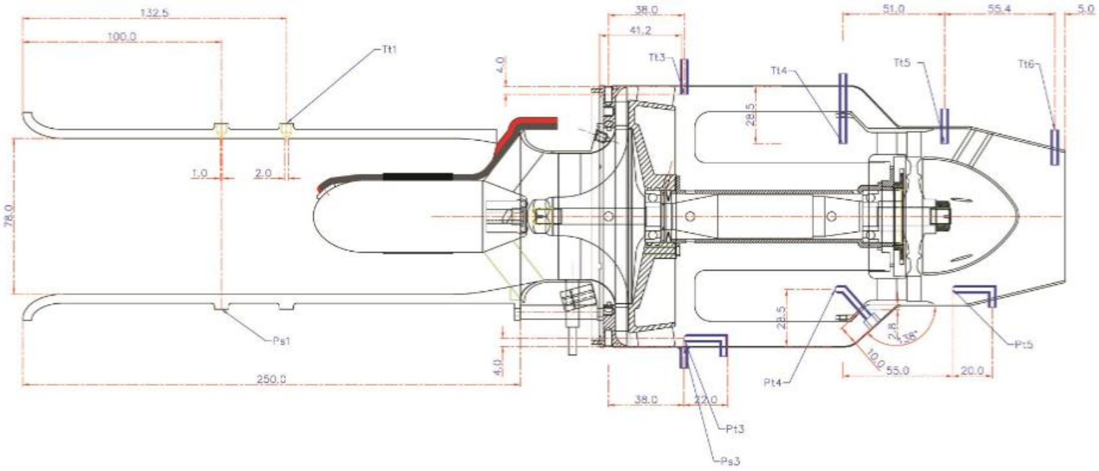

Figure 50. Schematic diagram of the Olympus engine in "University Configuration" with the extended intake [21]**.**

Figure 51. Olympus engine with the extended intake attached to the inlet [21]**.**

When designing the test facility, the LFE was the preferred method of air flow rate measurement because it was a pre-fabricated and pre-calibrated instrument with high accuracy. Unfortunately, there were unforeseen complications with attaching the LFE to the engine without disrupting the thrust measurements. Also, the extended intake for measuring air flow rate for the Olympus was not yet available from AMT.

Chapter 6: Conclusions & Future Work

6.1 Summary & Key Findings

This thesis has developed an experimentally validated thermodynamic model of a small gas turbine engine (AMT Olympus) that will be used as platform for constructing a bench-scale hybrid GT/SOFC system. The thermodynamic model of the engine was created using an industry standard software tool called Numerical Propulsion System Simulation (NPSS). The model uses a compressor map supplied by AMT and a scaled version of one of General Electric's low pressure turbine maps for the turbine. An indoor test facility was constructed to measure the engine's performance. Measurements include axial stage stagnation temperatures and pressures, thrust, fuel flow rate, air flow rate, and engine speed (RPM). Measured turbine inlet (T_{04}) and turbine exit (T_{05}) temperatures are corrected for conduction and radiation losses in the thermocouples. The NPSS model is validated by comparing predicted and experimentally measured performance parameters as functions of engine speed (or throttle setting) for steady state engine operation.

The key findings of this work are summarized below:

- Interstage pressures are predicted to within 2.5% of the measurements with the exception of P_{03} and P_{04} at 20% throttle which are predicted to within 9%
- Interstage temperatures are predicted to within 5% of the measurements
- Predicted air flow rate, exhaust static pressure, and turbine efficiency
    - The maximum NPSS predicted air flow rate is greater than the maximum rated air flow rate (specified by AMT) which could be

due to a change in compressor performance after replacing the original compressor or an inaccuracy in the compressor map provided by AMT

  - P_{s6} is greater than ambient pressure at higher engine speeds which is likely due to the exhaust ejector’s failure to engulf all of the engine’s exhaust at these speeds
  - Turbine efficiency does not appear to be a strong function of engine speed, reaching a minimum of 0.683 at about 60,000 corrected RPM and a maximum of 0.692 at about 107,000 corrected RPM

6.2 Contributions

This work presents two major contributions to modeling and performance testing of small gas turbine engines (particularly the AMT Olympus):

1. Developed an indoor small gas turbine (< 445 N) test facility that measures all global performance parameters (thrust, air flow rate, fuel flow rate, engine speed (RPM), and axial stage stagnation temperatures and pressures)
2. Developed what is believed to be the first Numerical Propulsion System Simulation (NPSS) thermodynamic model of the AMT Olympus gas turbine engine and validated it via comparison to experimental data

6.3 Future Work

Suggested improvements to this work and the next steps toward achieving a functional GT/SOFC prototype are outlined below:

- Replace the LFE-plenum-duct configuration for measuring air flow rate with the extended intake manufactured by AMT to avoid disrupting the thrust measurements
    - Use air flow measurements to create compressor and turbine performance maps based on experimental measurements
    - Replace current turbomachinery maps in NPSS model with the experimentally determined maps
- Replace the MDF tabletop with a more rigid surface such as an optical table breadboard with threaded holes to maintain a rigid contact point between the thrust stand and load cell
- Measure static pressure at the nozzle exit during engine runs
    - Better understand how the presence of the exhaust ejector affects thrust measurements
    - Enables thrust prediction from interstage measurements
- Have fuel samples tested to determine a more accurate lower heating value of combustion to be input into the NPSS burner model
- Perform a sensitivity analysis to examine how certain input parameters (such as compressor/turbine maps) affect NPSS calculations
    - The current NPSS model predictions are sensitive to the uncertainties in the turbomachinery maps (i.e., air flow rate, turbine efficiency, etc.), affecting the ability to make meaningful comparisons to measurements

- Develop an NPSS model of a commercially available SOFC system, and integrate this model into the existing model of the AMT Olympus to design the hybrid prototype system
    - A colleague is currently working toward this aim using the developed NPSS model of the Olympus engine presented in this work

Appendix A: Compressor & Turbine Performance Maps

A.1 Olympus Compressor Map

The compressor map for the Olympus was provided directly from AMT.

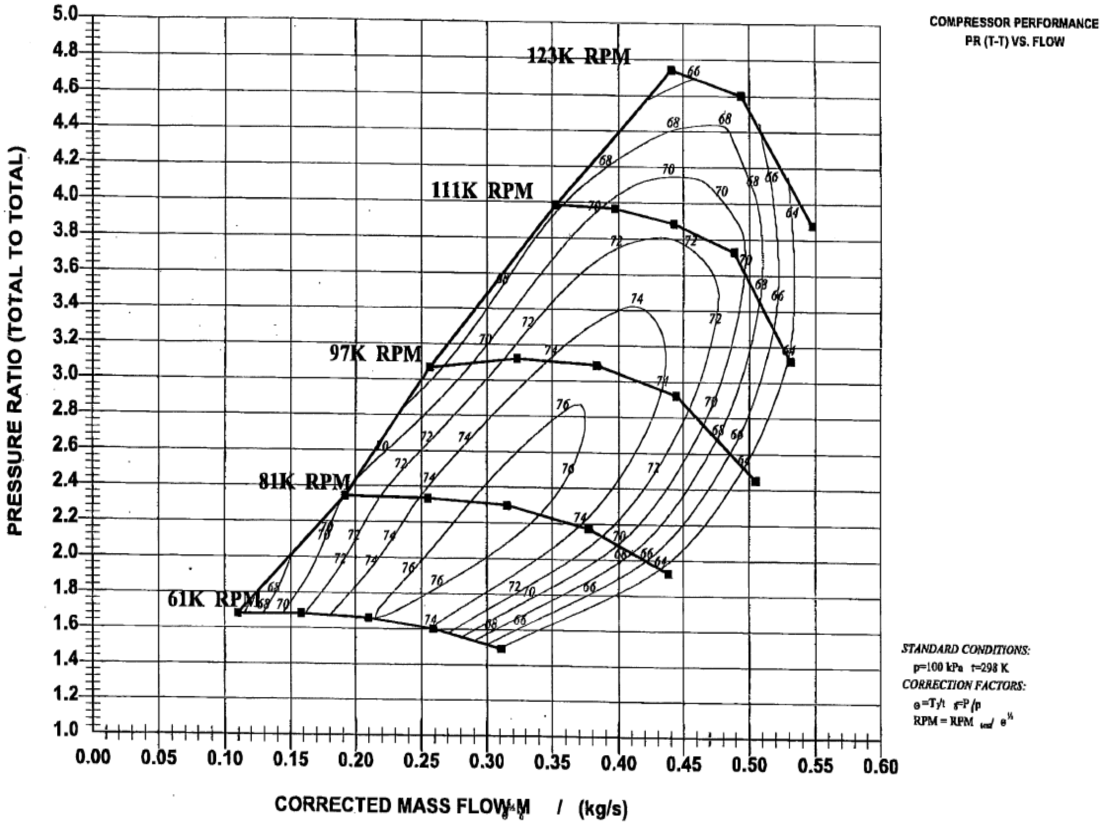

Figure 52. AMT Olympus compressor performance map.

The corrected air mass flow rate is defined in Eq. (58):

$$\dot{m}_{corr} = \frac{\dot{m}\theta^{1/2}}{\delta} = \frac{\dot{m}\left(T_{02}/T_{ref}\right)^{1/2}}{\left(P_{02}/P_{ref}\right)} \tag{58}$$

where θ is the temperature correction factor, δ is the pressure correction factor, P_{ref} is the reference pressure (P_{ref} = 100 kPa), and T_{ref} is the reference temperature (T_{ref} = 298 K). The corrected shaft speed is defined in Eq. (59):

$$N_{corr} = \frac{N}{\theta^{1/2}} \tag{59}$$

where θ is again the temperature correction factor.

A.2 Low Pressure Turbine Map

The low pressure turbine map below is the unscaled version of the performance map used in the Olympus engine model. It was created by General Electric as part of NASA's Energy Efficient Engine (E^3) program [81] and included in the NPSS software package [76]. The corrected mass flow and shaft speed are defined here the same as in Appendix "A.1 Olympus Compressor Map".

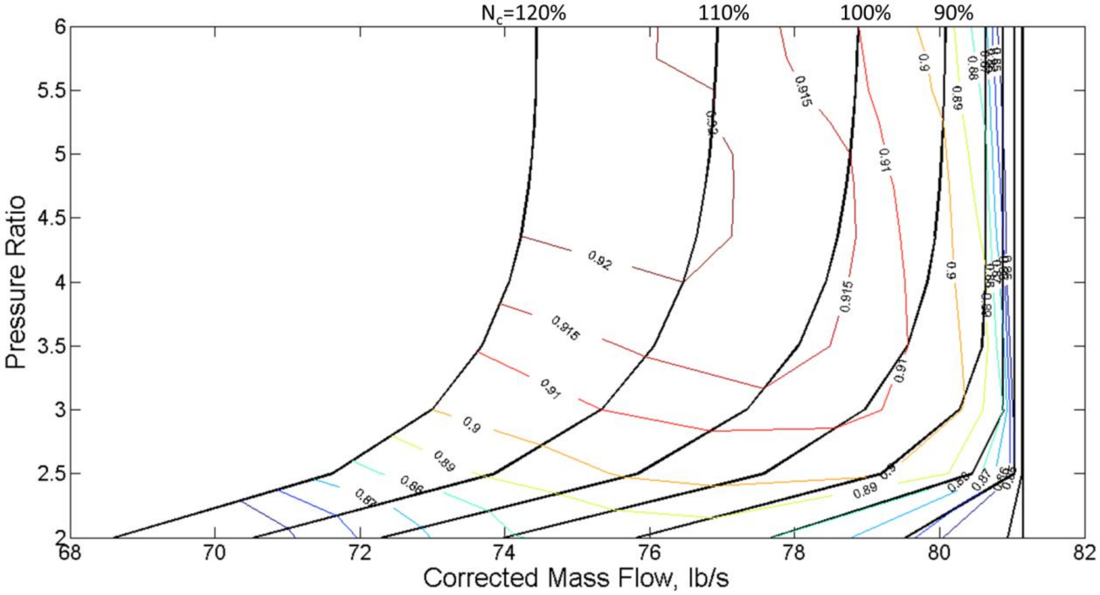

Figure 53. General Electric's low pressure turbine performance map from the Energy Efficient Engine Program [1].

Appendix B: Details of NPSS Olympus Model

B.1 Order of Execution

In a physical gas turbine system, the flow properties at a particular stage in the engine depend on the flow properties further upstream of that stage. Similarly, the components in an NPSS engine model rely on flow information stored and passed from preceding elements to calculate performance of the current element. Elements must be ordered such that the current element receives all required flow information to calculate its own flow properties and propagate that information downstream. Below is the order in which elements are executed for this work:

1. Ambient element: AmbientNASA ‘Amb’
2. Inlet Start element: InletStartNASA ‘InletStart’
3. Inlet element: Inlet ‘InEng’
4. Compressor element: Compressor ‘CmpH’
5. Fuel Start element: FuelStart ‘FusEng’
6. Burner element: Burner ‘BrnPri’
7. Turbine element: Turbine ‘TrbH’
8. Duct element: DuctNASA ‘D043’
9. Nozzle element: NozzleNASA ‘NozPri’
10. Flow End element: FlowEnd ‘FePri’
11. Shaft element: Shaft ‘ShH’

B.2 How to Run an NPSS Model

Below is an extremely basic outline on how to run an NPSS model:

1. Define an engine model ('.mdl') file.
    a. Include all necessary components (elements), and declare them in proper order.
    b. Be sure all fluid and shaft ports are linked properly.
    c. Input parameters for each element may be declared in this file, but they are typically changed in the '.case' file.
2. Define a case ('.case') file.
    a. Define a design case to set the baseline engine model according to specified design parameters.
    b. Define one or more off-design cases that adjust the model's input parameters to find operating conditions away from the design point.
    c. Make sure the solver is configured with the same number of independents as dependents for each case.
3. Define a run ('.run') file.
    a. The desired thermodynamics package is usually declared here.
    b. Include any output files, the model file, and the case file.
    c. The order in which files are included is important. For example, if the case file calls an output file, the output file should be included before the case file. Similarly, make sure the case file is included after the model file so that input parameters are initialized and changed properly.

4. Run the model.
    a. Open the NPSS command line prompt. To run the model, use the command “npss.nt *RunFileName*.run”. Be sure to include the file name extension ‘.run’.
    b. Make sure the NPSS command line prompt is in the same path/directory as all relevant files (‘.run’, ‘.case’, ‘.mdl’ files, etc.).

Appendix C: Example NPSS Code

C.1 Turbojet '.run' Run File

The following code is used to setup and run a turbojet engine model in NPSS. It declares the thermodynamics package and includes all relevant files such as output files, the model file, and case files.

Contents of the '.run' file:

```
//Set the thermo package
setThermoPackage("CEA", "Air", "H2O", "Jet-A(L)", "O2", "H2", "H",
                  "O", "N", "C", "Ar" );

//output files
#include "Viewers/perf_Olympus.view"
#include "Viewers/stage_Olympus.view"

//model file
// #include "turbojet.mdl"
#include "olympusNASAIn.mdl"
setOption("switchTransport","EQUIL");

//set parameters
#include "Parameters/solver_var.int" //solver independents and
                                     //dependents

//case input files
// #include "turbojet.case"
#include "Cases/olympusNASAIn.case"
// #include "Cases/SensitivityOD.case"
// #include "Cases/SensitivityDes.case"

//convergence statistics
// #include "ConvergeStats.report"
```

C.2 Example ‘.case’ Case File

The following code defines multiple cases to be run with the engine model. It runs a design case where the baseline engine model is set followed by several off-design cases that predict engine performance away from the design point.

Contents of the ‘.case’ file:

```
// conversion factors
real kelv_to_rank = 9./5;
real rank_to_kelv = 5./9;

perfTitles(); //set up headings in perf output file
stageTitles(); //set up headings in stage output file

setOption( "switchDes", "DESIGN" );
autoSolverSetup();

solver.addIndependent( "AirControl" );
// solver.addIndependent( "TurbPR" );
// solver.addIndependent( "TurbEff" );
// solver.addIndependent( "Qloss" );
// solver.addDependent( "Thrust" );
solver.addDependent( "TIT" );
// solver.removeIndependent( "TrbH.S_map.ind_parmMap");

cout << "\n\nDesign independents:\n" << solver.independentNames;
cout << "\n\nDesign Dependents:\n" << solver.dependentNames;

//based on initial experimental data (max RPM case)
Amb.switchMode = "PSTSMN";
Amb.Ps_in = 14.523;
Amb.Ts_in = 535.05; //297.25K
CmpH.S_map.PRdes = 3.7;
CmpH.S_map.effDes= 0.75;
BrnPri.dPqPBase = 1-0.948;
BrnPri.Wfuel = 0.0262;
BrnPri.Qhx = 116.857;
TrbH.S_map.effDes = 0.729166;
NozPri.PsExh = Amb.Ps_in;

real throttle;
throttle = 100.;

int HoodOn;
HoodOn = 0;

TIT_max = 1200.*kelv_to_rank;
Fn_target = 52.6; // from AMT data @ max RPM

// BrnPri.Fl_O.setOption("switchPrint", "TRUE");
BrnPri.Fl_O.A = 19.729; // combustor area, in^2
```

```
TrbH.Fl_O.A = 5.69; // turbine exit area, in^2

run();
perfPrint();
stagePrint();

setOption( "switchDes", "OFFDESIGN" );
autoSolverSetup();

// cout << "\n\nDesign independents:\n" << solver.independentNames;
// cout << "\n\nDesign Dependents:\n" << solver.dependentNames;

run();
perfPrint();

real Fn_FT = Perf.Fn; //initial full throttle thrust

solver.addIndependent( "Qloss" );
// solver.addIndependent( "TurbPR" );
// solver.addIndependent( "TurbEff" );
solver.addDependent( "Thrust" );
// solver.addDependent( "TIT" );

solver.maxIterations = 100;
solver.maxJacobians = 100;

cout << "\n\nOff-Design independents:\n" << solver.independentNames;
cout << "\n\nOff-Design Dependents:\n" << solver.dependentNames;

real throt[] = {23.5,38.89,51.28,61.54,71.37,79.91,
                87.61,94.02,100.};
real TambK[] = {295.79,295.72,295.94,296.62,296.78,296.09,
                296.98,296.90,297.25};
real Pamb[] = {14.632,14.606,14.581,14.564,14.554,14.542,
               14.533,14.530,14.523};
real fuel[] = {0.009000,0.011466,0.013655,0.015781,0.017847,
               0.020004,0.022069,0.024319,0.0262};
real fuelEff[] = {0.925549495,0.925138808,0.927036074,0.928615835,
      0.928850157,0.935733732,0.940858224,0.941247835,0.947688425};

int i;
for(i=0;i<throt.entries();i++) {

      throttle = throt[i];
      Amb.Ts_in = TambK[i]*kelv_to_rank;
      Amb.Ps_in = Pamb[i];
      Fn_target = throt[i]/100.*Fn_FT;
      BrnPri.Wfuel = fuel[i];
      BrnPri.dPqPBase = 1-fuelEff[i];
      NozPri.PsExh = Pamb[i];

      HoodOn = 0;
      run();
      perfPrint();
      stagePrint();

}
```

C.3 Turbojet ‘.mdl’ Model File

The following code declares the gas turbine components that define the engine model.

Contents of the ‘.mdl’ file:

```
Element AmbientNASA Amb {
  switchMode = "ALDTMN";
  alt_in      = 0.;
  dTs_in    = 0.;
  MN_in       = 0.;
} //END Amb


Element InletStartNASA InletStart{
  AmbientName = "Amb";
  W_in = 0.99; // max flow rate
} //END InletStart


Element Inlet InEng {
  eRamBase = 1.0;
} //END InEng


Element Compressor CmpH {
#include "Maps/olympusCompEff.map";
  S_map.PRdes  = 3.8;
  S_map.effDes= 0.719;
  S_map.RlineMap = 1.3;
  S_map.NcDes = 1.0;
} //END CmpH


Element FuelStart FusEng {
      fuelType  = "Jet-A(L)"; // define fuel type for CEA
      hFuel = -779.584;
} //END FusEng


Element Burner BrnPri {
      dPqPBase = 0.05;
      effBase = 0.95;
      Qhx = 115.;
      switchBurn = "FUEL";
      Wfuel = 0.0235; // fuel flow @ max RPM
      tolRayleigh = 0.0001;
} //END BrnPri


Element Turbine TrbH {
#include "Maps/lptE3.map"; //low pressure turbine map
  S_map.parmMapDes   = 2.098;
```

```
  S_map.parmNcDes = 100.0;
  S_map.effDes       = 0.80;
  // eff = 0.80;
  // PRbase = 2.265;
} //END TrbH


Element DuctNASA D043 {
  switchDP = "INPUT";
  void preexecute() {
    dPqP_in = 0.25 * Fl_I.MN * Fl_I.MN;
  }
  Fl_I.MNdes = 0.4;
} //END D043


Element NozzleNASA NozPri {
  // PsExhName = "Amb.Ps";
  PsExh = 14.7;
  setOption("switchFrozen","EQUIL");
} //END NozPri


Element FlowEnd FePri {
} //END FePri


Element Shaft ShH {
  //  Mechanical Ports.  These are created as needed on the shaft.
  ShaftInputPort MeCmpH, MeTrbH;
  Nmech = 108500.; // max shaft speed (design point)
} //END ShH


Element PerfNASA Perf {
} //END Perf


// -------------------------------
//      linkPorts
// -------------------------------
linkPorts( "InletStart.Fl_O", "InEng.Fl_I",           "F_1"  );
linkPorts( "InEng.Fl_O",      "CmpH.Fl_I",            "F_2"  );
linkPorts("CmpH.Fl_O",        "BrnPri.Fl_I",          "F_3"  );
linkPorts( "FusEng.Fu_O",     "BrnPri.Fu_I",          "F_4"  );
linkPorts( "BrnPri.Fl_O",     "TrbH.Fl_I",            "F_5"  );
linkPorts( "TrbH.Fl_O",       "D043.Fl_I",            "F_6"  );
linkPorts( "D043.Fl_O",       "NozPri.Fl_I",          "F_7"  );
linkPorts( "NozPri.Fl_O",     "FePri.Fl_I",           "F_8"  );


// -------------------------------
//      Shaft Connect Statements
// -------------------------------
linkPorts( "CmpH.Sh_O",      "ShH.MeCmpH",   "MeCmpH" );
linkPorts( "TrbH.Sh_O",      "ShH.MeTrbH",   "MeTrbH" );
```

Appendix D: Experimental Data

D.1 Performance Data without Air Flow Rate Measurements

These data are averaged over five runs at each throttle setting. The values of T_{04} and T_{05} are corrected for conduction and radiation losses in the thermocouples. This data set was used to generate the results reported in this work.

% Throttle	20	40	60	80	100
RPMc	66329.76	83642.83	93676.76	99979.95	106957.6
Thrust (N)	53.84159	95.68119	135.4801	166.6891	210.7888
Fuel Flow (kg/s)	0.00373	0.00551	0.007304	0.00899	0.011188
TSFC (g/kN-s)	69.30894	57.60343	53.92097	53.93981	53.08401
Pamb (kPa)	102.1944	102.1606	102.1403	102.1267	101.9709
P03 (kPa)	187.1453	253.0807	306.2492	342.3898	385.5344
P04 (kPa)	172.5758	235.4037	287.1719	323.2899	366.9106
P05 (kPa)	110.2941	124.4936	136.7637	146.5123	162.5681
Tamb (K)	294.8709	294.7877	295.1041	295.8127	296.5325
T03 (K)	362.9853	405.2246	436.1717	458.1209	489.8702
T04 (K)	945.121	974.0879	1030.479	1125.402	1228.329
T05 (K)	892.1089	876.0026	951.07	1009.646	1132.441

D.2 Performance Data with Air Flow Rate Measurements

These data are averaged over five runs at each throttle setting. The values of T_{04} and T_{05} are corrected for conduction and radiation losses in the thermocouples.

% Throttle	20	40	60	80	100
RPMc	65915.48	84208.1	93815.04	100507.9	107298.7
Thrust (N)	90.13677	153.7327	200.5396	240.282	282.8758
Air Flow (kg/sec)	0.227815	0.317627	0.364099	0.39163	0.40518
Fuel Flow (kg/s)	0.003922	0.005631	0.007314	0.009081	0.011304
TSFC (g/kN-s)	43.52936	36.63897	36.48742	37.80207	39.9616
Pamb (kPa)	101.6594	101.6526	101.6323	101.6255	101.6255
P02 (kPa)	96.02101	94.35704	93.37997	92.73244	92.16315
P03 (kPa)	181.79	250.572	300.5491	339.1346	379.5129
P04 (kPa)	168.041	233.6222	282.0071	320.1258	361.7134
P05 (kPa)	109.39	124.4237	135.7178	146.0545	161.796
Tamb (K)	294.1606	293.5967	293.6114	293.8666	294.6387
T03 (K)	361.7471	406.0616	435.299	458.5792	487.8886
T04 (K)	974.7461	990.0407	1037.99	1140.946	1247.238
T05 (K)	934.7274	881.9539	950.8339	1029.453	1132.759

Bibliography

[1] D. F. Waters, “Modeling of Gas Turbine - Solid Oxide Fuel Cell Systems for Combined Propulsion and Power on Aircraft.,” University of Maryland, College Park, 2015.

[2] A. T. Isikveren, “Future of [More] Electrical Aircraft,” *ICAS Biennial Workshop*. Cape Town, South Africa, 2013.

[3] S. W. Ashcraft, A. S. Padron, K. A. Pascioni, G. W. Stout, and D. L. Huff, “Review of Propulsion Technologies for N+3 Subsonic Vehicle Concepts,” *NASA/TM-2011-217239*. 2011.

[4] P. Jackson, K. Munson, and L. Peacock, *IHS Jane’s All the World’s Aircraft: Development & Production*. Alexandria, VA: IHS Global, Inc., 2014.

[5] M. Daly and M. Streetly, *IHS Jane’s All the World’s Aircraft: Unmanned*. Alexandria, VA: IHS Global, Inc., 2015.

[6] A. Choudhury, H. Chandra, and A. Arora, “Application of solid oxide fuel cell technology for power generation - A review,” *Renewable and Sustainable Energy Reviews*, vol. 20. pp. 430–442, 2013.

[7] K. Rajashekara, J. Grieve, and D. Daggett, “Solid oxide fuel cell/gas turbine hybrid APU system for aerospace applications,” in *IEEE Industry Applications Conference*, 2006, pp. 2185–2192.

[8] J. Islas, “The Gas Turbine:: A New Technological Paradigm in Electricity Generation,” *Technol. Forecast. Soc. Change*, vol. 60, pp. 129–148, 1999.

[9] M. Hepperle, “Electric Flight - Potential and Limitations,” NATO, Braunschweig, Germany.

[10] P. G. Hill and C. R. Peterson, *Mechanics and Thermodynamics of Propulsion*, 2nd ed. Reading, MA: Addison-Wesley, 1992.

[11] T. Lombardo, “Inside Siemens’ Record-Breaking Electric Aircraft Motor,” 2016. [Online]. Available: http://www.engineering.com/ElectronicsDesign/ElectronicsDesignArticles/ArticleID/12805/Inside-Siemens-Record-Breaking-Electric-Aircraft-Motor.aspx. [Accessed: 21-Sep-2016].

[12] Aviation Week Network, “Jet-A and Avgas Fuel Prices: August 2015.” [Online]. Available: http://aviationweek.com/%5Bprimary-term%5D/jet-and-avgas-fuel-prices-august-2015. [Accessed: 21-Sep-2016].

[13] M. K. Bradley and C. K. Droney, “Subsonic Ultra Green Aircraft Research: Phase II – Volume II – Hybrid Electric Design Exploration,” *NASA/CR–2015-218704*, vol. 2, 2015.

[14] Northrop Grumman, “Targets Fact Sheet.” [Online]. Available: http://www.northropgrumman.com/Capabilities/BQM74EAerialTarget/Documents/TGTS-Fact-Sheet.pdf. [Accessed: 05-Sep-2016].

[15] J. D. Mattingly, *Elements of Propulsion: Gas Turbines and Rockets*. Reston, VA: AIAA, 2006.

[16] M. J. Moran and H. N. Shapiro, *Fundamentals of Engineering Thermodynamics*, 6th ed. Hoboken, NJ: John Wiley & Sons, Inc., 2008.

[17] R. D. Flack, *Fundamentals of Jet Propulsion with Applications*. NY: Cambridge University Press, 2005.

[18] PBS Aerospace, “Turbojet Engines.” [Online]. Available: http://www.pbsaerospace.com/engines/turbojet-engines. [Accessed: 05-Sep-2016].

[19] PBS Aerospace, “TJ 100 Turbojet Engine.” [Online]. Available: http://www.pbsaerospace.com/our-products/tj-100-turbojet-engine. [Accessed: 05-Sep-2016].

[20] Sonex, “SubSonex: The Personal Jet Reality Check.” [Online]. Available: http://www.sonexaircraft.com/subsonex/index.html. [Accessed: 05-Sep-2016].

[21] AMT Netherlands, “Products.” [Online]. Available: http://www.amtjets.com/pdf/University-Olympus-HP-Jan-2017.pdf.

[22] Jetman Dubai, “Homepage.” [Online]. Available: http://www.jetman.com/. [Accessed: 05-Sep-2016].

[23] E. Benini and S. Giacometti, “Design, manufacturing and operation of a small turbojet-engine for research purposes,” *Appl. Energy*, vol. 84, no. 11, pp. 1102–1116, 2007.

[24] A. J. B. Jackson, P. Laskaridis, and P. Pilidis, “A test bed for small aero gas turbines for education and for university - Industry collaboration,” in *Proceedings of the ASME Turbo Expo 2004*, 2004, pp. 901–909.

[25] C. R. Davison and A. M. Birk, “Set Up and Operational Experience With a Micro-Turbine Engine for Research and Education,” in *Proceedings of the ASME Turbo Expo 2004*, 2004, pp. 849–858.

[26] Turbine Technologies, “MiniLab: Gas Turbine Power System.” [Online]. Available: http://www.turbinetechnologies.com/Portals/0/pdfs/specifications/minilab Specs.pdf. [Accessed: 05-Sep-2016].

[27] M. Badami, P. Nuccio, and A. Signoretto, “Experimental and numerical analysis of a small-scale turbojet engine,” *Energy Convers. Manag.*, vol. 76, pp. 225–233, 2013.

[28] AMT Netherlands, “Olympus HP in University Configuration: Spec Sheet.” [Online]. Available: http://www.amtjets.com/pdf/University-Olympus-HP-Jan-2013.pdf.

[29] A. Al-Alshaikh, “An Experimental and Numerical Investigation of the Effect of Aero Gas Turbine Test Facility Aspect Ratio on Thrust Measurement,” Cranfield University, 2011.

[30] D. P. Bakalis and A. G. Stamatis, “Data analysis and performance model calibration of a small turbojet engine,” in *Proceedings of the Institution of Mechanical Engineers*, 2011, pp. 1523–1533.

[31] R. GRZESZCZYK, J. MERKISZ, M. GÓRECKI, B. van de GOOR, and E. KAMIŃSKA, “The Laboratory Test Bench for a Small Turbojet Engine.” 2011.

[32] A. Horoufi and M. Boroomand, “Design and Construction of Microjet Engine,” in *45th AIAA/ASME/SAE/ASEE Joint Propulsion Conference & Exhibit*, 2009.

[33] P. Laskaridis, P. Pilidis, and V. Pachidis, “Small Scale Engine Test Bed Design and Optimisation,” in *Design Optimization International Conference*, 2004.

[34] Z. Leylek, “An Investigation into Performance Modelling of a Small Gas Turbine Engine,” Australia, 2012.

[35] N. U. Rahman and J. F. Whidborne, “A numerical investigation into the effect of engine bleed on performance of a single-spool turbojet engine,” in *Proceedings of the Institution of Mechanical Engineers*, 2008, pp. 939–949.

[36] R. O’Hayre, S. Cha, W. Colella, and F. B. Prinz, *Fuel Cell Fundamentals*, 2nd ed. Hoboken, NJ: John Wiley & Sons, Inc., 2009.

[37] X. Li, *Principles of Fuel Cells*. New York: Taylor & Francis Group, 2006.

[38] R. J. Kee, H. Zhu, and G. S. Jackson, “Solid Oxide Fuel Cells Using Syngas,” in *Synthesis Gas Combustion: Fundamentals and Applications*, T. C. Lieuwen, V. Yang, and R. Yetter, Eds. London: Taylor & Francis, 2009.

[39] Ballard Power Systems, “Products.” [Online]. Available: http://www.ballard.com. [Accessed: 07-Sep-2016].

[40] B. C. H. Steele and A. Heinzel, “Materials for fuel-cell technologies,” *Nature*, vol. 414, pp. 345–352, 2001.

[41] Y. Peng and J. T. Richardson, “Properties of ceramic foam catalyst supports: one-dimensional and two-dimensional heat transfer correlations,” *Appl. Catal. A Gen.*, vol. 266, pp. 235–244, 2004.

[42] J. T. Richardson, D. Remue, and J.-K. Hung, “Properties of ceramic foam

catalyst supports: mass and heat transfer," *Appl. Catal. A Gen.*, vol. 250, pp. 319–329, 2003.

[43] L. D. Schmidt, E. J. Klein, C. A. Leclerc, J. J. Krummenacher, and K. N. West, "Production of syngas by direct catalytic-oxidation of methane," *Chem. Eng. Sci.*, vol. 58, p. 1037, 2003.

[44] J. T. Richardson, Y. Peng, and D. Remue, "Properties of ceramic foam catalyst supports: pressure drop," *Appl. Catal. A Gen.*, vol. 204, pp. 19–32, 2000.

[45] K. E. Swider-Lyons, J. A. Mackrell, J. A. Rodgers, G. S. Page, M. W. Schuette, and R. O. Stroman, "Hydrogen Fuel Cell Propulsion for Long Endurance Small UAVs," in *AIAA Naval Centennial of Flight Forum*, 2011.

[46] K. E. Swider-Lyons, R. O. Stroman, J. A. Rodgers, D. Edwards, J. A. Mackrell, M. W. Schuette, and G. S. Page, "Liquid Hydrogen Fuel System for Small Unmanned Air Vehicles," in *51st AIAA Aerospace Meeting including the New Horizons Forum and Aerospace Exposition*, 2013.

[47] Intelligent Energy, "Intelligent Energy Hydrogen Fuel Cells Significantly Extend Drone Flight Time." [Online]. Available: http://www.intelligent-energy.com/news-and-events/company-news/2015/12/15/intelligent-energy-hydrogen-fuel-cells-significantly-extend-drone-flight-time/. [Accessed: 07-Sep-2016].

[48] Intelligent Energy, "Major Drone Manufacturer Snaps Up Intelligent Energy's Game-Changer for Drone Range (Flight Time)." [Online]. Available: http://www.intelligent-energy.com/news-and-events/company-news/2016/01/28/major-drone-manufacturer-snaps-up-intelligent-energys-game-changer-for-drone-range-fight-time/. [Accessed: 07-Sep-2016].

[49] Boeing, "Boeing Successfully Flies Fuel Cell-Powered Airplane." [Online]. Available: http://www.boeing.com/aboutus/environment/environmental_report/_inc/flash-2-1-2.html. [Accessed: 07-Sep-2016].

[50] D. F. Waters and C. P. Cadou, "Engine-integrated solid oxide fuel cells for efficient electrical power generation on aircraft," *J. Power Sources*, vol. 284, pp. 588–605, 2015.

[51] F. Calise, M. Dentice d' Accadia, L. Vanoli, and M. R. von Spakovsky, "Single-level optimization of a hybrid SOFC-GT power plant," *J. Power Sources*, vol. 159, no. 2, pp. 1169–1185, 2006.

[52] Y. Haseli, I. Dincer, and G. F. Naterer, "Thermodynamic modeling of a gas turbine cycle combined with a solid oxide fuel cell," *Int. J. Hydrogen Energy*, vol. 33, no. 20, pp. 5811–5822, 2008.

[53] A. Abbasi and Z. Jiang, "Multidisciplinary modeling and simulation of a fuel

cell/gas turbine hybrid power system," in *2009 IEEE Power and Energy Society General Meeting, PES '09*, 2009, pp. 1–7.

[54] S. H. Chan, H. K. Ho, and Y. Tian, "Modelling of simple hybrid solid oxide fuel cell and gas turbine power plant," *J. Power Sources*, vol. 109, no. 1, pp. 111–120, 2002.

[55] J. Palsson, A. Selimovic, and L. Sjunnesson, "Combined solid oxide fuel cell and gas turbine systems for efficient power and heat generation," *J. Power Sources*, vol. 86, no. 1, pp. 442–448, 2000.

[56] P. Costamagna, L. Magistri, and A. F. Massardo, "Design and part-load performance of a hybrid system based on a solid oxide fuel cell reactor and a micro gas turbine," *J. Power Sources*, vol. 96, no. 2, pp. 352–368, 2001.

[57] T.-H. Lim, R.-H. Song, D.-R. Shin, J.-I. Yang, H. Jung, I. C. Vinke, and S.-S. Yang, "Operating characteristics of a 5 kW class anode-supported planar SOFC stack for a fuel cell/gas turbine hybrid system," *Int. J. Hydrogen Energy*, vol. 33, pp. 1076–1083, 2008.

[58] T. Suther, A. S. Fung, M. Koksal, and F. Zabihian, "Effects of operating and design parameters on the performance of a solid oxide fuel cell-gas turbine system," *Int. J. Energy Res.*, vol. 35, pp. 616–632, 2011.

[59] Y. Zhao, J. Sadhukhan, A. Lanzini, N. Brandon, and N. Shah, "Optimal integration strategies for a syngas fuelled SOFC and gas turbine hybrid," *J. Power Sources*, vol. 196, no. 22, pp. 9516–9527, 2011.

[60] L. Leto, C. Dispenza, A. Moreno, and A. Calabr, "Simulation model of a molten carbonate fuel cell-microturbine hybrid system," *Appl. Therm. Eng.*, vol. 31, no. 6–7, pp. 1263–1271, 2011.

[61] S. E. Veyo, L. A. Shockling, J. T. Dederer, J. E. Gillett, and W. L. Lundberg, "Tubular Solid Oxide Fuel Cell/Gas Turbine Hybrid Cycle Power Systems: Status," *J. Eng. Gas Turbines Power*, vol. 124, pp. 845–849, 2002.

[62] J. E. Freeh, J. W. Pratt, and J. Brouwer, "Development of a Solid-Oxide Fuel Cell/Gas Turbine Hybrid System Model for Aerospace Applications," *Vol. 7 Turbo Expo 2004*, no. May, pp. 371–379, 2004.

[63] C. J. Steffen Jr., J. E. Freeh, and L. M. Larosiliere, "Solid oxide fuel cell/gas turbine hybrid cycle technology for auxiliary aerospace power," *Proc. ASME Turbo Expo*, vol. 5, no. April, pp. 253–260, 2005.

[64] J. E. Freeh, C. J. Steffen, and L. M. Larosiliere, "Off-Design Performance Analysis of a Solid-Oxide Fuel Cell/Gas Turbine Hybrid for Auxiliary Aerospace Power," *3rd Int. Conf. Fuel Cell Sci. Eng. Technol.*, no. December, pp. 265–272, 2005.

[65] S. Eelman, I. d. P. y. d. Poza, and T. Krieg, "Fuel Cell APU ' s in Commercial

Aircraft – An Assessment of SOFC and PEMFC Concepts,” in *24Th International Congress of the Aeronautical Sciences*, 2004.

[66] K. Rajashekara, J. Grieve, and D. Daggett, “Hybrid Fuel Cell Power in Aircraft,” *IEEE Industry Applications Magazine*, pp. 54–60, 2008.

[67] R. J. Braun, M. Gummalla, and J. Yamanis, “System Architectures for Solid Oxide Fuel Cell-Based Auxiliary Power Units in Future Commercial Aircraft Applications,” *J. Fuel Cell Sci. Technol.*, vol. 6, no. August 2009, p. 31015, 2009.

[68] A. Himansu, J. E. Freeh, C. J. Steffen, R. T. Tornabene, and X. Y. J. Wang, “Hybrid solid oxide fuel cell / Gas turbine system design for high altitude long endurance aerospace missions,” in *Proceedings of 4th International ASME Conference on Fuel Cell Science, Engineering and Technology, FUELCELL2006*, 2006.

[69] P. Aguiar, D. J. L. Brett, and N. P. Brandon, “Solid oxide fuel cell/gas turbine hybrid system analysis for high-altitude long-endurance unmanned aerial vehicles,” *Int. J. Hydrogen Energy*, vol. 33, no. 23, pp. 7214–7223, 2008.

[70] M. K. Bradley and C. K. Droney, “Subsonic Ultra Green Aircraft Research: Phase I Final Report,” *NASA/CR- 2011-216847*, 2011.

[71] M. K. Bradley and C. K. Droney, “Subsonic Ultra Green Aircraft Research Phase II: N+4 Advanced Concept Development,” *NASA/CR- 2012-217556*, 2012.

[72] A. R. Knott and C. P. Cadou, “Development of a Small Gas Turbine Engine Test Facility,” University of Maryland, College Park, 2014.

[73] JetCat USA, “Products.” [Online]. Available: http://www.jetcatusa.com/rc-turbines/.

[74] Jet Central USA, “Turbines.” [Online]. Available: http://www.jetcentralusa.com/.

[75] KingTech Turbines, “Turbines.” [Online]. Available: http://www.kingtechturbines.com/eshop/.

[76] NASA, “NPSS user guide, software release 1.6.5.” 2008.

[77] NASA, “NPSS developer’s guide, software release 1.6.5.” 2008.

[78] B. McBride and S. Gordon, “Computer Program for Calculation of Complex Chemical Equilibrium Compositions and Applications II. User’s Manual and Program Description.” NASA, RP-1311-P2, 1996.

[79] N. Sissenwine, M. Dubin, and H. Wexler, “The U.S. Standard Atmosphere, 1962,” *J. Geophys. Res.*, vol. 67, no. 9, pp. 3627–3630, 1962.

[80] P. Batterton, “Energy efficient engine program contributions to aircraft fuel conservation,” in *Aviation Fuel Conservation Symposium*, 1984.

[81] C. Ciepluch, D. Davis, and D. Gray, “Results of NASA’s energy efficient engine program,” *J. Propuls.*, vol. 3, no. 6, pp. 560–568, 1987.

[82] C. T. Kelley, *Solving Nonlinear Equations with Newton’s Method*. Philadelphia: Society for Industrial and Applied Mathematics, 2003.

[83] J. Ortega and W. Rheinboldt, *Iterative Solution of Nonlinear Equations in Several Variables*. New York: Academic Press, 1970.

[84] C. T. Kelley, *Iterative Methods for Linear and Nonlinear Equations*. Philadelphia: Society for Industrial and Applied Mathematics, 1995.

[85] A. G. Kehlenbeck, “Development of a Thrust Stand for a Miniature Jet Engine,” University of Maryland, College Park.

[86] National Weather Service, “College Park Airport Weather.” [Online]. Available: http://w1.weather.gov/obhistory/KCGS.html.

[87] Omega, “Thermocouples: Using Thermocouples in Temperature Measurement.” [Online]. Available: http://www.omega.com/prodinfo/thermocouples.html. [Accessed: 27-Sep-2016].

[88] A. F. Mills, *Basic Heat & Mass Transfer*, 2nd ed. Upper Saddle River, NJ: Prentice Hall, Inc., 1999.

[89] F. P. Incropera and D. P. DeWitt, *Introduction to Heat Transfer*, 2nd ed. John Wiley & Sons, Inc., 1990.

[90] S. P. Venkateshan, “Systematic errors in temperature measurement.” Indian Institute of Technology Madras.

[91] A. Faghri, Y. Zhang, and J. Howell, *Advanced Heat and Mass Transfer*. Global Digital Press, 2010.

[92] AMT Netherlands, “Olmypus HP Manual.” 2017.

[93] The American Society of Mechanical Engineers, “ASME PTC 19.1-2005: Test Uncerrtainty.” ASME International, New York, 2005.